Integration of Different Constitutive Models in Multibody System Algorithms

BY

LIANG WANG

B.Sc., Harbin Institute of Technology, 2009
M.Sc., Harbin Institute of Technology, 2011

THESIS

Submitted as partial fulfillment of the requirements
for the degree of Doctor of Philosophy in Mechanical Engineering
in the Graduate College of the
University of Illinois at Chicago, 2016

Chicago, Illinois

Defense Committee:

Professor Ahmed A. Shabana, Chair and Advisor, Mechanical and Industrial Engineering
Behrooz Fallahi, Mechanical Engineering, Northern Illinois University
Eduard Karpov, Civil and Materials Engineering
Shengwei Chi, Civil and Materials Engineering
Thomas J. Royston, Bioengineering

This thesis is dedicated to my family.

ACKNOWLEDGEMENTS

I would like to express my great appreciation to my advisor, Dr. Ahmed A. Shabana, for his strong support, extensive guidance, valuable suggestions and continuous encouragement throughout my graduate studies at the University of Illinois at Chicago. I would also like to thank the members of my thesis committee: Dr. Behrooz Fallahi, Dr. Eduard Karpov, Dr. Shengwei Chi and Dr. Thomas J. Royston for their invaluable advice. I am particularly grateful to Dr. Jesús R. Jiménez Octavio and Dr. Cheng Wei for their advice regarding the implementation of the liquid sloshing model using both floating frame reference and absolute nodal coordinate formulation, and to Dr. Yongxing Wang and Dr. Antonio M. Recurero for their help in developing the textile roll-drafting process presented in this thesis.

I would also like to thank my friends and colleagues currently working at and graduated from the Dynamic Simulation Laboratory with whom I have worked over the years. Each of them has helped me in their own ways whether it be advice directly pertaining to my work or one of the many discussions we have had that have expanded my academic knowledge.

I would also like to thank my parents who raised me up and supported me in all my pursuits, and I am particularly grateful to my loving, encouraging and patient wife, Ruixue Sun, without their continued support and encouragement, I could never have accomplished my studies.

CONTRIBUTION OF AUTHORS

Chapter 1 is a literature review that describes the contributions made by other researchers. This literature review serves to define clearly the contribution of this thesis. Chapter 2 represents a published manuscript (include complete citation) for which I was the first author and the lead researcher. Dr. Jesús R. Jiménez Octavio helped me in validating the mode shapes using the software ANSYS while Dr. Cheng Wei helped me in checking the equations. My advisor, Dr. Shabana contributed to defining the problem and supervising the research. Chapter 3 represents a published manuscript (include complete citation) for which I was the second author. I formulated the constitutive model and produced Figs. 23, 25 27, 28, 29 and 31. I played a large role in the writing of the manuscript along with the first author Dr. Cheng Wei and my academic advisor Dr. Shabana. My work was critical to the conclusions made in this manuscript because the procedure of deriving the fluid constitutive model using the Lagrangian approach is similar to the procedure used in Chapter 2 and a comparative study between the two approaches has been made. Chapter 4 represents a published manuscript (include complete citation) for which I was the first author and lead researcher. Dr. Yongxing Wang helped in building the roll-drafting model. Dr. Antonio M. Recurero and Dr. Shabana helped in defining the problem and supervising the research. In Chapter 5 provides a summary and the main contributions of this thesis as well as defines future research directions.

TABLE OF CONTENTS

TABLE OF CONTENTS (continued)

TABLE OF CONTENTS (continued)

LIST OF TABLES

LIST OF FIGURES

LIST OF FIGURES (continued)

SUMMARY

Multibody systems (MBS) in general include two collections of bodies. One collection consists of bulky and compact solids which can be treated as rigid bodies, while the second collection includes bodies that can be treated as flexible bodies that experience small and large deformations and undergo large rotations. Many technological and industrial problems such as liquid sloshing, textile hyper-elastic, biomechanics and vehicle terrain interaction require efficient and accurate modeling of flexible bodies. One of the objectives of this thesis is to develop a low order continuum-based liquid sloshing model that can be successfully integrated with multibody system algorithms. The liquid sloshing model proposed in this thesis allows for capturing the effect of the distributed inertia and the viscosity of the fluid. The fluid viscous forces are defined using the Navier-Stokes equations. In order to demonstrate the use of the approach presented in this study, the assumption of an incompressible Newtonian fluid is considered with a total Lagrangian approach. Fluid properties such as the incompressibility condition are formulated using a penalty method. The low order model that could capture the effect of the distributed fluid inertia on the vehicle dynamics is developed in this thesis using the *floating frame reference* (FFR) formulation. The use of this approach allows for developing an inertia-variant fluid model that accounts for the dynamic coupling between different modes of the fluid displacements. The matrix of position vector gradients and its derivative are formulated using the FFR kinematic description. The position and velocity gradient tensors are used to define the Navier-Stokes stress forces. The proposed liquid sloshing model is integrated with a MBS railroad vehicle model in which the rail/wheel interaction is formulated using a three-dimensional elastic contact formulation that allows for the wheel/rail

separation. Several simulation scenarios are used to examine the effect of the distributed liquid inertia on the motion of the railroad vehicle. The results, obtained using the sloshing model, are compared with the results obtained using a rigid body vehicle model. The comparative numerical study presented in this thesis shows that the effect of the sloshing tends to increase the possibility of wheel/rail separation as the forward velocity increases, thereby increasing the possibility of derailments at these relatively high speeds.

Another objective of this thesis is to develop a total Lagrangian non-incremental liquid sloshing solution procedure based on the *finite element* (FE) *absolute nodal coordinate formulation* (ANCF). The proposed liquid sloshing modeling approach can be used to avoid the difficulties of integrating most of fluid dynamics formulations, which are based on the Eulerian approach, with MBS dynamics formulations, which are based on a total Lagrangian approach. The proposed total Lagrangian FE fluid dynamics formulation, which can be systematically integrated with computational MBS algorithms, differs significantly from the conventional FE or finite volume methods which are based on an Eulerian representation that employs the velocity field of a fixed control volume in the region of interest. The ANCF fluid equations are expressed in terms of displacement and gradient coordinates of material points, allowing for straight forward implementation of kinematic constraint equations and for the systematic modeling of the interaction of the fluid with the external environment or with rigid and flexible bodies. The fluid incompressibility conditions and surface traction forces are considered and derived directly from the Navier Stokes equations. Two ANCF brick elements, one of which is obtained using an

incomplete polynomial representation and the other of which is obtained from a B-spline volume representation, are used. The new approach ensures the continuity of the displacement gradients at the nodal points and allows for imposing higher degree of continuity across the element interface by applying algebraic constraint equations that can be used to eliminate dependent variables and reduce the model dimensionality. Regardless of the magnitude of the fluid displacement, the fluid has a constant mass matrix, leading to zero Coriolis and centrifugal forces. The analysis presented in this thesis demonstrates the feasibility of developing an efficient non-incremental total Lagrangian approach for modeling sloshing problems in MBS system applications in which the bodies can experience large displacements including finite rotations. Several examples are presented in order to shed light on the potential of using the ANCF liquid sloshing formulation developed in this study.

This thesis also presents a new flexible MBS approach for modeling textile systems including roll-drafting sets used in chemical textile machinery. The proposed approach can be used in the analysis of textile materials such as lubricated *polyester filament bundles* (PFB) which have un-common material properties best described by specialized continuum mechanics constitutive models. In this thesis, the ANCF is used to model PFB as a hyper-elastic transversely isotropic material. The PFB strain energy density function is decomposed into a fully isotropic component and an orthotropic, transversely isotropic component expressed in terms of five invariants of the right Cauchy-Green deformation tensor. Using this energy decomposition, the second Piola-Kirchhoff stress and the elasticity tensors can also be split into isotropic and transversely isotropic

parts. The constitutive equations are used to define the generalized material forces associated with the coordinates of three-dimensional fully-parameterized ANCF finite elements. The proposed approach allows for modeling the dynamic interaction between the rollers polyester filament bundle and allows for using spline functions to describe the PFB forward velocity. The textile material constitutive equations and the MBS algorithms can be used effectively to obtain numerical solutions that define the state of strain and cross section deformation of the textile material and the relative slip and contact forces between rollers and PFB.

CHAPTER 1

INTRODUCTION

Multibody systems (MBS) consist of interconnected rigid and/or flexible bodies, each of which can undergo large translation and finite rotation. Many mechanical, structural, and biological systems such as vehicles, trains, aircrafts, robotic manipulators and human body joints can be considered as MBS examples. An important MBS example is railroad vehicles. Considering recent train accidents (King, 2015; Yan and Conlon, 2015) which involved freight tank cars carrying crude oil and other hazardous liquid materials, it is necessary to understand the dynamic behavior of liquid sloshing in tank cars under different motion scenarios in order to avoid serious accidents. Successful integration of fluid constitutive models with the railroad vehicle dynamics in computational MBS algorithms that allow for systematically formulating the kinematic and boundary constraint conditions is necessary to better understand the liquid sloshing phenomenon. Another challenging problem is the roll-drafting process in the chemical textile industry. Over the past decades, researchers, technicians, and engineers have attempted to control the bundle deformation regions during the roll-drafting process by using various diameters, different numbers of rollers in a drawing machine, and/or changing roller material, for instance, using rubber. These attempts are often based on experience or experiments because of the lack of accurate computational MBS models, and the difficulties in measuring the roller contact forces, PFB internal tension the velocity of certain points on the bundle, and/or the cross section deformation during the roll-drafting process. It is therefore critical to develop a new constitutive model for textile material and successfully integrate that with computational MBS algorithm which can be

used in the analysis and virtual prototyping of the textile machine in general and in the roll-drafting process in particular.

1.1 Background

The effect of liquid sloshing has been a subject of a large number of investigations. In many of these investigations, the effect of the fluid dynamics on the vehicle motion was the main concern. To this end, simple fluid models that have discrete inertia were developed; some of these models are represented using a simple planar pendulum model (Dodge and Kana, 1966; Kana, 1987; Kane, 1989; McIvor, 1989; Pinson, 1964; Sumner, 1965; Tritton, 1986; Unruh et al., 1986; Werner and Coldwell, 1961; Bauer, 1960). While the main focus of many of these investigations was on the effect of the fluid on the vehicle dynamics, the simplified models developed in these previous studies failed to capture the effect of the distributed inertia of the fluid due to the change in the fluid shape. The main goal of these past investigations, as well as this thesis, is not the development of an accurate fluid model that captures turbulence and other nonlinear effects, rather the main goal is to develop a simplified fluid model that allows for studying the effect of sloshing on the system dynamics.

These simplified liquid sloshing models can be of great value in many areas of science and engineering, including space, marine, and highway applications. Of particular interest in this study are railroad vehicle systems. As the speeds and loads of freight trains continue to increase, more investigations of the nonlinear dynamic behavior of railroad vehicle systems are needed. There are many factors that have a significant effect on the wheel/rail dynamic interaction, including the

wheel and rail profiles, car body vibration, track irregularities, and wheel/rail contact forces (Iwnicki, 2006; Shabana et al., 2008). The objective of this thesis is to propose a reduced order liquid sloshing model that can be integrated with three-dimensional multibody system (MBS) algorithms to study the effect of the liquid motion and its distributed inertia on the nonlinear dynamics of the rail vehicles. When a tank car is partially filled, the sloshing can cause a change in the shape and the location of the center of gravity of the car, resulting in time-varying inertia forces. These distributed inertia forces can have a significant effect on the wheel/rail contact forces and can lead to serious and costly accidents, particularly in the case of transporting hazardous liquid materials. An example is the recent derailment accident, in which a train consisting of 72 cars filled with oil derailed in Lac-Megantic, Quebec, Canada. As the result of this accident, 15 people died, 60 were missing, and 30 buildings were destroyed (CBS News, 2013). Meanwhile, the statistics published by the U.S. Department of Transportation (U.S. Dep. Transportation, 2013) show that the property damage due to hazardous material accidents reached about $25.2 million in 2007 and had an average yearly cost of $12.6 million between 2000 and 2010. Thus, considerable savings and better rolling stock performance can be achieved by improving the stability, safety margins, maximum allowable speed, and liquid carrying capacity of freight cars.

The development of computational models is the most economic and efficient method to design and evaluate the performance of physics and engineering systems. The use of virtual prototyping reduces the cost and allows for efficient examination of the effect of various system parameters. In particular, the MBS approach is the most suitable simulation technique for vehicle dynamics. Nonetheless, modeling of partially filled tank cars remains a challenging problem, as

evident by the simple pendulum sloshing models reported in the literature. The integration of an accurate sloshing model and MBS algorithms requires successful integration of a finite element (FE) or finite difference and MBS algorithms. Generally speaking, sloshing phenomena involve arbitrary motion of the free surface of a liquid. For instance, the motion of the liquid surface inside a partially filled container can be caused by disturbances to the vehicle motion as well as the design and shape of the container. The motion can be planar, non-planar, rotational, symmetric, asymmetric, quasi-periodic and even chaotic motion. In fact, many industrial, aerospace and structural applications exhibit these phenomena, including tank cars transported by trucks and freight trains, aerospace vehicles, large rockets, water reservoirs, nuclear vessels, etc.

This thesis is also concerned with developing a new continuum-based MBS approach for modeling textile systems. This investigation is motivated by the fact that only simple models exist in the literature for the analysis of such complex and highly nonlinear systems. The dynamic behavior of such complex textile systems, however, cannot be accurately captured using simplified approaches. In order to shed light on the complexity of such textile systems, MBS algorithms are used. The *polyester as-spun fiber*, obtained from melt spinning process, is a material commonly used in textile roll-drafting machines. This fiber has fairly weak crystallinity and orientation properties which make the fiber unsuitable for many practical uses. In the chemical fiber industry, subsequent processing, such as drawing (or roll-drafting) and setting, must be performed on the as-spun fiber in order to improve its fiber structure and surface morphology. The roll-drafting process leads to a higher performance fiber and increases its added value.

Compared with the *polyester filament bundle* (PFB) setting process, the drawing process

involves many complex factors and craft parameters. The most widely used setup in the PFB roll-drafting process is to link three sets of drawing machines together and draw and stretch the PFB among them consecutively, as shown in Fig. 1. Two hot water tanks with different temperatures are used to modify the PFB mechanical properties by reducing the modulus of elasticity and facilitating elongation. The complete drawing process increases the PFB length three to five times and the first two sets of drawing machines accomplish approximately 80~90 percent of the work. The rollers in each set of drawing machines are driven by controlled motors which produce the same roller angular velocity in each set of drawing machine. Sliding between the fiber and the rollers must be avoided; and for that reason, seven rollers are usually used in a drawing machine and one holding roller at the output side. Rollers of different sets of the drawing machine stretch the PFB, whereas rollers of the same set of the drawing machine drive the bundle forward.

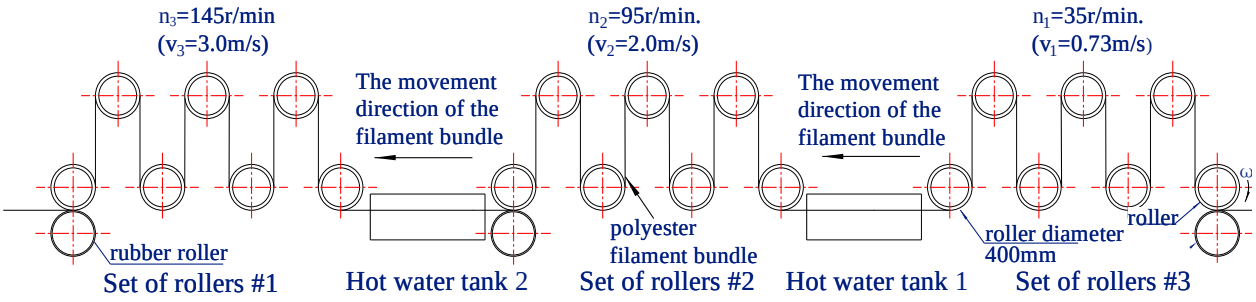

Figure 1. Roll-drafting process

During this process, millions of filaments are bundled together and fed into the drawing machine. The total amount of filament can reach 1.5 million Denier; a Denier is equivalent to the weight in grams of 9,000 meters of yarn. The output speed of the bundle after the drawing process is approximately 180 m/min. During the roll-drafting process, the PFB undergoes large elastic and plastic deformation; therefore, the cross section of the PFB can change dramatically. In order to

have these deformations under control, the plastic deformation between two sets of drawing machines must be concentrated in a certain region in the hot water tanks. Failure in controlling the concentrated plastic deformation region can lead to unpredictable fiber elongation ratio, which will not only produce non-uniform thickness, but also cause un-stretched filaments. Both of these flaws highly affect the quality of polyester fiber; consequently, fixing and controlling the position of deformation points is crucial in the industrial post processing stage of polyester fiber. Other craft requirements, such as making the PFB parallel to each other and homogenously distributed on the rollers, have to be taken into consideration in order to ensure proper filament tension.

A key point in the drawing process of PFB is to make the deformed material remain in a certain area while the PFB is moving at a high speed. Through the roll-drafting process, the contact forces between rollers and textile material, the PFB internal force distribution, the variation of cross section of the filament bundle, the configurations of rollers, and the sliding between bundle and machine are all factors that affect the distribution of the deformed material. Over the past decades, researchers, technicians, and engineers have attempted to control the bundle deformation regions during the roll-drafting process by using various diameters, different numbers of rollers in a drawing machine, and/or changing roller material, for instance, using rubber. These attempts are often based on experience or experiments because of the lack of accurate computational MBS models, and difficulties in measuring the roller contact forces, PFB internal tension the velocity of certain points on the bundle, and/or the cross section deformation during the roll-drafting process. It is therefore critical to develop a computational MBS method that can be used in the analysis and virtual prototyping of the textile machine in general and in the roll-drafting process in particular.

Such a computational MBS approach can be used effectively in the design and the analysis of different drawing machine configurations.

1.2 Liquid Sloshing Phenomenon Modeling

Different analytical approaches have been developed in order to simulate the dynamic response of liquid-filled tanks (Ibrahim et al., 2001; Ibrahim, 2005; Rebouillat and and Liksonov, 2010), taking into account not only the nature of the sloshing but special types of tank geometry as well. Early contributions were focused on developing equivalent mechanical models by means of mass-spring systems or by a using set of pendulums as previously mentioned (Graham, 1951; Graham and Rodríguez, 1952; Abramson, 1966; Zheng et al., 2012). In spite of its linear nature, which made these simplified models insufficient to account for the effect of rapid velocity changes of energy dissipation, new more detailed models have been developed incorporating dashpot elements to take into account the effect of nonlinear motion (Ranganathan et al., 1989). Broadly speaking, equivalent mechanical models have been developed for linear planar liquid motion, in the form of a series of mass-spring-dashpot systems or a set of simple pendulums, and for nonlinear sloshing phenomena as well by using spherical or compound pendulums which may represent rotational and chaotic sloshing. These models, however, still cannot capture the accurate inertia distribution of the liquid and the shape of the free surface as discussed by Aliabadi et al. (2003) who compared the FE fluid and the discrete element models and demonstrated the limitations of the discrete element model. In order to overcome the limitations of the equivalent mechanical models, more realistic spatial fluid models using computational and numerical methods were proposed. The

Eulerian and Lagrangian approaches are the two main methods to study the motion of the fluid (Reddy and Gartling, 2010). The Lagrangian description traces the material points, while the second is the Eulerian description in which the interest is focused on the fluid movement at fixed region or control volume. Lagrangian description has the advantage of tracing the fluid material points and examining systematically their interactions with other bodies and external environment, such a description has not been fully utilized in the study of the effect of liquid sloshing in MBS applications including vehicle systems. The Eulerian approach, which is not quite suitable for MBS applications, remains the most popular approach in the CFD field (Versteeg et al., 2007; Reddy et al., 2001; Zienkiewicz et al., 2005; Anderson, 1995; Zikanov et al., 2010). Integration of an Eulerian fluid procedure with MBS algorithms can be difficult even for simple liquid sloshing problems where turbulence is not an issue. Nonetheless, the existing more detailed FE models are not suitable for integration with MBS algorithms due to many factors that include the problem dimensionality, the basic differences between the FE and MBS approaches, differences in numerical solution procedures, and the way large displacements and rotations are treated in existing FE models.

While some mesh-free methods have been developed for fluid dynamics using the Lagrangian approach, the computational cost still hinders these methods from being practical and efficient for MBS applications (Son, 2005; Sussman et al., 1994; Gingold et al., 1977; Liu et al., 2010, Negrut et al., 2012; Idelsohn et al., 2006; Pin et al., 2007). Therefore, it is the objective of this thesis to address these deficiencies in the literatures by proposing a new approach for solving liquid sloshing problems. The focus will be on the integration of the fluid dynamics in computational MBS

algorithms. A new Lagrangian method which allows for the large displacements of the fluid and the systematic description of the interactions with the other MBS component is proposed. The general finite element FFR and ANCF approach can be used to develop systematically Lagrangian meshes and has the potential for solving efficiently the sloshing problem in MBS applications (Shabana, 1998; Wei et al., 2014).

1.3 Textile Material Modeling

Thorough theoretical study of the roll-drafting process is necessary in order to further improve the polyester filament drawing process. In order to analyze the roll-drafting process, it is necessary to select a proper constitutive law for textile materials, which have been scientifically studied for over 40 years. A brief review on the textile material research is provided in this section.

An early theoretical study on ropes was presented by Vose (1944), who proposed several approaches to examine the behavior of cords and gave brief analytical solutions to some cord problems. Original work on elastic textile materials can be found in a series of publications by Platt et al (1958, 1959), which focused on a single yarn. However, the first constitutive equations of filament bundles were proposed by Curiskis and Carnaby (1985) who treated the filament bundle as a continuum material, thereby allowing for using various mathematical techniques to investigate its mechanical properties. For instance, in Curiskis and Carnaby's work (1985), it is assumed that the filament bundle can be mechanically characterized as a degenerate square-symmetric homogeneous continuum. Pan et al. (1989, 1992) considered the fibers as a transversely isotropic material and performed experiments to obtain mechanical properties of staple yarn (short

fibers). Cai and Gutowski (1992) and Simacek and Karbhari (1996) modeled the filament bundle as a transversely isotropic material in order to analyze some practical problems, such as the filament winding, consolidation, and fiber waviness.

The abovementioned investigations were focused on the textile material behavior, but lacked addressing important practical issues. However, with the aid of computer technology, complex computational filament bundle models were developed using the finite element (FE) method. The mechanic behavior of textile materials was examined using FE analysis by dividing long filament bundles into several meshed elements in several investigations (Luijk et al., 1984; Djaja, 1992; Zhao et al., 2001). The PFB dynamic behavior in a roll-drafting process has also been analyzed recently using planar models (Huh and Kim, 2004, 2006; Kim et al., 2008). These models considered the extension of the fiber along the axial direction but did not consider three-dimensional constitutive equations or cross-section deformations. Other properties such as the thermal effect (Bechtel et al., 2002; Mbarek et al., 2012) and plasticity (Dyke and Hedgepeth, 1969; Jones, 1974; McLaughlin, 1972) of the fiber have also been examined. These properties can be modeled by choosing appropriate stress-strain and strain rate relationships in the constitutive equations.

Textile materials are fairly soft and can lead to large extension, deflection, and bending deformations. In order to analyze complex textile processes, it is necessary to use a large displacement, nonlinear formulation capable of taking into account the effect of rigid body motion. The ANCF is a nonlinear finite element method that can systematically model rigid body motion and large deformation, and allows for using general continuum mechanics constitutive equations.

For large deformation, linear constitutive relationships are not in general adequate, and for this reason, nonlinear theories must be adopted (Maqueda and Shabana, 2007; Jung and Kang, 2005). Fully parameterized ANCF beam finite elements, which employ a complete set of parameters, allow for the use of general constitutive relationships, and therefore, can be used to model the overall orthotropic mechanical behavior of a bundle of fibers, as demonstrated in this thesis in the case of transversely isotropic models in which the material coefficients are assumed constant over the cross section (Pan et al., 1989).

1.4 Scope and Organization of the Thesis

Chapter 2 was first published in the ASME *Journal of Computational and Nonlinear Dynamics* (Wang et al. 2015a) and is reproduced in this thesis with permission which is provided in Appendix A. This chapter addresses the limitation due to the lack of a distributed inertia liquid model that can be effectively used in nonlinear vehicle dynamics. To this end, a reduced order continuum-based total Lagrangian liquid sloshing model that captures the shape of the free surface and the inertia distribution of the liquid due to the sloshing is developed. The FE/FFR formulation, which allows for arbitrary large displacements and captures the inertia coupling between different modes of fluid displacements, is used in the fluid modeling. Crucial to the development presented in this chapter is the definition of the FFR position and velocity gradient tensors that are used to define the fluid strain rates. These strain rates are used to formulate the generalized Navier-Stokes stress forces associated with the fluid modes of displacements. This continuum model is integrated with the spatial MBS algorithms to study the effect of liquid sloshing on the nonlinear dynamics of

railroad vehicles. The use of the proposed method is demonstrated using a simple Newtonian fluid model. It is assumed that the fluid is an incompressible continuum material that has internal energy dissipation due to sloshing. For simplicity, complex fluid behaviors such as vortex and turbulence flow are not considered in this thesis. The simulation scenarios considered in this chapter show that the effect of the distributed inertia of the fluid can be significant. Furthermore, the time-varying inertia and the change in the shape of the fluid due to sloshing can lead to wheel/rail separations that can increase the possibility of vehicle derailments. In order to focus on the main procedures without delving into the details of the integration of shell finite element formulations with complex fluid shapes, a simple rectangular tank car model is used in the simulation scenarios presented in this thesis. Rectangular tank cars have been previously used in the literature (Celebi and Akyildiz, 2001).

Chapter 3 was first published in the ASME *Journal of Computational and Nonlinear Dynamics* (Wei et al. 2015) and is reproduced in this thesis with permission which is provided in Appendix A. This chapter proposes a new approach for modeling fluid problems in which the incompressibility conditions and surface traction forces are considered and derived from the *Navier Stokes* equations. Two ANCF brick finite elements are used, the first is defined using incomplete polynomial representation, while the second is obtained using a B-spline volume geometry. Both ANCF brick elements are described and the effect of applying continuity conditions at the nodal points is examined. This approach allows for modeling arbitrary large displacements, ensures the continuity of the displacement gradients, leads to a constant inertia matrix regardless of the magnitude of the fluid displacements, and allows for efficient and

systematic integration of fluid/MBS algorithms for the study of the liquid sloshing problems. Furthermore, an obvious advantage of the proposed new approach is the ability to handle MBS sloshing problems using a continuum method. The examples presented in this chapter show that fluid simulations can be performed efficiently in the framework of a total Lagrangian formulation. When applicable, comparison is also made with the results obtained using the FFR formulation that employs linear modes.

Chapter 4 was first published in the ASME *Journal of Computational and Nonlinear Dynamics* (Wang et al. 2015b) and is reproduced in this thesis with permission which is provided in Appendix A. This chapter proposes a new MBS approach for modeling the textile process. In order to demonstrate the use of this new approach, the PFB three-dimensional, large deformation behavior during the drawing process is examined using a transversely isotropic hyper-elastic material (Bonet and Burton, 1997; Limbert and Middleton, 2004; Kulkarni et al., 2014). The strain energy for transversely isotropic materials is decomposed into a fully isotropic component and an orthotropic, transversely isotropic component expressed in terms of five invariants of the right Cauchy-Green deformation tensor. Using this energy decomposition, the second Piola-Kirchhoff stress tensor and the tensor of the elastic coefficients can also be split into isotropic and transversely isotropic parts. In order to generalize the strain energy equations to the fully nonlinear regime, the neo-Hookean potential is used to describe the isotropic component of the strain density function, while the orthotropic, transversely isotropic part follows the strain density function defined by Bonet and Burton (1997). The total strain energy function is written in terms of five strain invariants and the resulting constitutive equations are expressed in terms of five independent

coefficients. Different Poisson ratios are used in order to capture the coupling between deformation modes in different directions. The textile machine, composed of rollers, is modeled as a multibody system. The rollers are considered as rigid bodies, whereas the PFB is treated as a flexible body. Constraints and contact forces are used to model the PFB/roller interaction. The computational algorithm developed in this chapter integrates filament bundle transversely isotropic nonlinear material model and ANCF finite elements. The MBS approach presented in this chapter allows for examination of roller contact forces, internal tension of filament bundle, PFB velocity, and filament cross-section deformation. Further phenomena, such as thermal and plastic effects, are not considered in this study and will be the subject of future investigations.

CHAPTER 2

FFR LIQUID SLOSHING MODEL

The objective of this chapter is to develop a low order continuum-based liquid sloshing model that can be successfully integrated with multibody system (MBS) algorithms. The liquid sloshing model proposed in this chapter allows for capturing the effect of the distributed inertia and viscosity of the fluid. The fluid viscous forces are defined using the Navier-Stokes equations. In order to demonstrate the use of the approach presented in this study, the assumption of an incompressible Newtonian fluid is considered with a total Lagrangian approach. Fluid properties such as the incompressibility condition are formulated using a penalty method. The low order model that captures the effect of the distributed fluid inertia on the vehicle dynamics is developed in this chapter using the floating frame reference (FFR) formulation. The use of this approach allows for developing an inertia-variant fluid model that accounts for the dynamic coupling between different modes of the fluid displacements. The matrix of position vector gradients and its derivative are formulated using the FFR kinematic description. The position and velocity gradient tensors are used to define the Navier-Stokes stress forces. The proposed liquid sloshing model is integrated with a MBS railroad vehicle model in which the rail/wheel interaction is formulated using a three-dimensional elastic contact formulation that allows for the wheel/rail separation. Several simulation scenarios are used to examine the effect of the distributed liquid inertia on the motion of the railroad vehicle. The results, obtained using the sloshing model, are compared with the results obtained using a rigid body vehicle model. The comparative numerical study presented in this chapter shows that the effect of the sloshing tends to increase the possibility

of wheel/rail separation as the forward velocity increases, thereby increasing the possibility of derailments at these relatively high speeds.

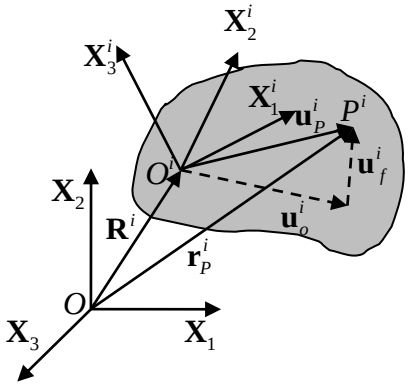

Figure 2. FFR coordinate system

2.1 FFR Fluid Body

The proposed liquid sloshing model developed in this chapter is based on the FE/FFR total Lagrangian formulation. In the FE/FFR formulation, the motion of the fluid body is defined as the motion of its reference frame plus the motion of the material points of the fluid body with respect to its reference, as shown in Fig. 2. Using this kinematic description, the inertia of the liquid can be formulated in terms of a set of constant inertia shape integrals that enter into the formulation of the nonlinear mass matrix of the fluid body. Crucial in the development presented in this section is the definition of the position and velocity gradient tensors required to define the generalized Navier-Stokes stress forces of the fluid body in terms of the FFR generalized coordinates. In this section, the FFR motion description is briefly reviewed and used to define the basic kinematics and forces equations required to develop the low order fluid body model.

2.1.1 FFR Kinematic Description

In order to explain how the position and velocity gradient tensors are formulated in terms of the

FFR generalized coordinates, some basic FFR kinematic equations are first presented. As shown in Fig. FFR coordinate system, the global position vector of an arbitrary point P on a fluid body i can be defined in the spatial analysis as (Shabana, 2014)

$$\mathbf{r}^i = \mathbf{R}^i + \mathbf{A}^i\bar{\mathbf{u}}^i = \mathbf{R}^i + \mathbf{A}^i\left(\bar{\mathbf{u}}_o^i + \bar{\mathbf{u}}_f^i\right) = \mathbf{R}^i + \mathbf{A}^i(\bar{\mathbf{u}}_o^i + \mathbf{S}^i\mathbf{q}_f^i) \tag{1}$$

where $\mathbf{R}^i$ is the global position vector of the origin of the fluid body reference, $\mathbf{A}^i$ is the transformation matrix that defines the orientation of the body reference in the global coordinate system, $\bar{\mathbf{u}}_o^i$ is the position of point P in the undeformed state, $\bar{\mathbf{u}}_f^i$ is the deformation vector, $\mathbf{S}^i = \mathbf{S}^i\left(x_1^i, x_2^i, x_3^i\right)$ is a space-dependent shape matrix, x_1^i, x_2^i, and x_3^i are the spatial coordinates, and $\mathbf{q}_f^i$ is the vector of time-dependent elastic generalized coordinates of the fluid body i. Differentiating Eq. 1 with respect to time yields

$$\dot{\mathbf{r}}^i = \dot{\mathbf{R}}^i + \dot{\mathbf{A}}^i\bar{\mathbf{u}}^i + \mathbf{A}^i\dot{\bar{\mathbf{u}}}^i = \dot{\mathbf{R}}^i + \dot{\mathbf{A}}^i\bar{\mathbf{u}}^i + \mathbf{A}^i\mathbf{S}^i\dot{\mathbf{q}}_f^i \tag{2}$$

The kinetic energy of the fluid body is defined as $T^i = (1/2)\int_{V^i}\rho^i\dot{\mathbf{r}}^{i\mathrm{T}}\dot{\mathbf{r}}^i dV^i$, where ρ^i is the mass density, and V^i is the volume. The vector of time dependent generalized velocities is $\dot{\mathbf{q}}^i = \left[\dot{\mathbf{R}}^{i\mathrm{T}} \;\; \dot{\boldsymbol{\theta}}^{i\mathrm{T}} \;\; \dot{\mathbf{q}}_f^{i\,\mathrm{T}}\right]^{\mathrm{T}}$. The kinetic energy can then be rewritten as $T^i = (1/2)\dot{\mathbf{q}}^{i\mathrm{T}}\mathbf{M}^i\dot{\mathbf{q}}^i$, where $\mathbf{M}^i$ is the symmetric mass matrix of the FFR fluid body. In the FFR formulation, this mass matrix is highly nonlinear regardless of the finite element used.

2.1.2 Incompressible Viscous Newtonian Fluid

Since the main goal of this chapter is to develop a continuum-based fluid body model that can be used to study the effect of liquid sloshing in MBS vehicle dynamics, the assumption of an incompressible Newtonian fluid is sufficient for this purpose. This assumption allows the use of a simple expression for the constitutive relationship in which the stresses are proportional to the

strain rates. While the incompressibility condition is imposed using the penalty method, the Navier-Stokes equations are used to formulate the viscous stress forces. The formulation of these forces requires the use of some basic continuum mechanics concepts and relationships. It is shown in this section how the FFR description can be used to evaluate the continuum mechanics kinematic relationship required to formulate the fluid body forces.

Recall that the determinant of the matrix of position vector gradients $\mathbf{J}^i$ can be written as $J^i = \left|\mathbf{J}^i\right| = \mathbf{r}^i_{x_1} \cdot \left(\mathbf{r}^i_{x_2} \times \mathbf{r}^i_{x_3}\right)$, where $\mathbf{r}^i_{x_i}, i = 1,2,3$, is the gradient vector obtained by differentiation of the position vector $\mathbf{r}^i$ with respect to the spatial coordinate x_i (Spencer, 1980; Bonet and Wood, 1997; Shabana, 2012). In the FFR representation, one can show that the determinant $J^i = \left|\mathbf{J}^i\right| = \mathbf{r}^i_{x_1} \cdot \left(\mathbf{r}^i_{x_2} \times \mathbf{r}^i_{x_3}\right)$ can be written as

$$J^i = \left(\frac{\partial \bar{\mathbf{u}}^i}{\partial x_1}\right) \cdot \left(\frac{\partial \bar{\mathbf{u}}^i}{\partial x_2} \times \frac{\partial \bar{\mathbf{u}}^i}{\partial x_3}\right) = \left(\mathbf{i} + \frac{\partial \mathbf{S}^i}{\partial x_1}\mathbf{q}^i_f\right) \cdot \left(\left(\mathbf{j} + \frac{\partial \mathbf{S}^i}{\partial x_2}\mathbf{q}^i_f\right) \times \left(\mathbf{k} + \frac{\partial \mathbf{S}^i}{\partial x_3}\mathbf{q}^i_f\right)\right) \tag{3}$$

In this equation, $\mathbf{i} = \begin{bmatrix}1 & 0 & 0\end{bmatrix}^{\mathrm{T}}$, $\mathbf{j} = \begin{bmatrix}0 & 1 & 0\end{bmatrix}^{\mathrm{T}}$, and $\mathbf{k} = \begin{bmatrix}0 & 0 & 1\end{bmatrix}^{\mathrm{T}}$. The determinant in the preceding equation is used in many basic continuum mechanics relationships. Recall that $dx_1 dx_2 dx_3 = dV^i$, where dV^i is the volume of an infinitesimal element in the reference configuration. The relationship between the volumes in the current and reference configurations is $dv^i = J^i dV^i$, where v^i is the volume in the current configuration. The incompressibility condition for a fluid body i in the FFR formulation implies that $J^i = \left|\mathbf{J}^i\right| = 1$. It follows that $\dot{J}^i = 0$, an identity that can be utilized to enforce the penalty condition at the velocity level. The 3×3 matrix of position vector gradients at an arbitrary point P can be defined as $\mathbf{J}^i = \partial \mathbf{r}^i / \partial \mathbf{x} = \begin{bmatrix}\partial \mathbf{r}^i / \partial x_1 & \partial \mathbf{r}^i / \partial x_2 & \partial \mathbf{r}^i / \partial x_3\end{bmatrix}$. Using Eq. 1, one has

$$\mathbf{J}^i = \frac{\partial \mathbf{r}^i}{\partial \mathbf{x}} = \mathbf{A}^i \left(\mathbf{I} + \left[\left(\frac{\partial \mathbf{S}^i}{\partial x_1} \right) \mathbf{q}_f^i \quad \left(\frac{\partial \mathbf{S}^i}{\partial x_2} \right) \mathbf{q}_f^i \quad \left(\frac{\partial \mathbf{S}^i}{\partial x_3} \right) \mathbf{q}_f^i \right] \right) \tag{4}$$

This equation can be written compactly as

$$\mathbf{J}^i = \frac{\partial \mathbf{r}^i}{\partial \mathbf{x}} = \mathbf{A}^i \left(\mathbf{I} + \frac{\partial \bar{\mathbf{u}}_f^i}{\partial \mathbf{x}} \right) = \mathbf{A}^i \left(\mathbf{I} + \bar{\mathbf{J}}_d^i \right) \tag{5}$$

In this equation, $\mathbf{x} = \begin{bmatrix} x_1 & x_2 & x_3 \end{bmatrix}^{\mathrm{T}}$, and

$$\bar{\mathbf{J}}_d^i = \frac{\partial \bar{\mathbf{u}}_f^i}{\partial \mathbf{x}} = \left[\left(\frac{\partial \mathbf{S}^i}{\partial x_1} \right) \mathbf{q}_f^i \quad \left(\frac{\partial \mathbf{S}^i}{\partial x_2} \right) \mathbf{q}_f^i \quad \left(\frac{\partial \mathbf{S}^i}{\partial x_3} \right) \mathbf{q}_f^i \right] \tag{6}$$

If the condition $J^i = 1$ is imposed, one has

$$J^i = \left| \mathbf{J}^i \right| = \left| \mathbf{J}_r^i \mathbf{J}_d^i \right| = \left| \mathbf{A}^i \right| \left| \mathbf{I} + \bar{\mathbf{J}}_d^i \right| = \left| \mathbf{I} + \bar{\mathbf{J}}_d^i \right| = 1 \tag{7}$$

where $\mathbf{J}_r^i = \mathbf{A}^i$ is the Jacobian matrix associated with the rigid body rotation, and $\mathbf{J}_d^i = \left(\mathbf{I} + \bar{\mathbf{J}}_d^i \right)$ is the Jacobian matrix associated with the fluid body deformation. If the condition $\dot{J}^i = 0$ is imposed, the time derivative of $\dot{J}^i$ can be evaluated as

$$\dot{J}^i = \sum_{k=1}^{3} \frac{\partial \dot{r}_k^i}{\partial r_k} J^i = \left(\frac{\partial \dot{r}_1^i}{\partial r_1} + \frac{\partial \dot{r}_2^i}{\partial r_2} + \frac{\partial \dot{r}_3^i}{\partial r_3} \right) J^i = \mathrm{tr}\left(\mathbf{D}^i \right) J^i \tag{8}$$

where $\mathbf{D}^i$ is the rate of deformation tensor, and $\left(\partial \dot{r}_i / \partial r_i \right) = \sum_{k=1}^{3} \left(\partial \dot{r}_i / \partial x_k \right) \left(\partial x_k / \partial r_i \right)$. One also has $\mathbf{J}^{-1} = \partial \mathbf{x} / \partial \mathbf{r} = \left[\partial \mathbf{x} / \partial r_1 \quad \partial \mathbf{x} / \partial r_2 \quad \partial \mathbf{x} / \partial r_3 \right]$, and $\dot{\mathbf{J}} = \partial \dot{\mathbf{r}} / \partial \mathbf{x} = \left[\partial \dot{\mathbf{r}} / \partial x_1 \quad \partial \dot{\mathbf{r}} / \partial x_2 \quad \partial \dot{\mathbf{r}} / \partial x_3 \right]$. Therefore, Eq. 8 can be written as $\dot{J}^i = \left(\dot{\mathbf{J}}^i : \left(\mathbf{J}^{i^{-1}} \right)^{\mathrm{T}} \right) J^i$, where in the FFR formulation, $\dot{\mathbf{J}}^i = \dot{\mathbf{A}}^i \left[\mathbf{I} + \bar{\mathbf{J}}_d^i \right] + \mathbf{A}^i \dot{\bar{\mathbf{J}}}_d^i$.

2.1.3 FFR Navier-Stokes Generalized Stress Forces

If the fluid is assumed to be *isotropic*, one can write the following fluid constitutive equations $\boldsymbol{\sigma}^i = \left\{ -P^i + \lambda \mathrm{tr}\left(\mathbf{D}^i \right) \right\} \mathbf{I} + 2\mu \mathbf{D}^i$ (Spencer, 1980; Bonnet and wood, 1997; and Shabana, 2012),

where λ and μ are viscosity coefficients that depend on the fluid density and temperature, $\boldsymbol{\sigma}^i$ is the Cauchy stress tensor, P^i is the hydrostatic pressure, and the symmetric rate of deformation tensor $\mathbf{D}^i$ can be expressed in terms of the Lagrangian strain rate $\dot{\boldsymbol{\varepsilon}}^i$ as $\mathbf{D}^i = \left(\mathbf{J}^i\right)^{-1^{\mathrm{T}}} \dot{\boldsymbol{\varepsilon}}^i \left(\mathbf{J}^i\right)^{-1}$, where $\mathbf{J}^i$ is the matrix of position vector gradients. It is clear from the preceding equation that if the velocity gradients are equal to zero, the shear stresses are equal to zero; and the normal stress components reduce to the hydrostatic pressure P^i. In the aforementioned fluid equation, μ is the *coefficient of shear viscosity*, and $\left(\lambda + \left(2\mu/3\right)\right)$ is called the *coefficient of bulk viscosity*. If $\lambda + \left(2\mu/3\right) = 0$, on has the *Stokes' relation*. For *incompressible fluids,* $J^i = 1$, and since $\mathrm{tr}\left(\mathbf{D}^i\right) = \dot{J}^i / J^i$, it follows that $\mathrm{tr}\left(\mathbf{D}^i\right) = 0$. Consequently, imposing the incompressibility condition at the velocity level $\dot{J}^i = 0$ ensures that $\mathrm{tr}\left(\mathbf{D}^i\right) = 0$. In this special case, the mass density ρ is constant, and the fluid constitutive equation reduces to $\boldsymbol{\sigma}^i = -P^i\mathbf{I} + 2\mu\mathbf{D}^i$. One can also show that in the case of incompressible fluid, enforcing the condition $J^i = 1$, allows for the use of the Navier-Stokes stress relationship $\boldsymbol{\sigma}^i = 2\mu\mathbf{D}^i$.

In general, the virtual work of the fluid stress forces can be written as

$$\delta W_s^i = -\int_{v^i} \boldsymbol{\sigma}^i : \delta\mathbf{J}^i dv^i = -\int_{V^i} \boldsymbol{\sigma}_{P2}^i : \delta\boldsymbol{\varepsilon}^i dV^i \tag{9}$$

In this equation, v^i is the volume in the current configuration, and $\boldsymbol{\sigma}_{P2}^i = J^i\left(\left(\mathbf{J}^i\right)^{-1}\boldsymbol{\sigma}^i\left(\mathbf{J}^i\right)^{-1^{\mathrm{T}}}\right)$ is the second Piola-Kirchhoff stress tensor. One can also write the virtual work of the stress forces as $\delta W_s^i = -\int_{V^i} J^i\boldsymbol{\sigma}^i : \delta\mathbf{J}^i dV^i$ in order to allow performing the integration over the volume in the reference configuration. The virtual change in the strain tensor can be written as $\delta\boldsymbol{\varepsilon}^i = \left(1/2\right)\left(\left(\delta\mathbf{J}_d^{i\,\mathrm{T}}\right)\mathbf{J}_d^i + \mathbf{J}_d^{i\,\mathrm{T}}\delta\mathbf{J}_d^i\right)$. This equation can also be written in the form

$\delta\boldsymbol{\varepsilon}^i = (1/2)\left(\left(\delta\bar{\mathbf{J}}_d^{i\,\mathrm{T}}\right)\mathbf{J}_d^i + \mathbf{J}_d^{i\,\mathrm{T}}\delta\bar{\mathbf{J}}_d^i\right)$. Using the FFR kinematic description to define the tensor $\bar{\mathbf{J}}_d^i$, the virtual change in the strain tensor can be written as

$$\delta\boldsymbol{\varepsilon}^i = \frac{1}{2}\left(\left(\delta\left(\frac{\partial\bar{\mathbf{u}}_f^i}{\partial\mathbf{x}}\right)^{\mathrm{T}}\right)\mathbf{J}_d^i + \mathbf{J}_d^{i\,\mathrm{T}}\delta\left(\frac{\partial\bar{\mathbf{u}}_f^i}{\partial\mathbf{x}}\right)\right) \tag{10}$$

It follows that

$$\delta\left(\frac{\partial\bar{\mathbf{u}}_f^i}{\partial\mathbf{x}}\right) = \delta\left[\frac{\partial\bar{\mathbf{u}}_f^i}{\partial x_1} \quad \frac{\partial\bar{\mathbf{u}}_f^i}{\partial x_2} \quad \frac{\partial\bar{\mathbf{u}}_f^i}{\partial x_3}\right] = \left[\left(\frac{\partial\mathbf{S}^i}{\partial x_1}\delta\mathbf{q}_f^i\right) \quad \left(\frac{\partial\mathbf{S}^i}{\partial x_2}\delta\mathbf{q}_f^i\right) \quad \left(\frac{\partial\mathbf{S}^i}{\partial x_3}\delta\mathbf{q}_f^i\right)\right] \tag{11}$$

The preceding two equations, which show that $\delta\boldsymbol{\varepsilon}^i$ can be written as a linear function in $\delta\mathbf{q}_f^i$, can be used to write the virtual work of the FFR Navier-Stokes generalized forces as

$$\delta W_s^i = -\int_{V^i}\boldsymbol{\sigma}_{P2}^i : \delta\boldsymbol{\varepsilon}^i dV^i = \mathbf{Q}_{ns}^i\delta\mathbf{q}_f^i \tag{12}$$

Alternatively, one can use directly the expression $\delta W_s^i = -\int_{V^i} J^i\boldsymbol{\sigma}^i : \delta\mathbf{J}^i dV^i$, where $\delta\mathbf{J}^i$ can be determined using Eq. 4. The FFR Navier-Stokes generalized force vector $\mathbf{Q}_{ns}^i$ can be introduced to the dynamic equations that govern the motion of the FFR fluid body.

2.1.4 FFR Incompressibility Generalized Forces

In this chapter, the penalty method is used to formulate the FFR generalized forces resulting from the conditions $J^i = 1$ and $\dot{J}^i = 0$. A strain energy function $U_{IC}^i = (1/2)k\left(J^i - 1\right)^2$ is used to enforce the incompressibility condition $J^i = 1$, where k is a stiffness coefficient. One can also impose the incompressibility condition at the velocity level by formulating the dissipation function $U_{DP}^i = (1/2)c\left(\dot{J}^i\right)^2$ resulting from the condition $\dot{J}^i = 0$, where c is a damping coefficient. The stiffness and damping coefficients k and c can be selected to ensure that the incompressibility

condition is satisfied. Using U_{IC} and U_{DP}, the penalty forces from incompressibility condition can be obtained by differentiation with respect to the FFR elastic coordinates and velocities as

$$\left.\begin{aligned}\mathbf{Q}_{IC}^{i\mathrm{T}} &= \frac{\partial U_{IC}^{i}}{\partial \mathbf{q}_f^i} = k\left(J^i - 1\right)\frac{\partial J^i}{\partial \mathbf{q}_f^i} \\ \mathbf{Q}_{DP}^{i\mathrm{T}} &= \frac{\partial U_{DP}^{i}}{\partial \dot{\mathbf{q}}_f^i} = c\dot{J}^i \frac{\partial \dot{J}^i}{\partial \dot{\mathbf{q}}_f^i}\end{aligned}\right\} \tag{13}$$

The definition $J^i = \left|\mathbf{J}^i\right| = \mathbf{r}_{x_1}^i \cdot \left(\mathbf{r}_{x_2}^i \times \mathbf{r}_{x_3}^i\right)$ and the use of basic cross product identities lead to

$$\frac{\partial J^i}{\partial \mathbf{q}_f^i} = \frac{\partial \dot{J}^i}{\partial \dot{\mathbf{q}}_f^i} = \left(\frac{\partial \bar{\mathbf{u}}_f^i}{\partial x_2} \times \frac{\partial \bar{\mathbf{u}}_f^i}{\partial x_3}\right)^{\mathrm{T}} \frac{\partial \mathbf{S}^i}{\partial x_1} + \left(\frac{\partial \bar{\mathbf{u}}_f^i}{\partial x_3} \times \frac{\partial \bar{\mathbf{u}}_f^i}{\partial x_1}\right)^{\mathrm{T}} \frac{\partial \mathbf{S}^i}{\partial x_2} + \left(\frac{\partial \bar{\mathbf{u}}_f^i}{\partial x_1} \times \frac{\partial \bar{\mathbf{u}}_f^i}{\partial x_2}\right)^{\mathrm{T}} \frac{\partial \mathbf{S}^i}{\partial x_3} \tag{14}$$

This equation can be used to define the generalized penalty forces associated with the generalized FFR coordinates. Note that when the incompressibility condition is used, the element mass dm^i can be expressed in the reference and current configurations as $dm^i = \rho_0^i dV^i = \rho^i dv^i$, where ρ_0^i and ρ^i are, respectively, the mass density in the reference and current configurations. Because $dv^i = J^i dV^i$, it is clear that $\rho_0^i = \rho^i J^i$. In the case of incompressible materials for fluid body i, $J^i = \left|\mathbf{J}^i\right| = 1$. It follows that $\rho_0^i = \rho^i$, which implies that the mass density remains constant. This allows carrying out the integration required to determine the mass matrix and inertia forces of the FFR fluid body using properties defined in the reference configuration.

2.1.5 Dynamic Equations

The equations of equilibrium for the fluid body i can be written in a vector form as

$$\left(\nabla \boldsymbol{\sigma}^{i\mathrm{T}}\right)^{\mathrm{T}} + \mathbf{f}_b^i - \rho^i \mathbf{a}^i = \mathbf{0} \tag{15}$$

In this equation, $\mathbf{f}_b^i$ is the vector of body forces, and $\mathbf{a}^i = \ddot{\mathbf{r}}^i$ is the vector of absolute acceleration of an arbitrary point on the fluid body. In order to solve this partial differential equation that

depends on space and time, the principle of virtual work and approximation techniques are used to convert the partial differential equations to a set of discrete ordinary differential equations. In order to evaluate the virtual work of forces, the preceding equation is multiplied by $\delta\mathbf{r}^i$ and integrated over the current volume leading to $\int_{v^i}\left[\left(\nabla\boldsymbol{\sigma}^{i\mathrm{T}}\right)^{\mathrm{T}}+\mathbf{f}_b^i-\rho^i\mathbf{a}^i\right]^{\mathrm{T}}\delta\mathbf{r}^i dv^i=0$. Using Gauss theorem, one obtains

$$\int_{s^i}\mathbf{n}^{i\mathrm{T}}\boldsymbol{\sigma}^i\delta\mathbf{r}^i ds^i-\int_{v^i}\boldsymbol{\sigma}^i:\left(\delta\mathbf{J}^i\right)\left(\mathbf{J}^i\right)^{-1}dv^i+\int_{v^i}\mathbf{f}_b^{i\mathrm{T}}\delta\mathbf{r}^i dv^i-\int_{v^i}\left(\rho^i\mathbf{a}^i\right)^{\mathrm{T}}\delta\mathbf{r}^i dv^i=0 \tag{16}$$

In this equation, $\mathbf{n}^i$ is the unit normal on a surface s^i. The first term in this equation represents the virtual work of surface traction forces, the second term is the virtual work of internal viscous forces, the third term is the virtual work of body forces, and the last term is the virtual work of inertia forces**.** The virtual work of inertia force can be written as $\delta W_i^i=\int_{V^i}\rho^i\ddot{\mathbf{r}}^{i\mathrm{T}}\delta\mathbf{r}^i dV^i$ and the virtual work of the body force is defined as $\delta W_e^{\ i}=\int_{V^i}\mathbf{f}_b^{i\mathrm{T}}\delta\mathbf{r}^i dV^i=\mathbf{Q}_e^{i\mathrm{T}}\delta\mathbf{q}^i$, where $\mathbf{Q}_e^i$ is the external generalized force vector. If $\mathbf{Q}_{FB}^i$ denotes the viscous and penalty forces, the fluid body Lagrange-D'Alembert equations can be written as.

$$\int_{V^i}\rho^i\ddot{\mathbf{r}}^{i\mathrm{T}}\delta\mathbf{r}^i dV=\left(\mathbf{Q}_{FB}^i\right)_f^{\mathrm{T}}\delta\mathbf{q}_f^i+\mathbf{Q}_e^{i\mathrm{T}}\delta\mathbf{q}^i \tag{17}$$

This equation will be used to couple the fluid dynamics with the dynamics of the multibody vehicle system.

2.2 FE/FFR Low Order Fluid Body Model

The equations that govern the flow of fluids are partial differential equations, which are functions of the flow variables and their derivatives. Furthermore, in the case of tank car sloshing, the fluid

can be subjected to arbitrary displacements. Therefore, for such problems the use of FE/MBS algorithms is recommended in order to be able to accurately define the fluid inertia and its effect on the dynamics of the vehicle system. Using a FE/MBS approach based on the FFR formulation, the fluid inertia can be expressed in terms of a set of constant inertia shape integrals that enter into the formulation in the nonlinear fluid mass matrix. This approach also allows for reducing the number of coordinates of the fluid body using conventional modal reduction methods.

2.2.1 Hexahedral Element and Finite Element Coordinate Systems

In a general MBS approach based on the FE/FFR formulation, a deformable body is normally divided into more than one element. In this chapter, superscript ij refers to an element j on the fluid body i. Using the finite element coordinate systems shown in Fig.3, a systematic and efficient procedure can be developed to study the effect of the distributed inertia of the fluid body.

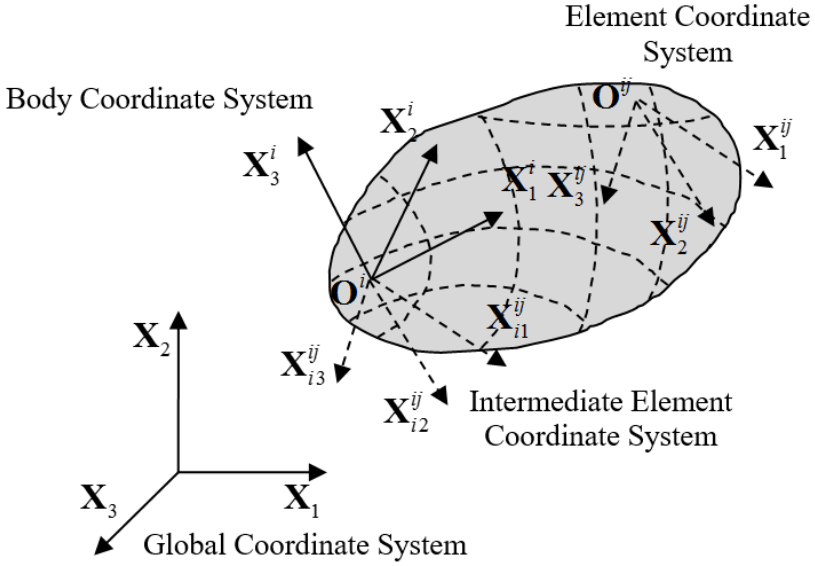

Figure 3. Finite element coordinate systems

In Fig. 3, $\mathbf{X}_1^{ij}\mathbf{X}_2^{ij}\mathbf{X}_3^{ij}$ is the element coordinate system that translates and rotates with the element and has an origin rigidly attached to a point on the element; $\mathbf{X}_1^{i}\mathbf{X}_2^{i}\mathbf{X}_3^{i}$ is the fluid body coordinate system that need not to be rigidly attached to a point on the body; $\mathbf{X}_{i1}^{ij}\mathbf{X}_{i2}^{ij}\mathbf{X}_{i3}^{ij}$ is an intermediate element coordinate system whose origin is rigidly attached to the origin of the body $\mathbf{X}_1^{i}\mathbf{X}_2^{i}\mathbf{X}_3^{i}$ coordinate system and is assumed to have a fixed orientation with respect to the body coordinate system. Using these coordinate systems, the position coordinates of an arbitrary point on the finite element with respect to the origin of the fluid body coordinate system can be written as $\bar{\mathbf{u}}^{ij} = \mathbf{C}^{ij}\mathbf{S}^{ij}\mathbf{e}_i^{ij} = \mathbf{C}^{ij}\mathbf{S}^{ij}\bar{\mathbf{C}}^{ij}\mathbf{q}_n^{ij}$. In this equation, $\mathbf{C}^{ij}$ is a transformation matrix that defines the orientation of the element coordinate system with respect to the body coordinate system, $\bar{\mathbf{C}}^{ij}$ is the orthogonal constant transformation matrix, the dimension of which depends on the number of nodal coordinates of the element, $\mathbf{S}^{ij}$ is the element shape function, $\mathbf{q}_n^{ij} = \mathbf{q}_0^{ij} + \mathbf{q}_f^{ij}$ is the vector of nodal coordinates of element ij defined with respect to the coordinate system of the fluid body i, and $\mathbf{q}_0^{ij}$ is the vector of nodal coordinates in the reference configuration (Shabana, 2014).

While the FFR formulation presented in this study allows for the use of any finite element including conventional structural elements that employ infinitesimal rotations as nodal coordinates, in the numerical study presented in this chapter, a standard hexahedral element is used in the analysis of three-dimensional viscous flow problems. The element used is the 8-node linear brick element. In this case, without loss of generality, the element coordinate system is assumed to be parallel to the body coordinate system, $\mathbf{C}^{ij} = \mathbf{I}_{3\times 3}$ and $\bar{\mathbf{C}}^{ij} = \mathbf{I}_{24\times 24}$. The shape function matrix $\mathbf{S}^{ij}$ of the brick element can be written as $\mathbf{S} = \left[s_1\mathbf{I}\ s_2\mathbf{I}\ s_3\mathbf{I}\ s_4\mathbf{I}\ s_5\mathbf{I}\ s_6\mathbf{I}\ s_7\mathbf{I}\ s_8\mathbf{I}\right]$, where $\mathbf{I}$ is a 3 × 3

identity matrix and $s_i, i=1,2,\cdots,8$, are $s_1=1/8(1+\xi)(1-\eta)(1-\varsigma)$, $s_2=1/8(1+\xi)(1+\eta)(1-\varsigma)$, $s_3=1/8(1-\xi)(1+\eta)(1-\varsigma)$, $s_4=1/8(1-\xi)(1-\eta)(1-\varsigma)$, $s_5=1/8(1+\xi)(1-\eta)(1+\varsigma)$, $s_6=1/8(1+\xi)(1+\eta)(1+\varsigma)$, $s_7=1/8(1-\xi)(1+\eta)(1+\varsigma)$, $s_8=1/8(1-\xi)(1-\eta)(1+\varsigma)$, where $\xi=x_1/a$, $\eta=x_2/b$, $\varsigma=x_3/c$, and $2a$, $2b$, $2c$ are the dimensions of the element in three directions.

2.2.2 FFR Fluid Element Mass Matrix

Using the definition $\mathbf{N}^{ij}=\mathbf{C}^{ij}\mathbf{S}^{ij}\bar{\mathbf{C}}^{ij}\mathbf{B}_1^{ij}$, where $\mathbf{B}_1^{ij}$ is a constant Boolean transformation which defines the connectivity of the element, and assuming that $\mathbf{B}_2^{i}$ is a linear transformation that arises from imposing the reference conditions, the mass matrix of the fluid finite element j of the fluid body i can be written as (Shabana, 2014)

$$\mathbf{M}^{ij}=\begin{bmatrix}\mathbf{m}_{RR}^{ij} & \mathbf{m}_{R\theta}^{ij} & \mathbf{m}_{Rf}^{ij}\\ & \mathbf{m}_{\theta\theta}^{ij} & \mathbf{m}_{\theta f}^{ij}\\ \textit{Sym.} & & \mathbf{m}_{ff}^{ij}\end{bmatrix}=\int_{V^{ij}}\rho^{ij}\begin{bmatrix}\mathbf{I} & -\mathbf{A}^{i}\tilde{\bar{\mathbf{u}}}^{ij}\bar{\mathbf{G}}^{i} & \mathbf{A}^{i}\mathbf{N}^{ij}\mathbf{B}_2^{i}\\ & \bar{\mathbf{G}}^{i\mathrm{T}}\tilde{\bar{\mathbf{u}}}^{ij\mathrm{T}}\tilde{\bar{\mathbf{u}}}^{ij}\bar{\mathbf{G}}^{i} & \bar{\mathbf{G}}^{i\mathrm{T}}\tilde{\bar{\mathbf{u}}}^{ij\mathrm{T}}\mathbf{N}^{ij}\mathbf{B}_2^{i}\\ \mathrm{sym.} & & \mathbf{B}_2^{i\mathrm{T}}\mathbf{N}^{ij\mathrm{T}}\mathbf{N}^{ij}\mathbf{B}_2^{i}\end{bmatrix}dV^{ij} \tag{18}$$

where $\mathbf{I}$ is a 3×3 identity matrix, $\bar{\mathbf{G}}^{i}$ is the matrix that relates the angular velocity vector to the time derivatives of the orientation parameters. This matrix, which can be written in terms of the orientation parameters $\boldsymbol{\theta}^{i}$, can be nonlinear in the orientation parameters if Euler angles are used. This matrix also accounts for the effect of the dynamic coupling between the large reference displacements of the fluid and its movements with respect to its reference. The mass matrix of the fluid body can be obtained by assembling the mass matrices of its elements (Shabana, 2014).

2.2.3 Low Order Fluid Body Model

As previously mentioned, the goal of this chapter is to develop an FFR/MBS low order model for liquid sloshing that allows for accurately capturing the effect of the distributed fluid inertia on the dynamics of vehicle systems. In this case, some important modes of the fluid displacements can be identified and used to define the fluid inertia in the MBS algorithm. This approach, which captures the effect of the distributed inertia of the fluid, allows for developing more accurate liquid sloshing models as compared to the discrete inertia pendulum models used in the literature.

As the finite element discretization of the fluid results in a large number of nodal coordinates, component mode synthesis methods can be used to reduce the number of coordinates. This can be accomplished systematically because the FFR formulation allows for defining a local linear problem. The modes of displacement of the fluid can be assumed by the analyst. Another alternate approach, that is more systematic, is to define a fluid body FE mesh at a pre-processing stage and assume certain stiffness parameters to define a mesh local stiffness matrix $\mathbf{K}_{ff}^{i}$. The explicit expression for the stiffness matrix for element j of the fluid body i is defined as $\mathbf{K}_{ff}^{ij} = \int_{V^{ij}} (\mathbf{D}^{ij}\bar{\mathbf{N}}^{ij})^{\mathrm{T}} \mathbf{E}^{ij} (\mathbf{D}^{ij}\bar{\mathbf{N}}^{ij}) dV^{ij}$, where $\mathbf{D}^{ij}$ is a spatial derivative operator relating strains and displacements, and $\mathbf{E}^{ij}$ is the matrix of elastic coefficients. The stiffness parameters are obtained from the constitutive model of conventional structural mechanics in which the Possion ratio is assumed to be 0.49 for the incompressible material and the bulk modulus is $2.2\times10^{9}\,\mathrm{Pa}$. This local stiffness matrix is only used at a preprocessing stage to identify possible modes of displacements of the fluid. That is, this stiffness matrix is not used in the equations of motion of

the fluid and it is used only to determine the assumed displacement modes. This approach can also be used in the case of compressible fluid in which J^i can vary from one.

If the fluid is assumed to vibrate freely with respect to its reference, one has $\mathbf{m}^i_{ff}\ddot{\mathbf{q}}^i_f + \mathbf{K}^i_{ff}\mathbf{q}^i_f = \mathbf{0}$, where $\mathbf{m}^i_{ff}$ is the assembled matrix of the element $\mathbf{m}^{ij}_{ff}$ matrices. This equation can be used to determine the mode shapes (assumed modes of displacements). The mode shapes can be used to form the modal matrix $\bar{\mathbf{\Phi}}^i_n$, which has a number of columns n_f equal to the number of elastic nodal coordinates of the fluid. A reduced order model can be achieved by solving only for n_m mode shapes. A coordinate transformation from the physical nodal coordinates to the modal elastic coordinates using n_m modes can be written as $\mathbf{q}^i_f = \bar{\mathbf{\Phi}}^i_m \mathbf{p}^i_f$, where $\bar{\mathbf{\Phi}}^i_m$ is the modal transformation matrix, whose columns are the selected n_m fundamental mode shapes, and $\mathbf{p}^i_f$ is the n_m-vector of modal coordinates.

While this approach defines low order model for the fluid body, it has several clear advantages. It is a more realistic model as compared to the discrete inertia models that employ pendulum systems, it allows for capturing the fluid body distributed inertia, it allows for studying the contribution of each mode of displacement on the vehicle dynamics and identifying the modes that are the cause of accidents, and it can be systematically integrated into the computational algorithms implemented in most commercial MBS computer programs.

2.3 Integration with MBS Algorithms

This section explains the procedure for integrating the viscous fluid model with computational MBS algorithms which are designed to solve a system of differential/algebraic equations (DAE's). The differential equations define the system equations of motion, while the algebraic equations

define the kinematic constraints that describe mechanical joints and specified motion trajectories. These constraint functions can be written in a vector form as $\mathbf{C}(\mathbf{q},t)=\mathbf{0}$, where $\mathbf{q}$ is the total vector of system generalized coordinates, t is time, $\mathbf{C}$ is the vector of linearly independent constraint functions. The virtual change in the generalized coordinates leads to $\mathbf{C}_\mathbf{q}\delta\mathbf{q}=\mathbf{0}$, where $\mathbf{C}_\mathbf{q}$ is the constraint Jacobian matrix.

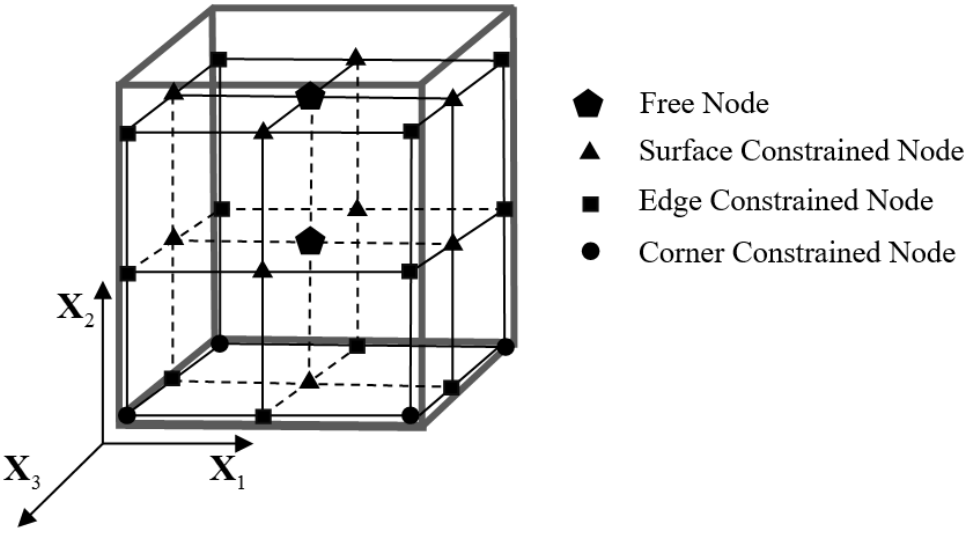

Figure 4. Fluid element boundary constraints

2.3.1 Fluid Boundary Constraints

In the finite element analysis, the global mass and stiffness matrices of the fluid body are obtained by assembling the element mass and stiffness matrices of its finite elements. The linear brick element used in this chapter has three translational degrees of freedom (DOFs) per node. The conditions imposed on the surface nodes of the fluid in a rectangular container can be classified into four different types: free nodes, surface constrained nodes, edge constrained nodes, and corner constrained nodes. In order to demonstrate the differences between different nodes, Fig. 4 depicts

a simplified fluid model having eight elements that includes all these four conditions. Each of the free nodes has three translational degrees of freedom at that node and this node can move freely subject to the incompressibility condition only. A surface node has two degrees of freedom that allow the node to move on that surface without penetration or separation. An edge node has only one degree of freedom along that edge allowing the node to move along the edge of the tank only. A corner node has all degrees of freedom fixed to the fluid body coordinate system.

2.3.2 System Equations of Motion

Using Eqs. 3 and 15 and the expression for damping forces, one can write the constrained MBS dynamic equations of motion of the fluid body as

$$\mathbf{M}^i\ddot{\mathbf{q}}^i + \mathbf{C}^{\mathrm{T}}_{\mathbf{q}^i}\boldsymbol{\lambda} = \mathbf{Q}^i_e + \mathbf{Q}^i_v + \mathbf{Q}^i_{FB}, \quad i = 1, 2..., n_b \tag{19}$$

where n_b is the total number of bodies in the system, $\mathbf{C}_{\mathbf{q}^i}$ is the constraint Jacobian matrix, $\boldsymbol{\lambda}$ is the vector of Lagrange multipliers, and $\mathbf{Q}^i_v$ is a quadratic velocity vector that absorbs Coriolis and centrifugal forces. The preceding equation can be written in a partitioned matrix form as follows:

$$\begin{bmatrix} \mathbf{m}^i_{RR} & \mathbf{m}^i_{R\theta} & \mathbf{m}^i_{Rf} \\ & \mathbf{m}^i_{\theta\theta} & \mathbf{m}^i_{\theta f} \\ \text{sym.} & & \mathbf{m}^i_{ff} \end{bmatrix} \begin{bmatrix} \ddot{\mathbf{R}}^i \\ \ddot{\boldsymbol{\theta}}^i \\ \ddot{\mathbf{q}}^i_f \end{bmatrix} + \begin{bmatrix} \mathbf{C}^{\mathrm{T}}_{\mathbf{R}^i} \\ \mathbf{C}^{\mathrm{T}}_{\boldsymbol{\theta}^i} \\ \mathbf{C}^{\mathrm{T}}_{\mathbf{q}^i_f} \end{bmatrix} \boldsymbol{\lambda} = \begin{bmatrix} \left(\mathbf{Q}^i_e\right)_R \\ \left(\mathbf{Q}^i_e\right)_\theta \\ \left(\mathbf{Q}^i_e\right)_f \end{bmatrix} + \begin{bmatrix} \left(\mathbf{Q}^i_v\right)_R \\ \left(\mathbf{Q}^i_v\right)_\theta \\ \left(\mathbf{Q}^i_v\right)_f \end{bmatrix} + \begin{bmatrix} \mathbf{0} \\ \mathbf{0} \\ \left(\mathbf{Q}^i_{FB}\right)_f \end{bmatrix}, \quad i = 1, 2..., n_b \tag{20}$$

This equation represents a system of second-order differential equations whose solution has to satisfy the algebraic constraint equations $\mathbf{C}(\mathbf{q}, t) = \mathbf{0}$. This mixed system of differential and algebraic equations has to be solved simultaneously. The preceding equation can be systematically

integrated with MBS algorithms to study the effect of the liquid inertia on the dynamics of railroad vehicle systems. This equation allows for arbitrary displacement of the fluid container.

Using component mode synthesis techniques discussed in preceding section, the preceding equation can be written in terms of modal coordinates as

$$\begin{bmatrix} \bar{\mathbf{m}}^i_{rr} & \bar{\mathbf{m}}^i_{rf} \\ \bar{\mathbf{m}}^i_{fr} & \bar{\mathbf{m}}^i_{ff} \end{bmatrix} \begin{bmatrix} \ddot{\mathbf{p}}^i_r \\ \ddot{\mathbf{p}}^i_f \end{bmatrix} + \begin{bmatrix} \mathbf{C}^{\mathrm{T}}_{\mathbf{p}^i_r} \\ \mathbf{C}^{\mathrm{T}}_{\mathbf{p}^i_f} \end{bmatrix} \boldsymbol{\lambda} = \begin{bmatrix} \left(\bar{\mathbf{Q}}^i_e\right)_r \\ \left(\bar{\mathbf{Q}}^i_e\right)_f \end{bmatrix} + \begin{bmatrix} \left(\bar{\mathbf{Q}}^i_v\right)_r \\ \left(\bar{\mathbf{Q}}^i_v\right)_f \end{bmatrix} + \begin{bmatrix} \mathbf{0} \\ \left(\bar{\mathbf{Q}}^i_{FB}\right)_f \end{bmatrix}, \quad i = 1, 2..., n_b \tag{21}$$

where subscript r refers to reference, $\bar{\mathbf{m}}^i_{rr} = \mathbf{m}^i_{rr}$, $\bar{\mathbf{m}}^i_{rf} = \bar{\mathbf{m}}^{i\mathrm{T}}_{fr} = \mathbf{m}^i_{rf}\bar{\boldsymbol{\Phi}}^i_m$, $\bar{\mathbf{m}}^i_{ff} = \bar{\boldsymbol{\Phi}}^{i\mathrm{T}}_m \mathbf{m}^i_{ff}\bar{\boldsymbol{\Phi}}^i_m$, $\bar{\mathbf{C}}^i_D = \bar{\boldsymbol{\Phi}}^{i\mathrm{T}}_m \mathbf{C}^i_D \bar{\boldsymbol{\Phi}}^i_m$, $\left(\bar{\mathbf{Q}}^i_e\right)_r = \left(\mathbf{Q}^i_e\right)_r$, $\left(\bar{\mathbf{Q}}^i_e\right)_f = \bar{\boldsymbol{\Phi}}^{i\mathrm{T}}_m \left(\mathbf{Q}^i_e\right)_f$, $\left(\bar{\mathbf{Q}}^i_v\right)_r = \left(\mathbf{Q}^i_v\right)_r$, $\left(\bar{\mathbf{Q}}^i_v\right)_f = \bar{\boldsymbol{\Phi}}^{i\mathrm{T}}_m \left(\mathbf{Q}^i_v\right)_f$, $\mathbf{C}_{\mathbf{p}^i_r} = \mathbf{C}_{\mathbf{q}^i_r}$, $\mathbf{C}_{\mathbf{p}^i_f} = \mathbf{C}_{\mathbf{q}^i_f}\bar{\boldsymbol{\Phi}}^i_m$, and $\left(\bar{\mathbf{Q}}^i_{FB}\right)_f = \bar{\boldsymbol{\Phi}}^{i\mathrm{T}}_m \left(\mathbf{Q}^i_{FB}\right)_f$ (Shabana, 2014). In this equation, n_m can be significantly less than n_f.

2.4 Numerical Examples

In this section, different computer simulation scenarios are used to examine the effect of the time-variant distributed inertia due to liquid sloshing on railroad vehicle dynamics. In order to increase the effect of the sloshing, in some simulation scenarios, the forward velocity of the vehicle is increased to initiate flange contacts. In some other examples, an initial lateral velocity is used to initiate the hunting motion. A sudden increase of the vehicle velocity is also considered to make the effect of the liquid inertia on the vehicle dynamics more predominant. The data of the railroad vehicle model used in this chapter are the same as the data of the model used by Shabana et al. (2008).

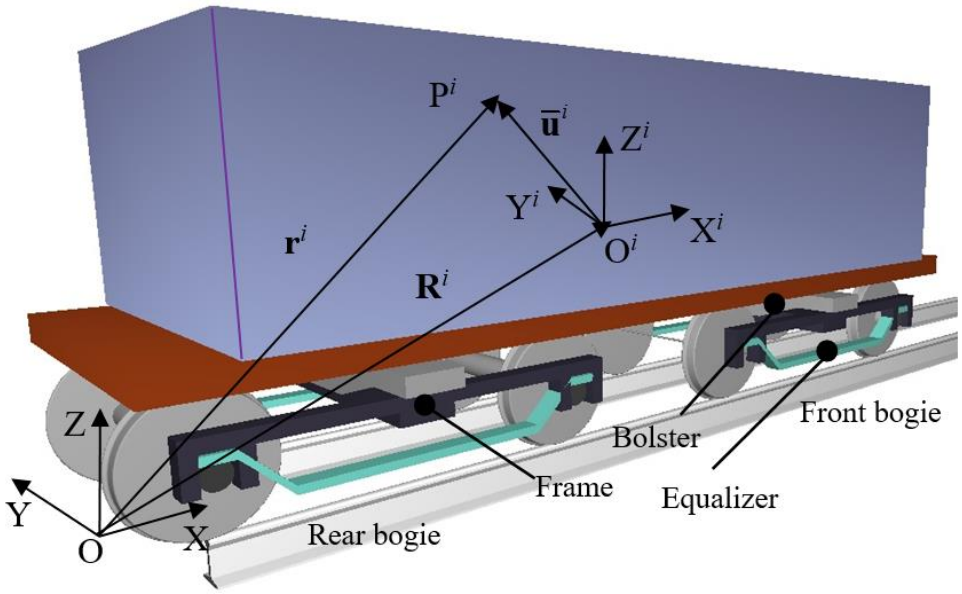

Figure 5. Railroad Vehicle model

2.4.1 Description of the Model

The vehicle model used to examine the sloshing effect is shown in Fig.5. This MBS vehicle model has 15 bodies, 14 of which are rigid bodies and one is a fluid body that represents a water tank. One rigid body is the rail which is fixed to the ground. There are two bogies, each of which consists of 6 bodies; two wheelsets: two equalizers on both sides connected to the wheelsets by bearing elements, and one frame and one bolster connected by revolute joint. The tank car is another rigid body which holds the fluid body. Twenty assumed modes are used in the numerical study presented in this section to describe the change of the shape of the fluid body. A trajectory coordinate constraint was used to prescribe the forward velocity of the vehicle.

The dynamic interaction between the wheel and the rail is formulated using an elastic contact formulation (Shabana et al., 2008). The wheel/rail contact is described using a compliant force element instead of kinematic constraints, thereby allowing for wheel/rail separations. The rigid rectangular tank is assumed to have dimensions $12\text{m}\times1.52\text{m}\times1.33\text{m}$, and is attached to a massless

plate using rigid joint. The plate is connected to the bolster with several bushing elements.

The liquid used in this chapter is assumed to be water. Numerical experimentation showed that a penalty coefficient of $k = 10000$ N.m leads to acceptable results consistent with water properties, and allows the simulation to be completed in reasonable CPU time. Using this penalty coefficient k, the simulation time for 10s is approximately 4 hours and for 20s is approximately 9 hours. The simulations were performed using HP-Z210 PC with CPU unit of Intel Core i5-2400. Only single processor was used in the simulation (sequential computations). The effect of increasing the damping coefficients is examined in the following section.

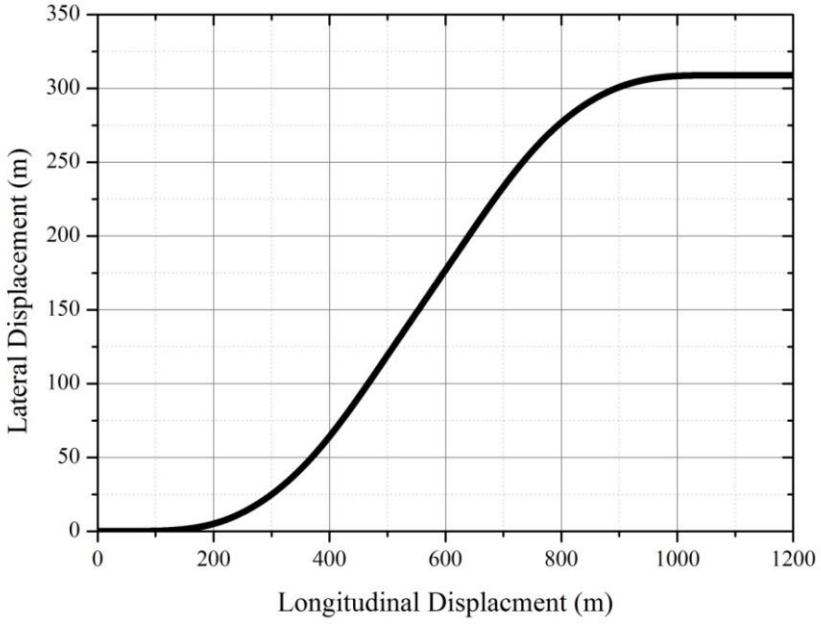

Figure 6. The S-shape curved track

2.4.2 Sloshing Effect

In order to examine the sloshing effect on the motion of the vehicle, another equivalent rigid-body model was used for the purpose of comparison. This rigid body model is obtained by assuming the

fluid body to be rigid while keeping all other model parameters the same. The speed at which the rigid-body model on a tangent track would derail was found to be 90m/s (201 mph), while it is 60m/s (134 mph) for the model which has the fluid body. If the curved track shown in Fig. 6 is used, this speed is 35 m/s (78 mph) for the fluid body model.

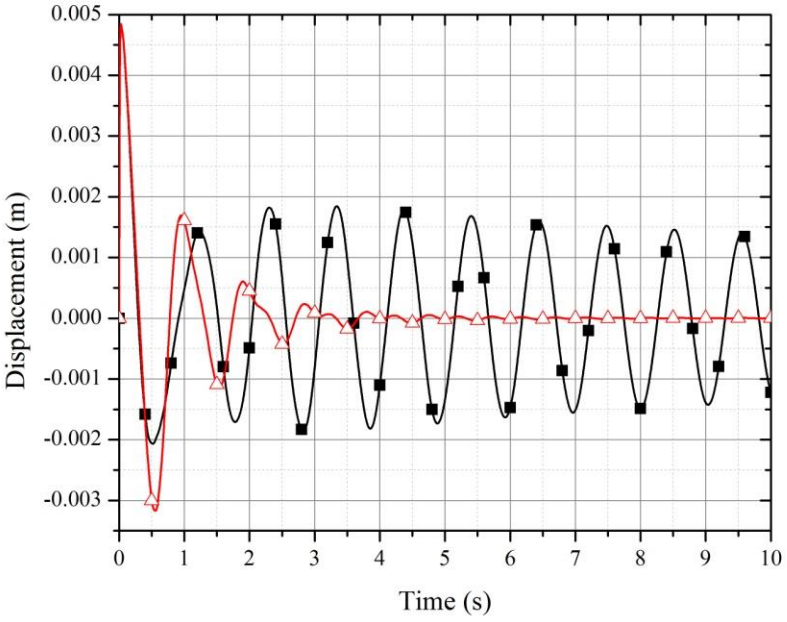

Figure 7. Lateral displacement of the rear wheelset with forward velocity of 25m/s (56mph) (—■—Rigid body , —△— Flexible body)

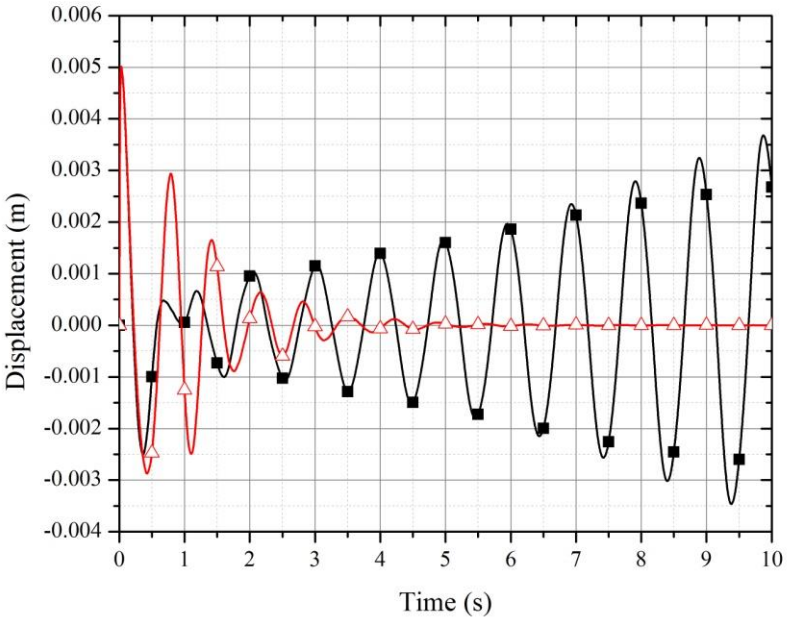

Figure 8. Lateral displacement of the rear wheelset with forward velocity of 35m/s (78mph)
(—■—Rigid body , —△— Flexible body)

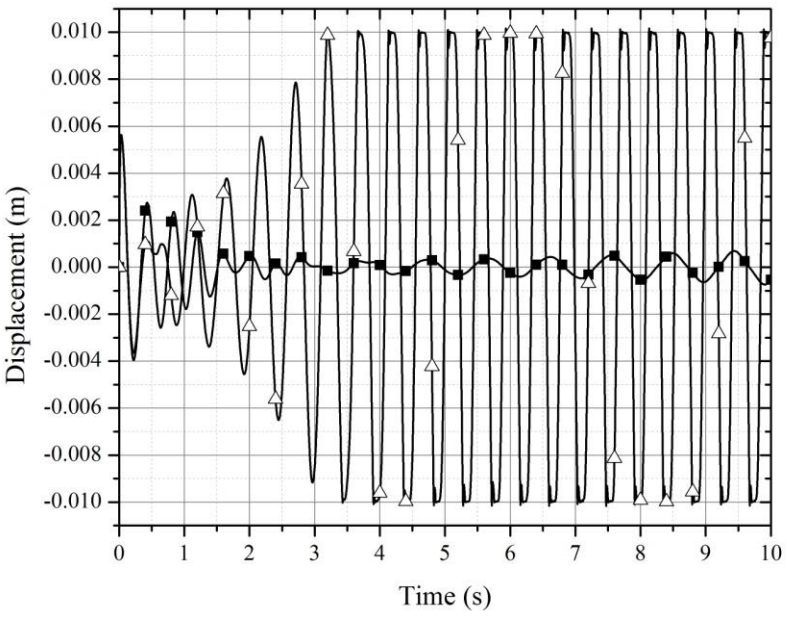

Figure 9. Lateral displacement of the rear wheelset with forward velocity of 60m/s (134mph)
(—■—Rigid body , —△— Flexible body)

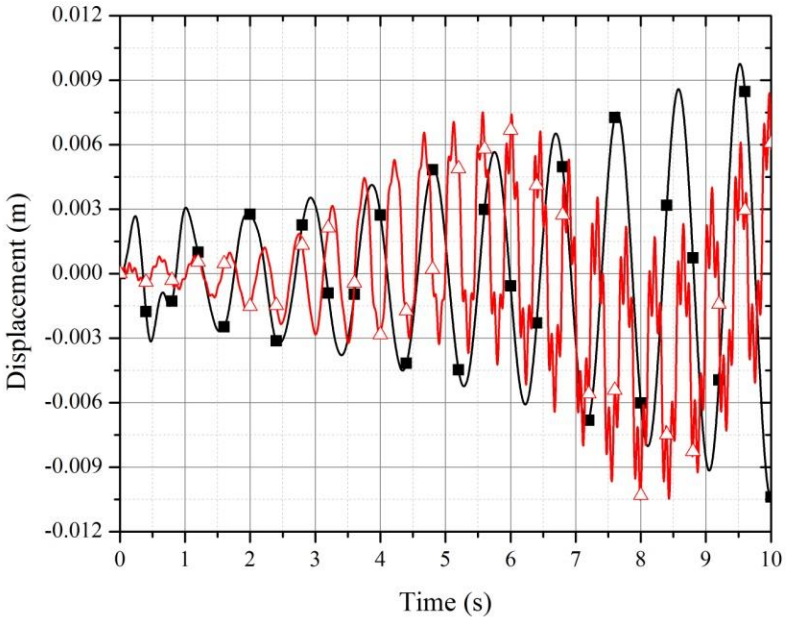

Figure 10. Lateral displacement of the car body with forward velocity of 60m/s (134mph) (—■—Rigid body , —△— Flexible body)

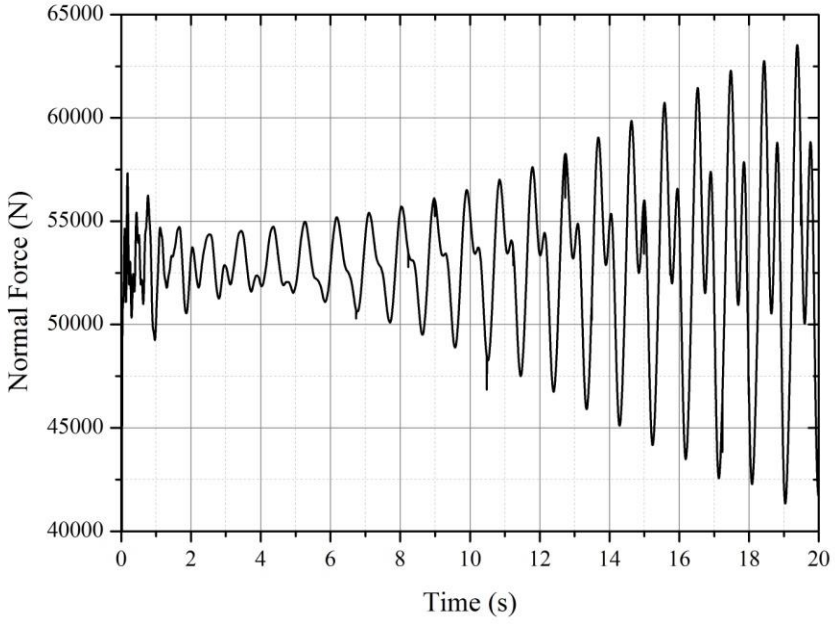

Figure 11. Normal contact force on the right wheel of the rear wheelset of the rear bogie in the rigid body model with forward velocity of 60m/s (134mph)

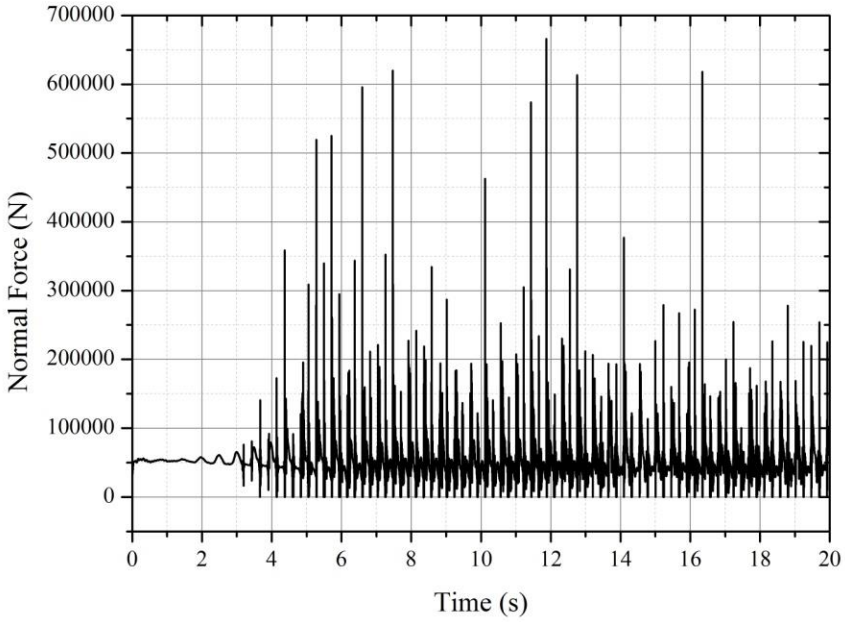

Figure 12. Normal contact force on the right wheel of the rear wheelset of the rear bogie in the fluid body model with forward velocity of 60m/s (134mph)

In the first simulation scenario considered, two constant forward velocities of 25 m/s (56 mph) and 35m/s (78 mph) along the tangent track are considered. All wheelsets are assumed to have 0.5 m/s initial lateral velocity. Figures 7 and 8 show that, at the low speed when hunting is not significant, the fluid body introduces damping that tends to reduce the amplitude of the hunting oscillations, making the system more stable as compared to the rigid body model. However, if the forward velocity is increased to 60 m/s (134 mph), the fluid body model becomes more unstable as compared to the rigid body model, as demonstrated by the results of Fig. 9. Figure 10 shows significant changes in the lateral displacement of center of mass of the fluid body at this relatively high speed. Figures 11 and 12 show the normal force for the rigid and fluid body models, respectively. The results presented in these two figures show that the liquid sloshing can cause

impulsive forces between the wheel and the rail, leading to spikes in the contact force. More importantly, the liquid sloshing can lead to wheel/rail separations which can increase the possibility of rollover and derailment (Fig. 12).

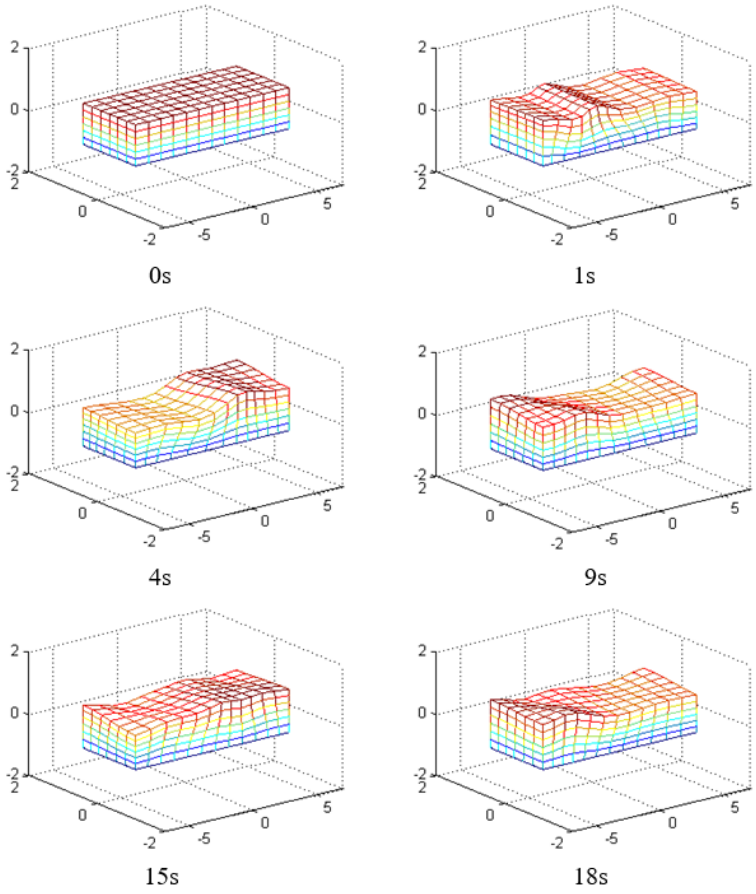

Figure 13. Change of the fluid shape due to sloshing

The second simulation scenario is used to demonstrate that the proposed approach can capture the effect of the three-dimensional fluid body distributed inertia which cannot be captured using the simplified two-dimensional motion pendulum models often used to study liquid sloshing in vehicle dynamics. Figure 13 shows the change in the shape of the liquid due to a sudden forward acceleration accompanied by the hunting motion. It is clear from this figure that the reduced order model proposed in this study can be used to predict the change of the shape of the fluid body.

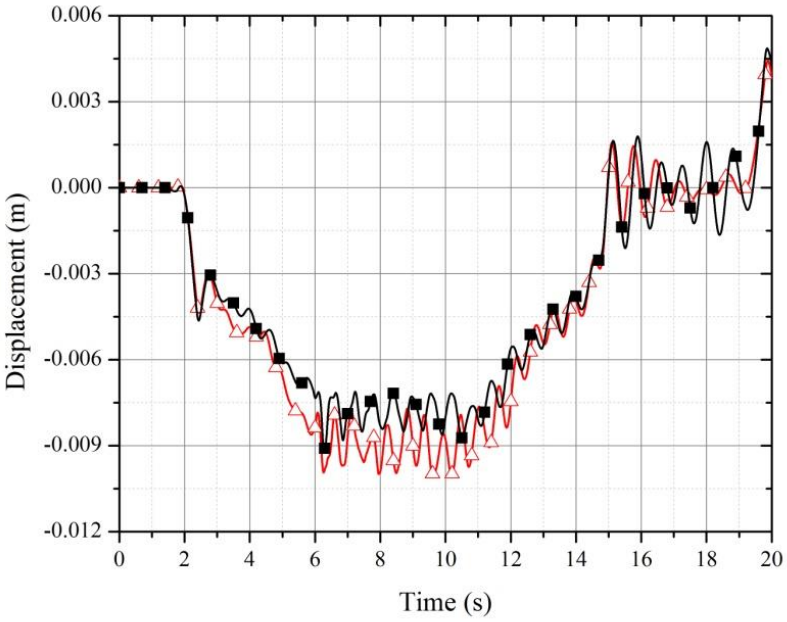

Figure 14. Lateral displacement of the rear wheelset with respect to the track
(—■—Rigid body, —△— Fluid body)

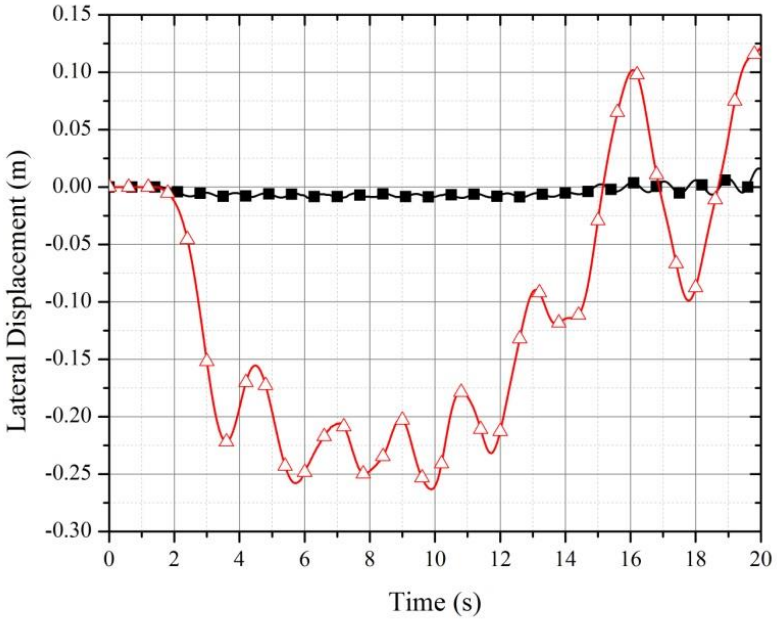

Figure 15. Change of the center of mass with respect to the track
(—■—Rigid body , —△— Fluid body)

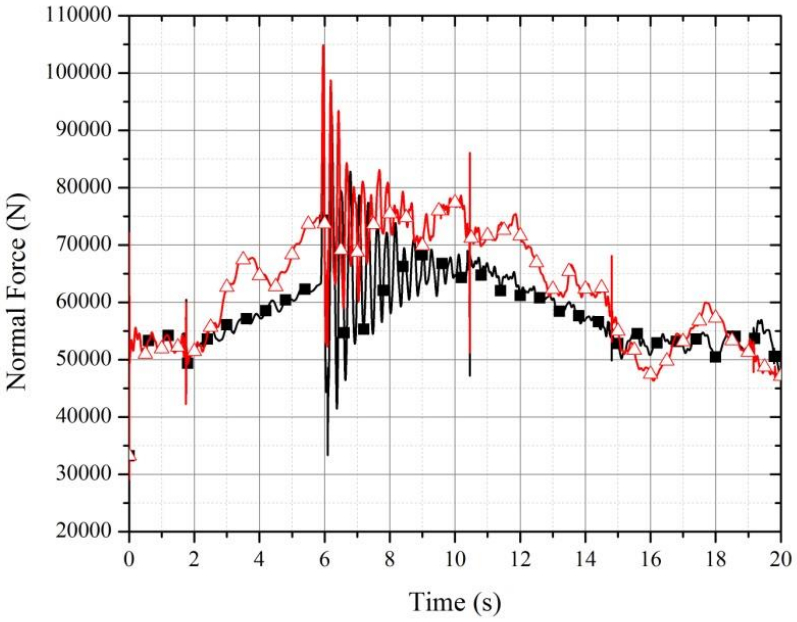

Figure 16. Normal contact force of the right wheel of the rear wheelset of the rear bogie (—■—Rigid body, —△— Fluid body)

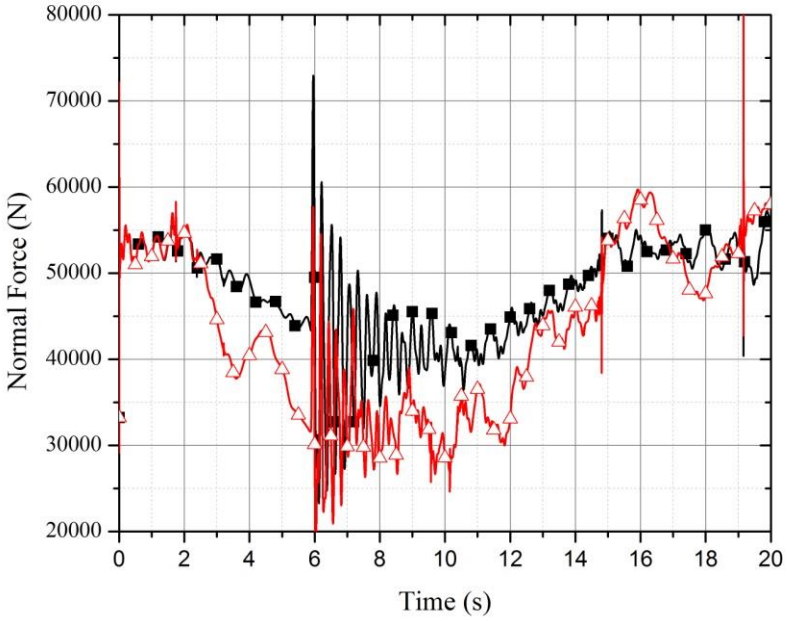

Figure 17. Normal contact force of the left wheel of the rear wheelset of the rear bogie (—■—Rigid body , —△— Flexible body)

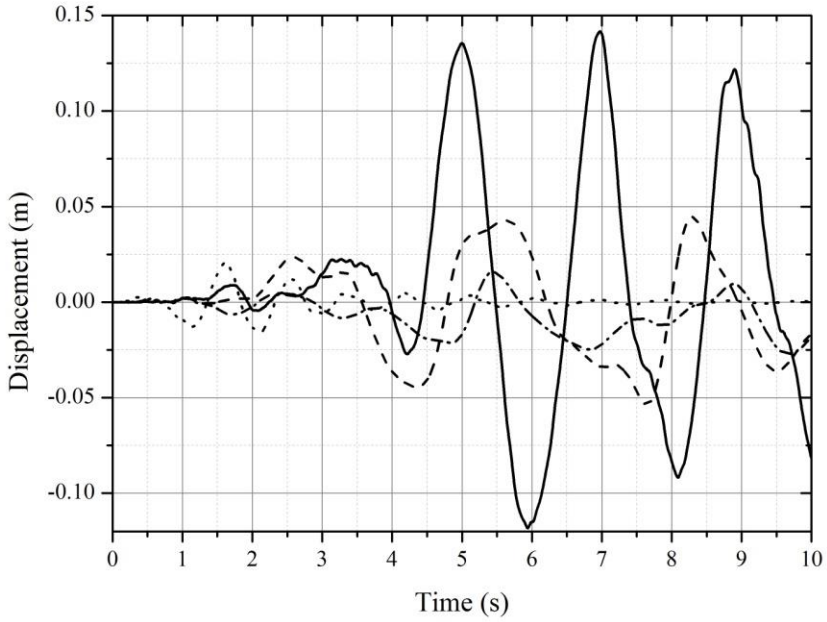

Figure 18. Lateral displacement of the car body using different damping coefficients (——— $c = 0$, - - - - - - $c = 50$, - . - . - . $c = 100$, ... Rigid model)

In a third simulation scenario, the results obtained using the rigid and fluid body models are compared when the vehicle negotiates a curved track at 35 m/s speed with no initial lateral velocity. Figure 14, which depicts the lateral displacement of the wheelset with respect to the track, shows that the fluid body model has larger lateral displacement due to the sloshing effect. Figure 15 shows the change in the location of the center of gravity of the fluid body in the lateral Y direction. The results of this figure show that the change in the position of the center of mass is more significant when the vehicle negotiates a curved track. The results of Figs. 16 and 17 show that changing the location of the fluid body center of mass leads to a different distribution of the normal contact forces on the wheels. That is, the wheels which carry the highest loads in the fluid body and the rigid body models can be different. The results presented in Fig. 18 show that

increasing the viscosity of the fluid leads to a more stable behavior because an increase in the viscosity produces more resistance to the fluid motion.

2.5 Concluding Remarks

In this chapter, a low order three-dimensional liquid sloshing model based on the FFR formulation is proposed. This liquid sloshing model can capture the free surface motion and the distributed inertia of the fluid. Using a total Lagrangian approach and the FFR formulation, the liquid sloshing model was successfully integrated with MBS algorithms and used to study the effect of the sloshing on the dynamics of railroad vehicles. The FE method and modal analysis techniques are used to develop a reduced order fluid body model. The results presented in this chapter shows that liquid sloshing can have a significant effect on the contact forces and the dynamics of the vehicle. This was demonstrated using a three-dimensional wheel/rail contact model that allows for accurate description of the wheel and rail profiles. The results presented in this chapter showed that the wheels that carry the highest loads in the fluid body and rigid body models can be different. The results also show that liquid sloshing tends to increase the possibility of wheel/rail separation.

While the liquid sloshing approach proposed in this study defines a low order model, it has several clear advantages compared to existing models. It is a more realistic model as compared to the discrete inertia models that employ pendulum systems and used in the area of vehicle dynamics, it allows capturing the effect of the fluid body distributed inertia, it allows studying the contribution of each mode of the fluid displacement on the vehicle dynamics and identifying the modes that are the cause of accidents, and it can be systematically integrated into the computational algorithms implemented in most commercial MBS computer programs. As previously mentioned in this chapter, the goal is not to study the effect of the vehicle motion on the fluid, rather the goal is to study the effect of the distributed inertia of the fluid on the vehicle dynamics.

CHAPTER 3

ANCF FLUID MODEL

The objective of this chapter is to develop a total Lagrangian non-incremental liquid sloshing solution procedure based on the finite element (FE) absolute nodal coordinate formulation (ANCF). The proposed liquid sloshing modeling approach can be used to avoid the difficulties of integrating most of fluid dynamics formulations, which are based on the Eulerian approach, with multibody system (MBS) dynamics formulations, which are based on a total Lagrangian approach. The proposed total Lagrangian FE fluid dynamics formulation, which can be systematically integrated with computational MBS algorithms, differs significantly from the conventional FE or finite volume methods which are based on an Eulerian representation that employs the velocity field of a fixed control volume in the region of interest. The ANCF fluid equations are expressed in terms of displacement and gradient coordinates of material points, allowing for straight forward implementation of kinematic constraint equations and for the systematic modeling of the interaction of the fluid with the external environment or with rigid and flexible bodies. The fluid incompressibility conditions and surface traction forces are considered and derived directly from the Navier-Stokes equations. Two ANCF brick elements, one of which is obtained using an incomplete polynomial representation and the other obtained from a B-spline volume representation, are used. The new approach ensures the continuity of the displacement gradients at the nodal points and allows for imposing higher degree of continuity across the element interface by applying algebraic constraint equations that can be used to eliminate dependent variables and reduce the model dimensionality. Regardless of the magnitude of the fluid displacement, the fluid

has a constant mass matrix, leading to zero Coriolis and centrifugal forces. The analysis presented in this chapter demonstrates the feasibility of developing an efficient non-incremental total Lagrangian approach for modeling sloshing problems in MBS system applications in which the bodies can experience large displacements including finite rotations. Several examples are presented in order to shed light on the potential of using the ANCF liquid sloshing formulation developed in this chapter. A two-loop implicit sparse matrix numerical integration (Aboubakr, 2015) which include numerical damping is used in this section.

3.1 Fluid Dynamics Description

The Eulerian and Lagrangian approaches are often used to study the motion of the fluid (Reddy, 2001). In the Eulerian approach, the interest is focused on the fluid motion at specific locations in the space, while in the Lagrangian approach, one traces the motion of the fluid particles. In this section, the basic fluid equations used in this investigation to formulate the liquid sloshing problem are summarized. For simplicity, the case of isotropic, Newtonian, viscous and incompressible fluid will be considered. Other detailed fluid dynamic models can be found in the literature (Anderson, 1995; Reddy et al., 2001). The fluid continuity equation can be written as

$$\frac{\partial \rho(\mathbf{r},t)}{\partial t} + \nabla \cdot (\rho \mathbf{u}) = 0 \tag{22}$$

where ρ is the mass density, t is time, and $\mathbf{r}$ and $\mathbf{u}$ are the position and velocity vectors, respectively. In the case of incompressible fluid, the density is constant, and the continuity equation becomes $\nabla \cdot \mathbf{u} = 0$. The partial differential equation of the fluid can be written as

$$\left(\nabla \boldsymbol{\sigma}^{\mathrm{T}}\right)^{\mathrm{T}} + \mathbf{f}_b - \rho \mathbf{a} = \mathbf{0} \tag{23}$$

where $\mathbf{a}$ is the acceleration vector, $\boldsymbol{\sigma}$ is the symmetric Cauchy stress tensor, and $\mathbf{f}_b$ is the vector of body forces per unit volume. Considering the simple case of isotropic Newtonian fluid, it can be shown that the fluid constitutive equations can be written as $\boldsymbol{\sigma}=\left\{-p\left(\rho,T\right)+\lambda\left(\rho,T\right)\mathrm{tr}\left(\mathbf{D}\right)\right\}\mathbf{I}+2\mu\left(\rho,T\right)\mathbf{D}$, where λ and μ are viscosity coefficients that depend on the fluid mass density ρ and temperature T, p is the hydrostatic pressure defined as $p=\left(1/3\right)\sum_{i=1}^{3}\boldsymbol{\sigma}_{ii}$, $\mathbf{I}$ is a 3×3 identity matrix, "$\mathrm{tr}(\ )$" refers to the trace of a matrix, and $\mathbf{D}$ is the rate of deformation tensor (Spencer, 1980; Shabana, 2012). If the effect of temperature is neglected and the incompressibility assumption is used, the constitutive equations can be simplified and written as

$$\boldsymbol{\sigma}=\left\{p+\lambda\mathrm{tr}\left(\mathbf{D}\right)\right\}\mathbf{I}+2\mu\mathbf{D} \tag{24}$$

Substituting this equation in Eq. 23 leads to

$$\left\{-\nabla\left(p\mathbf{I}\right)+\nabla\left(\lambda\mathrm{tr}\left(\mathbf{D}\right)\mathbf{I}\right)+\nabla\left(2\mu\mathbf{D}\right)\right\}^{\mathrm{T}}+\mathbf{f}_b-\rho\mathbf{a}=\mathbf{0} \tag{25}$$

This is the equilibrium equation which will be used to develop the proposed ANCF fluid finite elements employed in this chapter.

Since the focus of this chapter is on capturing the liquid motion using a computational procedure based on integrating the fluid dynamics with MBS algorithms, a total Lagrangian description will be used. The Green-Lagrangian strain $\boldsymbol{\varepsilon}$ and the second Piola-Kirchhoff stress tensor $\boldsymbol{\sigma}_{P2}$ are used. One can write $\boldsymbol{\sigma}_{P2}=J\mathbf{J}^{-1}\boldsymbol{\sigma}\mathbf{J}^{-1^{\mathrm{T}}}$ and $\mathbf{D}=\mathbf{J}^{-1^{\mathrm{T}}}\dot{\boldsymbol{\varepsilon}}\mathbf{J}^{-1}$, where $\mathbf{J}$ is the matrix of position vector gradients. Using these equations, one can write

$$\boldsymbol{\sigma}_{P2}=-pJ\mathbf{C}_r^{-1}+\lambda J\mathrm{tr}\left(\mathbf{D}\right)\mathbf{C}_r^{-1}+2\mu J\left(\mathbf{C}_r^{-1}\dot{\boldsymbol{\varepsilon}}\mathbf{C}_r^{-1}\right) \tag{26}$$

where $J = |\mathbf{J}|$, and $\mathbf{C}_r = \mathbf{J}^{\mathrm{T}}\mathbf{J}$ is the right Cauchy-Green deformation tensor.

3.2 ANCF Brick Element Kinematics

In this section, the ANCF fluid elements used in this chapter are introduced. Two ANCF brick elements are considered in this section. The first element is based on an incomplete polynomial representation, while the second element has a complete polynomial representation. The assumed displacement field of the two elements, and the continuity conditions at the element interface are discussed. It is shown that the use of the element with incomplete polynomials allows for developing a finer mesh with a significantly smaller number of degrees of freedom. This ANCF brick element allows for applying linear conditions that lead to a higher degree of continuity at the element interface. These conditions can be applied at a preprocessing stage, thereby allowing for eliminating the dependent nodal variables before the start of the dynamic simulation.

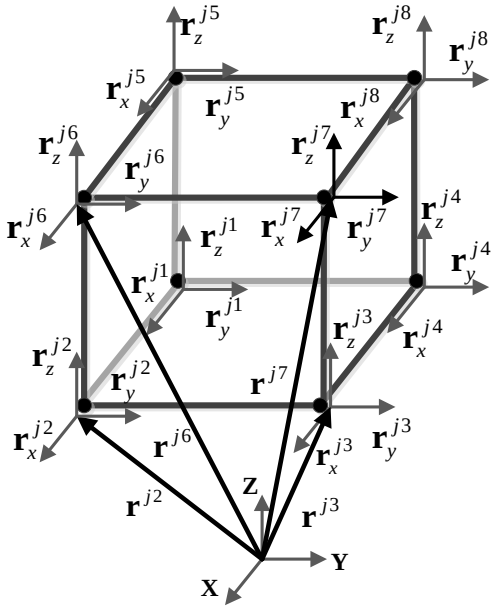

Figure 19. The 8-node brick fluid element

3.2.1 Brick Element with Incomplete Polynomial Representation

The three-dimensional ANCF brick element, with an incomplete polynomial representation, used in this investigation is an 8-node element shown in Fig.19. The nodal coordinates $\mathbf{e}^{jk}$ at the node k of the finite element j can be defined as

$$\mathbf{e}^{jk} = \left[\mathbf{r}^{jk^{\mathrm{T}}} \ \mathbf{r}_x^{jk^{\mathrm{T}}} \ \mathbf{r}_y^{jk^{\mathrm{T}}} \ \mathbf{r}_z^{jk^{\mathrm{T}}} \right]^{\mathrm{T}} \qquad k = 1, 2; ..., 8 \tag{27}$$

where $\mathbf{r}^{jk}$ is the absolute position vector at the node k of the finite element j, and $\mathbf{r}_x^{jk}$, $\mathbf{r}_y^{jk}$ and $\mathbf{r}_z^{jk}$ are the position vector gradients obtained by differentiation with respect to the spatial coordinates x, y and z, respectively. The displacement field of each coordinate of the brick fluid element can be defined using an incomplete polynomial with 32 coefficients as (Olshevskiy, 2013; Wei and Shabana, 2014)

$$\begin{aligned}
\phi(x,y,z) &= \alpha_1 + \alpha_2 x + \alpha_3 y + \alpha_4 z + \alpha_5 x^2 + \alpha_6 y^2 + \alpha_7 z^2 + \alpha_8 xy + \alpha_9 yz + \alpha_{10} xz \\
&+ \alpha_{11} x^3 + \alpha_{12} y^3 + \alpha_{13} z^3 + \alpha_{14} x^2 y + \alpha_{15} x^2 z + \alpha_{16} y^2 z + \alpha_{17} xy^2 + \alpha_{18} xz^2 + \alpha_{19} yz^2 \\
&+ \alpha_{20} xyz + \alpha_{21} x^3 y + \alpha_{22} x^3 z + \alpha_{23} xy^3 + \alpha_{24} y^3 z + \alpha_{25} xz^3 + \alpha_{26} yz^3 + \alpha_{27} x^2 yz \\
&+ \alpha_{28} xy^2 z + \alpha_{29} xyz^2 + \alpha_{30} x^3 yz + \alpha_{31} xy^3 z + \alpha_{32} xyz^3
\end{aligned} \tag{28}$$

In this equation, $\alpha_k, k = 1, 2, ..., 32$, are the polynomial coefficients. Using this polynomial description, the shape functions of the ANCF brick fluid element can be derived as follows:

$$\left.\begin{aligned}
S^{k,1} &= (-1)^{1+\xi_k+\eta_k+\zeta_k} (\xi + \xi_k - 1)(\eta + \eta_k - 1)(\zeta + \zeta_k - 1) \cdot \\
&(1 + (\xi - \xi_k)(1 - 2\xi) + (\eta - \eta_k)(1 - 2\eta) + (\zeta - \zeta_k)(1 - 2\zeta)) \\
S^{k,2} &= (-1)^{\eta_k+\zeta_k} a \xi^{\xi_k+1} (\xi - 1)^{2-\xi_k} \eta^{\eta_k} (\eta - 1)^{1-\eta_k} \zeta^{\zeta_k} (\zeta - 1)^{1-\zeta_k} \\
S^{k,3} &= (-1)^{\xi_k+\zeta_k} b \xi^{\xi_k} (\xi - 1)^{1-\xi_k} \eta^{\eta_k+1} (\eta - 1)^{2-\eta_k} \zeta^{\zeta_k} (\zeta - 1)^{1-\zeta_k} \\
S^{k,4} &= (-1)^{\xi_k+\eta_k} c \xi^{\xi_k} (\xi - 1)^{1-\xi_k} \eta^{\eta_k} (\eta - 1)^{1-\eta_k} \zeta^{\zeta_k+1} (\zeta - 1)^{2-\zeta_k}
\end{aligned}\right\} \quad k = 1, 2..., 8 \tag{29}$$

where a,b, and c are, respectively, the dimensions of the element along the axes x, y, and z directions, $\xi = x/a,\ \eta = y/b,\ \zeta = z/c$, $\xi,\ \eta,\ \zeta \in [0,1]$, and ξ_k, η_k, ζ_k are the dimensionless nodal locations for node k. The position vector of an arbitrary material point on element j can be written as

$$\mathbf{r}^j = \sum_{k=1}^{8} \begin{bmatrix} S^{k,1}\mathbf{I} & S^{k,2}\mathbf{I} & S^{k,3}\mathbf{I} & S^{k,4}\mathbf{I} \end{bmatrix} \mathbf{e}^{jk} = \mathbf{S}^j \mathbf{e}^j \tag{30}$$

Where $\mathbf{I}$ is the 3×3 identity matrix, $\mathbf{S}^j$ and $\mathbf{e}^j$ are, respectively, the element shape function matrix and the vector of nodal coordinates which can be written as

$$\left.\begin{aligned} \mathbf{S}^j &= \begin{bmatrix} S^{1,1}\mathbf{I} & S^{1,2}\mathbf{I} & S^{1,3}\mathbf{I} & S^{1,4}\mathbf{I} & \ldots S^{8,1}\mathbf{I} & S^{8,2}\mathbf{I} & S^{8,3}\mathbf{I} & S^{8,4}\mathbf{I} \end{bmatrix} \\ \mathbf{e}^j &= \begin{bmatrix} \mathbf{e}^{j1^{\mathrm{T}}} & \mathbf{e}^{j2^{\mathrm{T}}} & \mathbf{e}^{j3^{\mathrm{T}}} & \mathbf{e}^{j4^{\mathrm{T}}} & \mathbf{e}^{j5^{\mathrm{T}}} & \mathbf{e}^{j6^{\mathrm{T}}} & \mathbf{e}^{j7^{\mathrm{T}}} & \mathbf{e}^{j8^{\mathrm{T}}} \end{bmatrix}^{\mathrm{T}} \end{aligned}\right\} \tag{31}$$

Because the proposed element has 96 degrees of freedom (DOFs), by using one element, complex fluid shapes can be captured as demonstrated in the numerical example section.

3.2.2 ANCF Element with Complete Polynomial Representation

The configuration of this element is the same as the one with the incomplete polynomial ANCF element shown in Fig. 19. The element has 8 nodes, but the number of nodal coordinates at each node is 24 instead of 12. These nodal coordinates are defined as follows:

$$\mathbf{e}^{jk} = \begin{bmatrix} \mathbf{r}^{jk^{\mathrm{T}}} & \mathbf{r}_x^{jk^{\mathrm{T}}} & \mathbf{r}_y^{jk^{\mathrm{T}}} & \mathbf{r}_z^{jk^{\mathrm{T}}} & \mathbf{r}_{xy}^{jk^{\mathrm{T}}} & \mathbf{r}_{yz}^{jk^{\mathrm{T}}} & \mathbf{r}_{xz}^{jk^{\mathrm{T}}} & \mathbf{r}_{xyz}^{jk^{\mathrm{T}}} \end{bmatrix}^{\mathrm{T}} \qquad k = 1,2\ldots,8 \tag{32}$$

The element discussed in this section is obtained from a B-spline volume representation that has the following Bernstein functions in the three directions $\xi,\ \eta$, and ζ:

$$\left.\begin{aligned} S_{\xi,0} &= 2\xi^3 - 3\xi^2 + 1,\ S_{\xi,1} = a\left(\xi^3 - 2\xi^2 + \xi\right),\ S_{\xi,2} = -2\xi^3 + 3\xi^2,\ S_{\xi,3} = a\left(\xi^3 - \xi^2\right) \\ S_{\eta,0} &= 2\eta^3 - 3\eta^2 + 1,\ S_{\eta,1} = b\left(\eta^3 - 2\eta^2 + \eta\right),\ S_{\eta,2} = -2\eta^3 + 3\eta^2,\ S_{\eta,3} = b\left(\eta^3 - \eta^2\right) \\ S_{\zeta,0} &= 2\zeta^3 - 3\zeta^2 + 1,\ S_{\zeta,1} = c\left(\zeta^3 - 2\zeta^2 + \zeta\right),\ S_{\zeta,2} = -2\zeta^3 + 3\zeta^2,\ S_{\zeta,3} = c\left(\zeta^3 - \zeta^2\right) \end{aligned}\right\} \quad (33)$$

Using these B-spline basis functions, the 64 shape functions of the ANCF brick element with complete polynomial representation can be written as follows:

$$\left.\begin{aligned} S^{k,1} &= S_{\xi,2\xi_k} S_{\eta,2\eta_k} S_{\zeta,2\zeta_k},\ S^{k,2} = S_{\xi,2\xi_k+1} S_{\eta,2\eta_k} S_{\zeta,2\zeta_k} \\ S^{k,3} &= S_{\xi,2\xi_k} S_{\eta,2\eta_k+1} S_{\zeta,2\zeta_k},\ S^{k,4} = S_{\xi,2\xi_k} S_{\eta,2\eta_k} S_{\zeta,2\zeta_k+1} \\ S^{k,5} &= S_{\xi,2\xi_k+1} S_{\eta,2\eta_k+1} S_{\zeta,2\zeta_k},\ S^{k,6} = S_{\xi,2\xi_k} S_{\eta,2\eta_k+1} S_{\zeta,2\zeta_k+1} \\ S^{k,7} &= S_{\xi,2\xi_k+1} S_{\eta,2\eta_k} S_{\zeta,2\zeta_k+1},\ S^{k,8} = S_{\xi,2\xi_k+1} S_{\eta,2\eta_k+1} S_{\zeta,2\zeta_k+1} \end{aligned}\right\} (k = 1,...,8) \quad (34)$$

These shape functions can be used to define the element displacement field in the manner described by Eqs. 30 and 31.

3.2.3 Continuity Conditions

In this chapter, the incomplete polynomial ANCF element will be referred to as IPAE, while the B-spline/ANCF element will be referred to as BSAE. The first element ensures the continuity of the displacement gradients at the nodes, while the second element ensures the continuity of the gradients as well as the curvature vectors which appear in Eq. 32. Nonetheless, IPAE linear algebraic equations can be developed and applied at a preprocessing stage in order to increase the degree of continuity of the IPAE mesh. This procedure allows for developing initially a finer IPAE mesh. One can then not only reduce the mesh dimensionality by applying constraint equations to obtain the desired continuity required in the fluid simulations and but at the same time significantly reduce the model dimension as well.

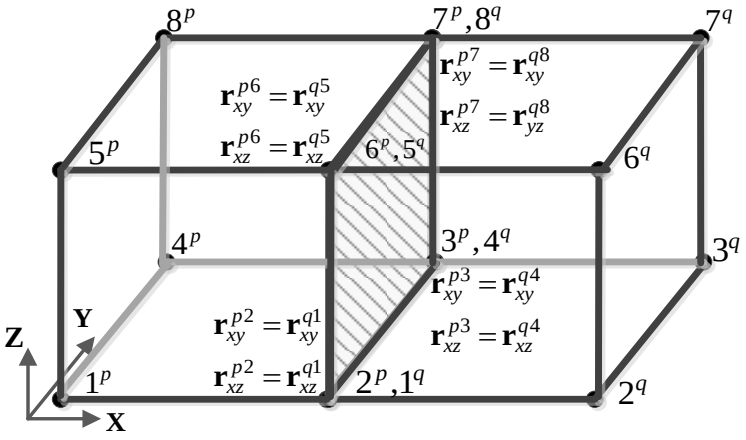

Figure 20. Continuity at the element interface

Figure 20 shows the continuity conditions at the element interface using a two-element mesh, the numbers indicate the node numbers of the individual elements, while the letter superscripts p and q denote the element number. For the IPAE mesh, the C^0, C_y^1 and C_z^1 continuities at the element interface are automatically ensured using standard FE element assembly procedure, where subscripts x, y, and z will be used in this chapter to refer to the coordinate along which the continuity conditions apply. As shown in Fig. 21, the C_x^1 continuity is not ensured for the IPAE mesh, while Fig. 22 shows that the C_x^1 continuity is ensured for the BSAE mesh. The coordinate systems used in Figs. 21 and 22 are the same as the coordinate system used in Fig. 20. In Fig. 21a, one can notice the discontinuity along the x coordinate at the boundary of two adjacent elements, and Fig. 21b shows this discontinuity in the direction of the gradient vectors. One, however, can increase the IPAE degree of continuity at the element interface by imposing linear algebraic equations at a preprocessing stage. For example, using the algebraic equations $\mathbf{S}_x\left(\xi = 1, \eta, \varsigma\right)\mathbf{e}^p = \mathbf{S}_x\left(\xi = 0, \eta, \varsigma\right)\mathbf{e}^q$ ensures the continuity of the IPAE gradient vector along the x coordinate at the element interface. Nonetheless, these eight algebraic equations are not

sufficient to ensure the IPAE $\mathbf{r}_x$ continuity at the element interface which is ensured automatically by using the BSAE mesh. In order to achieve $\mathbf{r}_x$ continuity at the element interface in addition to the continuity of this gradient vector at the nodal points when the IPAE mesh is used, one must also ensure the continuity of the IPAE $\mathbf{r}_{xy}$ and $\mathbf{r}_{xz}$ curvature vectors at the nodal points of the IPAE mesh. Therefore, the continuity of the $\mathbf{r}_x$ gradient vector at the element interface for the two-element IPAE mesh requires the formulation of 24 linear algebraic equations that can be used to reduce the model dimensionality at a preprocessing stage. This process, which can be automated and advantageous in many applications since it can significantly reduce the model dimension, will also reduce the number of displacement modes that can be assumed by the fluid. In many applications, however, the remaining modes are sufficient for obtaining an accurate solution, and therefore the use of the IPAE mesh can be advantageous computationally. For example, to ensure C^1 continuity at the element interface of an eight-IPAE mesh which has 27 nodes and 324 coordinates as shown in Fig. 23, one has to ensure C^1 continuity in all directions at the element interface. After eliminating redundant constraints, the number of degrees of freedom of the mesh is reduced to 168. Compared with the two-BSAE mesh which has 288 coordinates and automatically ensures C_x^1 by using the standard FE assembly without the need for imposing constraint equations, it is clear that the eight-IPAE mesh which ensures the continuity of the $\mathbf{r}_x$ gradient vector at the element interface has fewer degrees of freedom, and therefore, is more computationally efficient than the BSAE mesh.

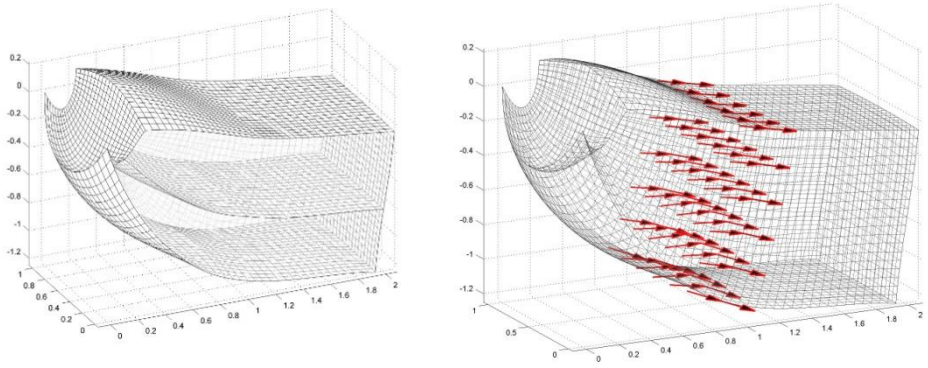

(a) (b)

Figure 21. C^1 Interface discontinuity in two-IPAE mesh

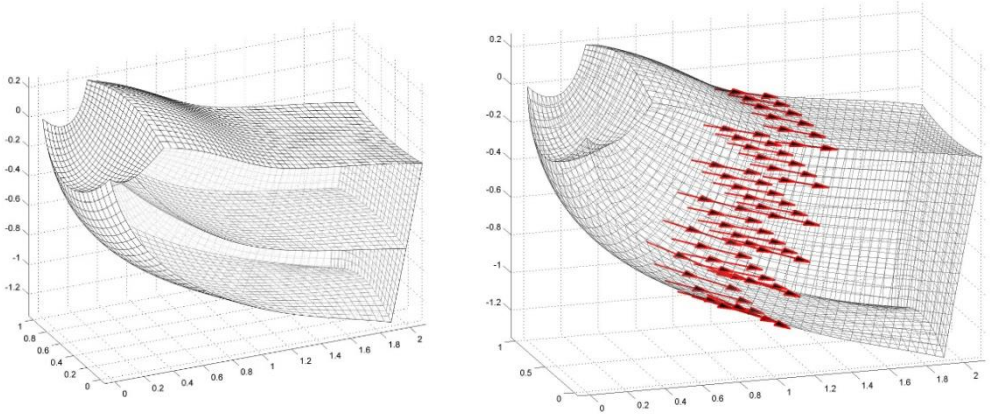

(a) (b)

Figure 22. C^1 Continuity after applying continuity constraints

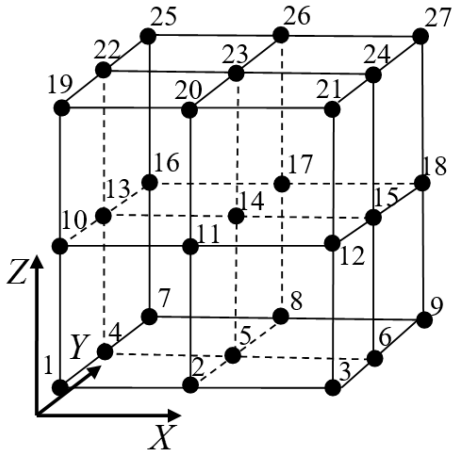

Figure 23. Eight-IPAE mesh

3.3 ANCF Fluid Dynamics Model

The fluid Navier-Stokes equations, the viscous forces, the incompressibility condition, and the surface tension of the ANCF fluid elements are introduced in this section.

3.3.1 Navier-Stokes Generalized Stress Forces

As previously discussed in this chapter, the fluid constitutive equations can be written as $\boldsymbol{\sigma} = \left\{ p + \lambda \mathrm{tr}\left(\mathbf{D}\right) \right\} \mathbf{I} + 2\mu \mathbf{D}$. In this fluid equation, μ is the *coefficient of shear viscosity*, and $\left(\lambda + \left(2\mu/3\right)\right)$ is called the *coefficient of bulk viscosity*. If $\lambda + \left(2\mu/3\right) = 0$, one has the *Stokes' relation*. For *incompressible fluids* element j, the determinant of the matrix of position vector gradients $\mathbf{J}^j$ must be equal to one, that is $J^j = 1$, and since $\mathrm{tr}\left(\mathbf{D}^j\right) = \dot{J}^j / J^j$, it follows that $\mathrm{tr}\left(\mathbf{D}^j\right) = 0$. Consequently, imposing the incompressibility condition at the velocity level $\dot{J}^j = 0$ ensures that $\mathrm{tr}\left(\mathbf{D}^j\right) = 0$. In this special case, the mass density ρ remains constant, and the fluid constitutive equation reduces to $\boldsymbol{\sigma}^j = -p^j \mathbf{I} + 2\mu \mathbf{D}^j$. One can also show that in the case of incompressible fluid, by enforcing the condition $J^j = 1$, the Navier-Stokes stress relationship reduces to $\boldsymbol{\sigma}^j = 2\mu \mathbf{D}^j$ (Spencer, 1980; Wang et al., 2014).

In general, the virtual work of the fluid stress forces can be written as

$$\delta W_s^j = -\int_{v^j} \boldsymbol{\sigma}^j : \delta \mathbf{J}^j \mathbf{J}^{j^{-1}} dv^j = -\int_{V^j} \boldsymbol{\sigma}_{P2}^j : \delta \boldsymbol{\varepsilon}^j dV^j \tag{35}$$

In this equation, v^j is the volume in the current configuration, V^j is the volume defined in the reference configuration, and $\boldsymbol{\sigma}_{P2}^j = J^j \left(\left(\mathbf{J}^j \right)^{-1} \boldsymbol{\sigma}^j \left(\mathbf{J}^j \right)^{-1^{\mathrm{T}}} \right)$ is the second Piola-Kirchhoff stress tensor. One can also write the virtual work of the stress forces as $\delta W_s^j = -\int_{V^j} J^j \boldsymbol{\sigma}^j : \delta \mathbf{J}^j \left(\mathbf{J}^j \right)^{-1} dV^j$

in order to allow performing the integration over the volume in the reference configuration. The virtual change in the strain tensor can be written as $\delta\boldsymbol{\varepsilon}^j = \left(\partial\boldsymbol{\varepsilon}^j/\partial\mathbf{e}^j\right)\delta\mathbf{e}^j$, in which $\partial\boldsymbol{\varepsilon}^j/\partial\mathbf{e}^j$ can be written using vector notations as:

$$\left(\frac{\partial\boldsymbol{\varepsilon}^j}{\partial\mathbf{e}^j}\right)_{vector} = \left[\mathbf{S}_x^{j^{\mathrm{T}}}\mathbf{S}_x^j\mathbf{e}^j \quad \mathbf{S}_y^{j^{\mathrm{T}}}\mathbf{S}_y^j\mathbf{e}^j \quad \mathbf{S}_z^{j^{\mathrm{T}}}\mathbf{S}_z^j\mathbf{e}^j \quad 2\mathbf{S}_x^{j^{\mathrm{T}}}\mathbf{S}_y^j\mathbf{e}^j \quad 2\mathbf{S}_y^{j^{\mathrm{T}}}\mathbf{S}_z^j\mathbf{e}^j \quad 2\mathbf{S}_z^{j^{\mathrm{T}}}\mathbf{S}_x^j\mathbf{e}^j\right]^{\mathrm{T}} \tag{36}$$

The fluid viscous forces can then be written as follows:

$$\delta W_v^j = -\int_{V^j}\left(J^j\left(\left(\mathbf{J}^j\right)^{-1}2\mu\mathbf{D}^j\left(\mathbf{J}^j\right)^{-1^{\mathrm{T}}}\right)\right):\delta\boldsymbol{\varepsilon}^j dV^j = -\int_{V^j}2\mu J^j\left(\mathbf{C}_r^{j^{-1}}\dot{\boldsymbol{\varepsilon}}^j\mathbf{C}_r^{j^{-1}}\right):\delta\boldsymbol{\varepsilon}^j dV^j = \mathbf{Q}_v^j\delta\mathbf{e}^j \tag{37}$$

where $\left(\dot{\boldsymbol{\varepsilon}}^j\right)_{vector} = \left[\mathbf{e}^{j^{\mathrm{T}}}\mathbf{S}_x^{j^{\mathrm{T}}}\mathbf{S}_x^j\dot{\mathbf{e}}^j \quad \mathbf{e}^{j^{\mathrm{T}}}\mathbf{S}_y^{j^{\mathrm{T}}}\mathbf{S}_y^j\dot{\mathbf{e}}^j \quad \mathbf{e}^{j^{\mathrm{T}}}\mathbf{S}_z^{j^{\mathrm{T}}}\mathbf{S}_z^j\dot{\mathbf{e}}^j \quad 2\mathbf{e}^{j^{\mathrm{T}}}\mathbf{S}_x^{j^{\mathrm{T}}}\mathbf{S}_y^j\dot{\mathbf{e}}^j \quad 2\mathbf{e}^{j^{\mathrm{T}}}\mathbf{S}_y^{j^{\mathrm{T}}}\mathbf{S}_z^j\dot{\mathbf{e}}^j \quad 2\mathbf{e}^{j^{\mathrm{T}}}\mathbf{S}_z^{j^{\mathrm{T}}}\mathbf{S}_x^j\dot{\mathbf{e}}^j\right]^{\mathrm{T}}$, is the vector form of the time rate of strain. Using the preceding equation, one can show that the generalized viscous force vector can be written as

$$\mathbf{Q}_v^j = -\int_{V^j}2\mu J^j\left(\mathbf{C}_r^{j^{-1}}\dot{\boldsymbol{\varepsilon}}^j\mathbf{C}_r^{j^{-1}}\right):\frac{\partial\boldsymbol{\varepsilon}^j}{\partial\mathbf{e}^j}dV \tag{38}$$

This vector of generalized forces associated with the ANCF nodal coordinates will be used to define the equations of motion of the fluid.

3.3.2 Incompressibility Condition

The conservation of mass implies $dm = \rho_0 dV = \rho dv$, where ρ_0 and dV are, respectively, the density and the volume of the undeformed element, while ρ and dv are, respectively, the density and the volume in the current configuration. The relationship between the volumes in the undeformed reference and current configurations is (Spencer, 1980; Shabana, 2012)

$$dv = \mathbf{r}_x dx\cdot\left(\mathbf{r}_y dy\times\mathbf{r}_z dz\right) = \left(\mathbf{r}_x\cdot\left(\mathbf{r}_y\times\mathbf{r}_z\right)\right)dxdydz = JdV \tag{39}$$

where $J = |\mathbf{J}| = |\mathbf{r}_x \ \mathbf{r}_y \ \mathbf{r}_z|$. It follows that $\rho_0 = \rho J$. In the case of incompressible materials, as previously mentioned, $J = |\mathbf{J}| = 1$. In the numerical implementation, the penalty method is used to enforce the incompressibility condition. In order to enforce the condition $J^j = |\mathbf{J}^j| = 1$ for the element j, the penalty strain energy $U_{IC}^j = (1/2) k_{IC}^j \left(J^j - 1\right)^2$ is used, where k_{IC}^j is a penalty coefficient. One can obtain the penalty force $\mathbf{Q}_{IC}^j$ by differentiating the energy with respect to the nodal coordinates of element j as $\mathbf{Q}_{IC}^{j^{\mathrm{T}}} = \partial U_{IC}^j / \partial \mathbf{e}^j = k_{IC}^j \left(J^j - 1\right)\left(\partial J^j / \partial \mathbf{e}^j\right)$. Keeping in mind that $J^j = |\mathbf{J}^j| = |\mathbf{r}_x^j \ \mathbf{r}_y^j \ \mathbf{r}_z^j|$, one has

$$\left(\frac{\partial J^j}{\partial \mathbf{e}^j}\right)^{\mathrm{T}} = \mathbf{S}_x^{j^{\mathrm{T}}} \left(\mathbf{r}_y^j \times \mathbf{r}_z^j\right) + \mathbf{S}_y^{j^{\mathrm{T}}} \left(\mathbf{r}_z^j \times \mathbf{r}_x^j\right) + \mathbf{S}_z^{j^{\mathrm{T}}} \left(\mathbf{r}_x^j \times \mathbf{r}_y^j\right) \tag{40}$$

where $\mathbf{S}_x^j, \mathbf{S}_y^j$, and $\mathbf{S}_z^j$ are, respectively, the derivatives of the shape function matrix with respect to x, y and z spatial coordinates of element j. It follows that the penalty force vector of the incompressible fluid element can be written using the ANCF element shape functions as

$$\mathbf{Q}_{IC}^{j^{\mathrm{T}}} = k_{IC}^j \left(J^j - 1\right)\left(\mathbf{S}_x^{j^{\mathrm{T}}} \left(\mathbf{r}_y^j \times \mathbf{r}_z^j\right) + \mathbf{S}_y^{j^{\mathrm{T}}} \left(\mathbf{r}_z^j \times \mathbf{r}_x^j\right) + \mathbf{S}_z^{j^{\mathrm{T}}} \left(\mathbf{r}_x^j \times \mathbf{r}_y^j\right)\right) \tag{41}$$

One can also impose the incompressibility condition at the velocity level by formulating the dissipation function $U_{TD}^j = (1/2) c_{TD}^j \left(\dot{J}^j\right)^2$ resulting from the condition $\dot{J}^j = 0$, where c_{TD}^j is another penalty coefficient. Following the same procedure one can write $\mathbf{Q}_{TD}^{j^{\mathrm{T}}} = \partial U_{TD}^j / \partial \dot{\mathbf{e}}^j = c_{TD}^j \dot{J}^j \left(\partial \dot{J}^j / \partial \dot{\mathbf{e}}^j\right)$, where $\dot{J}^j = \mathrm{tr}\left(\mathbf{D}^j\right) J^j$ and $\partial \dot{J}^j / \partial \dot{\mathbf{e}}^j = \partial J^j / \partial \mathbf{e}^j$. It follows that the penalty force due to enforcing the condition $\dot{J}^j = 0$ can be written as

$$\mathbf{Q}_{TD}^{j^{\mathrm{T}}} = c_{TD}^j J^j \mathrm{tr}\left(\mathbf{D}^j\right)\left(\mathbf{S}_x^{j^{\mathrm{T}}} \left(\mathbf{r}_y^j \times \mathbf{r}_z^j\right) + \mathbf{S}_y^{j^{\mathrm{T}}} \left(\mathbf{r}_z^j \times \mathbf{r}_x^j\right) + \mathbf{S}_z^{j^{\mathrm{T}}} \left(\mathbf{r}_x^j \times \mathbf{r}_y^j\right)\right) \tag{42}$$

The incompressibility condition at velocity level can also be written using Eq. 26 and the virtual work. The second term of Eq. 26 is $\boldsymbol{\sigma}_{Jv} = \lambda J \,\mathrm{tr}\left(\mathbf{D}\right)\mathbf{C}_r^{-1}$ which is used in the following virtual work expression:

$$\delta W_{Jv}^{j} = -\int_{V^j} \left(\lambda^j J^j \mathrm{tr}\left(\mathbf{D}^j\right)\mathbf{C}_r^{j^{-1}}\right) : \delta\boldsymbol{\varepsilon}^j dV^j = \mathbf{Q}_{Jv}^{j}\delta\mathbf{e}^j \tag{43}$$

where λ^j is the viscosity coefficient which can be written as $\lambda^j = k^j - \frac{2}{3}\mu^j$, where k^j is the bulk modulus of the fluid element. The vectors $\mathbf{Q}_{Jv}^{j}$ and $\mathbf{Q}_{TD}^{j}$ have the same effect in imposing the incompressibility condition at the velocity level.

3.3.3 Surface Traction Forces

The partial differential equation of the fluid was previously defined in this chapter as $\left(\nabla\boldsymbol{\sigma}^{\mathrm{T}}\right)^{\mathrm{T}} + \mathbf{f}_b - \rho\mathbf{a} = \mathbf{0}$. Multiplying this equation by $\delta\mathbf{r}$ and integrating over the current volume, one obtains $\int_v \left\{\left(\nabla\boldsymbol{\sigma}^{\mathrm{T}}\right) + \mathbf{f}_b - \rho\mathbf{a}\right\}^{\mathrm{T}} \delta\mathbf{r} dv = 0$. Using Gauss theorem, one can write

$$\int_s \mathbf{n}^{\mathrm{T}}\boldsymbol{\sigma}\delta\mathbf{r} ds - \int_v \boldsymbol{\sigma} : \left(\delta\mathbf{J}\right)\mathbf{J}^{-1} dv + \int_v \mathbf{f}_b^{\mathrm{T}}\delta\mathbf{r} dv - \int_v \left(\rho\mathbf{a}\right)^{\mathrm{T}}\delta\mathbf{r} dv = 0 \tag{44}$$

where the first integral in this equation represents the virtual work of the surface traction forces, the second integral is the virtual work of the internal elastic forces which are described in the previous sections and the third and fourth terms are the virtual work of the body and inertia forces, respectively (Spencer, 1980; Shabana, 2012). The virtual work of the surface traction forces for element j is $\delta W_t^j = \int_{s^j} \mathbf{n}^{j^{\mathrm{T}}}\boldsymbol{\sigma}^j\delta\mathbf{r}^j ds^j$, where $\mathbf{n}^j$ is the unit normal to the surface, and s^j is the current area. By relating the area in the current and reference configurations using Nanson's

formula (Ogden, 1984; Shabana, 2012), one has $J^j\mathbf{N}^j dS^j = \mathbf{J}^{j^{\mathrm{T}}}\mathbf{n}^j ds^j$ which shows that $\mathbf{n}^{j^{\mathrm{T}}} = \left(\mathbf{N}^{j^{\mathrm{T}}}\mathbf{J}^{j^{-1}}J^j\right)dS^j/ds^j$, where S^j and $\mathbf{N}^j$ are, respectively, the area and normal to the surface in the reference configuration. It follows that the virtual work of the surface traction forces can be written as

$$\delta W_t^j = \int_{s^j} \mathbf{n}^{j^{\mathrm{T}}}\boldsymbol{\sigma}^j\delta\mathbf{r}^j ds^j = \int_s \left(\mathbf{N}^{j^{\mathrm{T}}}\mathbf{J}^{j^{-1}}J^j\right)\frac{dS^j}{ds^j}\boldsymbol{\sigma}^j\delta\mathbf{r}^j ds^j = \int_{S^j} J^j\mathbf{N}^{j^{\mathrm{T}}}\mathbf{J}^{j^{-1}}\boldsymbol{\sigma}^j\delta\mathbf{r}^j dS^j \qquad (45)$$

where $\delta\mathbf{r}^j = \mathbf{S}^j\delta\mathbf{e}^j$. One can then write $\delta W_t^j = \int_{S^j} J^j\mathbf{N}^{j^{\mathrm{T}}}\mathbf{J}^{j^{-1}}\boldsymbol{\sigma}^j\mathbf{S}^j\delta\mathbf{e}^j dS^j = \mathbf{Q}_t^j\delta\mathbf{e}^j$. In this case, the surface traction force can be defined as follows:

$$\mathbf{Q}_t^j = \int_{S^j} J^j\mathbf{N}^{j^{\mathrm{T}}}\mathbf{J}^{j^{-1}}\boldsymbol{\sigma}^j\mathbf{S}^j dS^j = \int_{S^j}\mathbf{N}^{j^{\mathrm{T}}}\boldsymbol{\sigma}_{P1}^j\mathbf{S}^j dS^j \qquad (46)$$

where $\boldsymbol{\sigma}_{P1}^j = J^j\mathbf{J}^{j^{-1}}\boldsymbol{\sigma}^j$ is the first Piola-Kirchhoff stress tensor, and $\mathbf{S}^j$ is the shape function matrix of the ANCF brick element.

3.3.4 Equations of Motion

Because of the conservation of mass, $\rho dv = \rho_o dV$, the virtual work of the inertia forces for element j in the reference configuration as $\delta U_I^j = \int_{V^j}\rho^j\mathbf{a}^j\cdot\delta\mathbf{r}^j\, dV^j = \left(\mathbf{M}^j\ddot{\mathbf{e}}^j\right)\cdot\delta\mathbf{e}^j$, where $\mathbf{M}^j = \int_{V^j}\rho^j\mathbf{S}^{j^T}\mathbf{S}^j dV^j$ is the constant symmetric mass matrix of the fluid element j. This matrix is constant regardless of the magnitude of the fluid displacement. The virtual work of the body forces can also be obtained as $\delta U_b^j = \int_{V^j}\mathbf{f}_b^{j^{\mathrm{T}}}\delta\mathbf{r}^j\, dV^j = \int_{V^j}\mathbf{f}_b^{j^{\mathrm{T}}}\mathbf{S}^j\,\delta\mathbf{e}^j dV^j = \mathbf{Q}_b^j\delta\mathbf{e}^j$. Using the virtual work of the inertia and other forces, one obtains the following element equations of motion:

$$\mathbf{M}^j\ddot{\mathbf{e}}^j = \mathbf{Q}_b^j + \mathbf{Q}_t^j - \left(\mathbf{Q}_{IC}^j + \mathbf{Q}_{TD}^j + \mathbf{Q}_v^j\right) \qquad (47)$$

In this equation, $\mathbf{Q}_b^j$ is the vector of the body forces. These equations can be used to solve for the acceleration vector $\ddot{\mathbf{e}}^j$. In the case of using more than one element, the element equations can be assembled to obtain the equations of motion of the ANCF mesh, which can be used to solve for the mesh accelerations.

3.4. Boundary Constraints and MBS Algorithms

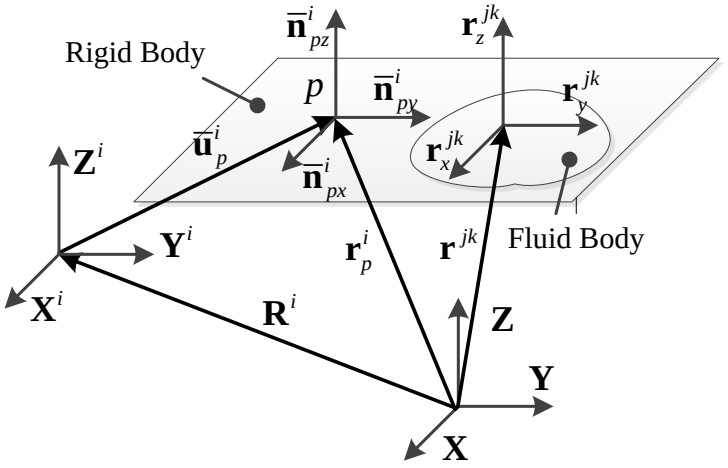

Figure 24. Boundary conditions

In many applications, the fluid interacts with the environment or with rigid and flexible bodies such as in the case of automobile or spacecraft with tanks filled with liquid. There are clear advantages of using a total Lagrangian approach for the integration of fluid and MBS algorithms. The constraints between the fluid and a surface can be systematically developed by using algebraic equations expressed in terms of the surface and fluid nodal coordinates. The use of the position vector gradients can facilitate the formulation of these algebraic constraint equations. Consider a rigid body i which interacts with the fluid body j as shown in Fig. 24. The configuration of the body is assumed to be defined using the reference coordinates $\mathbf{q}^i = \left[\mathbf{r}^{i\mathrm{T}}\ \boldsymbol{\theta}^{i\mathrm{T}}\right]^{\mathrm{T}}$, where $\mathbf{r}^i$ and

$\boldsymbol{\theta}^i$ are, respectively, the global position coordinates of the origin of the body reference and the set of orientation parameters which can be selected to be Euler parameters (Shabana, 2014). The transformation matrix that defines the body orientation is denoted as $\mathbf{A}^i$. Similarly, the coordinates of a selected marker p (coordinate system) on the body can be defined in the body coordinate system using the vector $\bar{\mathbf{u}}_p^i$, where subscript p refers to the marker point. The marker local transformation matrix can be defined as $\bar{\mathbf{A}}_p^i = \left[\bar{\mathbf{n}}_{px}^i \;\; \bar{\mathbf{n}}_{py}^i \;\; \bar{\mathbf{n}}_{pz}^i\right]$, where $\bar{\mathbf{n}}_{px}^i$, $\bar{\mathbf{n}}_{py}^i$ and $\bar{\mathbf{n}}_{pz}^i$ are three orthogonal unit vectors that define the axes of the marker coordinate system in the body coordinate system. Note that the global components of these axes can be defined as $\mathbf{n}_{pk}^i = \mathbf{A}^i \bar{\mathbf{n}}_{pk}^i, \;\; k = x, \, y, \, z$. Note also that the position vector of the marker reference point is given by $\mathbf{r}_p^i = \mathbf{R}^i + \mathbf{A}^i \bar{\mathbf{u}}_p^i$. Using these simple kinematic equations, the boundary constraints between the fluid and a surface that has an arbitrary displacement can be systematically developed. For example, the boundary constraints between the fluid nodes and the $x-y$ marker surface can be described using the three constraints $\mathbf{r}_x^{jk} \cdot \mathbf{n}_{pz}^i = 0$, $\mathbf{r}_y^{jk} \cdot \mathbf{n}_{pz}^i = 0$, and $\left(\mathbf{r}^{jk} - \mathbf{r}_p^i\right) \cdot \mathbf{n}_{pz}^i = 0$, where superscript k refers to the node number on the ANCF fluid body. These constraint equations prevent the fluid from penetrating the surface defined by the marker p. These algebraic equations can be implemented in a MBS algorithm in a straight forward manner. To this end, one defines the vector of boundary constraint functions as

$$\mathbf{C}\left(\mathbf{e}^{jk}, \mathbf{q}^i\right) = \left[\mathbf{r}_x^{jk} \cdot \mathbf{n}_{pz}^i \quad \mathbf{r}_y^{jk} \cdot \mathbf{n}_{pz}^i \quad \left(\mathbf{r}^{jk} - \mathbf{r}_p^i\right) \cdot \mathbf{n}_{pz}^i\right]^{\mathrm{T}} = \mathbf{0} \tag{48}$$

In this equation, $\mathbf{e}^{jk}$ is the vector of ANCF coordinates at node k. The constraint Jacobian matrix of the algebraic constraint equations can be written as

$$\mathbf{C}_{\mathbf{q}} = \begin{bmatrix} \mathbf{C}_{\mathbf{e}^{jk}} & \mathbf{C}_{\mathbf{q}^{i}} \end{bmatrix} = \begin{bmatrix} \dfrac{\partial\left(\mathbf{r}_x^{jk}\cdot\mathbf{n}_{pz}^{i}\right)}{\partial\mathbf{e}^{jk}} & \dfrac{\partial\left(\mathbf{r}_x^{jk}\cdot\mathbf{n}_{pz}^{i}\right)}{\partial\mathbf{q}^{i}} \\ \dfrac{\partial\left(\mathbf{r}_y^{jk}\cdot\mathbf{n}_{pz}^{i}\right)}{\partial\mathbf{e}^{jk}} & \dfrac{\partial\left(\mathbf{r}_y^{jk}\cdot\mathbf{n}_{pz}^{i}\right)}{\partial\mathbf{q}^{i}} \\ \dfrac{\partial\left(\left(\mathbf{r}^{jk}-\left(\mathbf{r}^{i}+\mathbf{A}^{i}\bar{\mathbf{u}}_p^{i}\right)\right)\cdot\mathbf{n}_{pz}^{i}\right)}{\partial\mathbf{e}^{jk}} & \dfrac{\partial\left(\left(\mathbf{r}^{jk}-\left(\mathbf{r}^{i}+\mathbf{A}^{i}\bar{\mathbf{u}}_p^{i}\right)\right)\cdot\mathbf{n}_{pz}^{i}\right)}{\partial\mathbf{q}^{i}} \end{bmatrix} \tag{49}$$

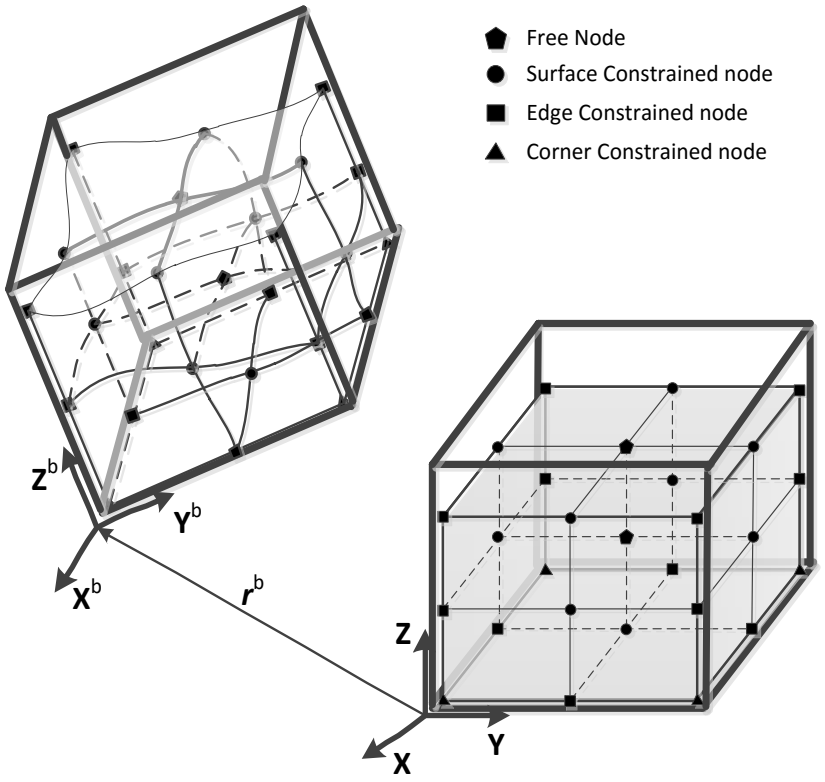

Figure 25. Fluid element in a container

Similar kinematic equations can also be used to model the fluid in a container as shown in Fig. 25. Other constraint types can also be developed and implemented systematically in MBS algorithms which are based on the following general Lagrangian virtual work principle $\delta\mathbf{q}^{\mathrm{T}}\left(\mathbf{M}\ddot{\mathbf{q}}+\mathbf{C}_{\mathbf{q}}^{\mathrm{T}}\boldsymbol{\lambda}-\mathbf{Q}_e\right)=0$, where $\mathbf{q}$ is the vector of system coordinates, $\mathbf{M}$ is the system mass matrix, $\boldsymbol{\lambda}$ is the vector of Lagrange multipliers, and $\mathbf{Q}_e$ is the vector of applied forces.

3.5. Numerical Examples

The objective of this chapter is to examine the performance of ANCF brick elements in solving liquid sloshing problems. To this end, several examples are considered in this section. The fluid ground interaction example is used to check if the boundary constraints were imposed in the dynamic system; the simple pendulum model is introduced to check the effects of the continuity condition; the zero gravity droplet model which is commonly used to check the if the surface tension (Yu et al., 2012, Thürey et al. 2010) is imposed correctly or not and in the end a sloshing model both in ANCF and FFR are made to see if the model could be well integrated with the MBS.

3.5.1 Fluid/Ground Surface Interaction

Only one finite element is used in this example with the assumption of *Newtonian fluid*. The results presented in this section clearly show that complex fluid shapes can be obtained using one ANCF element. The dimensions of the element are $a=b=c=1\text{m}$, while the mass density $\rho=1.0\times10^{3}\,\text{kg/m}^{3}$, the gravity force $\mathbf{F}_g=\left[0\ \ 0\ \ \text{-}9.8\right]^{\text{T}}\,\text{m/s}^{2}$, the penalty coefficient $k_{IC}=1.0\times10^{6}\ \text{N/m}$, and the shear viscosity $\mu=0.00093\,\text{Pas}$. The simulation time is assumed to be 1s. In this simulation scenario, the fluid element bottom surface is assumed to be in contact with the ground. The fluid is assumed to move freely under the effect of gravity. The results of the simulation for the IPAE and BSAE one-element mesh are shown in Figs. 26a and 26b, respectively. These results show that the fluid collapses rapidly as evident by the decrease of the height from 1 m to very small value. The results show that the one-BSAE mesh can capture more displacement modes as compared to the one-IPAE mesh. The top surface of the BSAE mesh assumes the

expected circular shape, while the surface of the IPAE mesh maintains rectangular shape as shown in Fig. 26. The results obtained also demonstrated that the fluid maintained constant volume. This simulation scenario also shows that the proposed ANCF fluid elements can capture large displacements using a total Lagrangian approach.

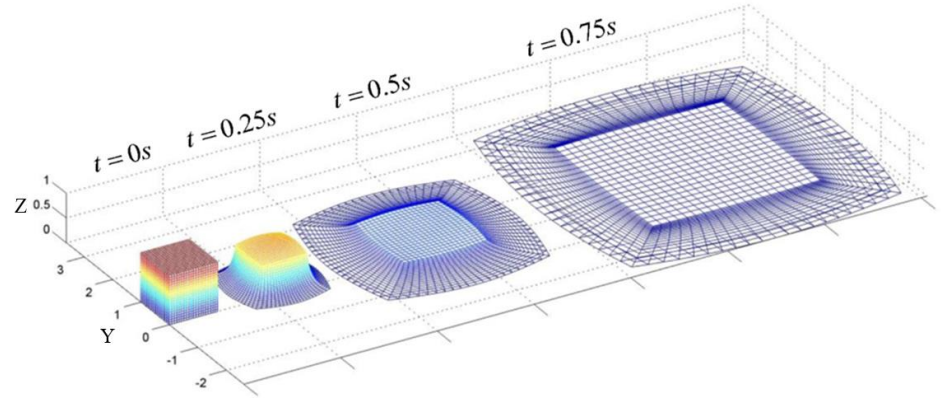

(a) IPAE example

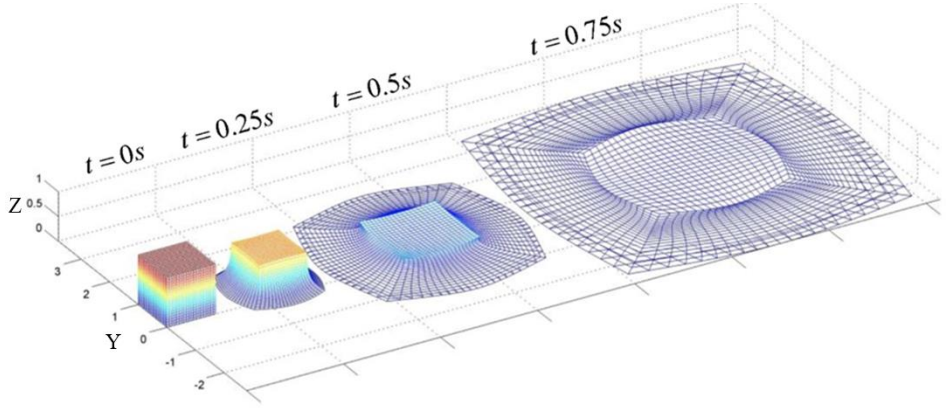

(b) BSAE example

Figure 26. Fluid/ground surface interaction using one element

3.5.2 Continuity Conditions

In this example, the eight-IPAE mesh, shown in Fig. 23, which consists of 8 elements, each of which has the same dimensions and material properties as the one-element mesh previously

considered will be used to examine the effect of changing the degree of continuity. In this example, the fluid body has dimensions $A = B = C = 2\text{m}$. The total simulation time for all the scenarios considered is 1s. In one scenario, no continuity conditions are imposed except for the continuity achieved by a standard FE assembly procedure, as previously discussed in this chapter, this is the case shown in Fig. 27a. In the second scenario, Fig. 27b, the linear algebraic constraint equations previously discussed in this chapter are applied in order to ensure C^1 continuity at the element interface. The simulation results demonstrated that the IPAE fluid model with higher degree of continuity assumes the expected circular shape under the gravity effect, while the model without the continuity constraints cannot describe the geometry accurately in this example. Figure 28. shows that the IPAE mesh with continuity constraints has smoother gradients than the one without continuity condition.

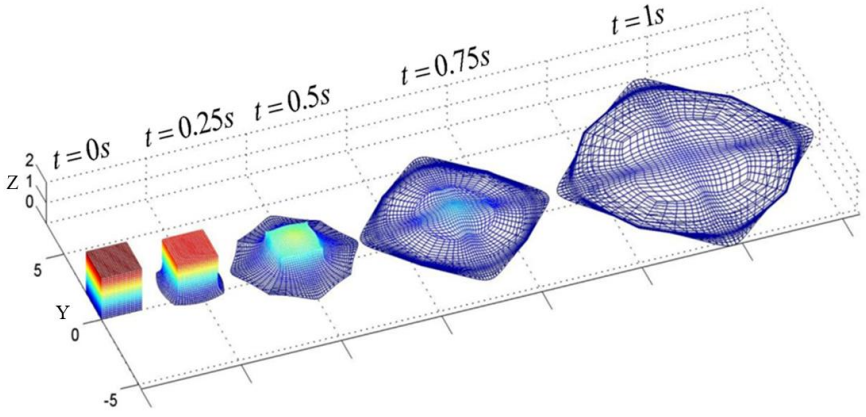

(a) Without continuity constraints

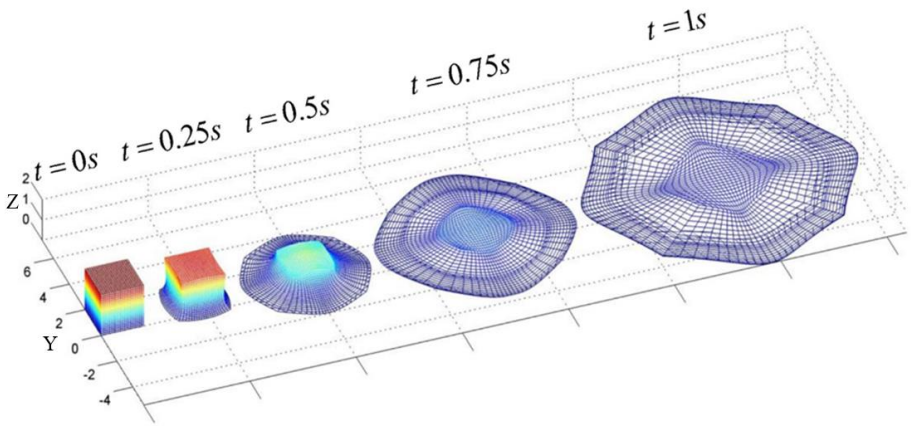

(b) With continuity constraints

Figure 27. Fluid/ground surface interaction without and with continuity constraints using an eight-IPAE mesh.

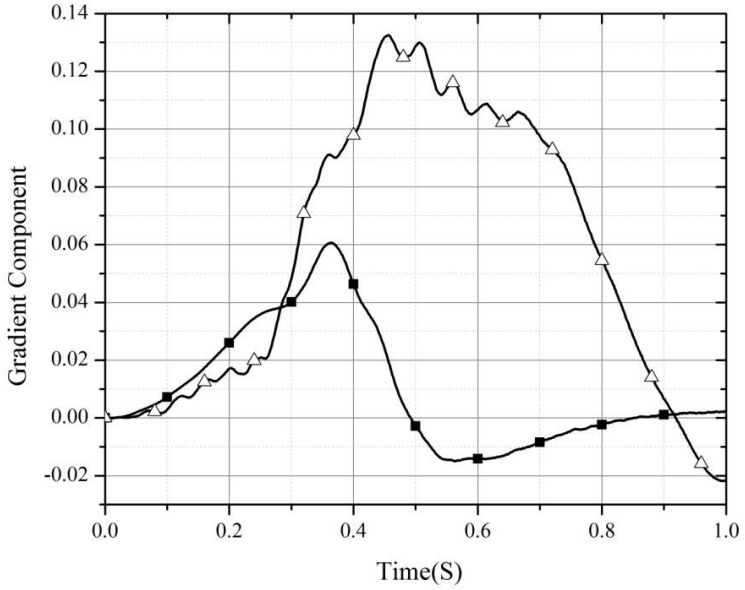

Figure 28. The Z component of $\mathbf{r}_x$ of node number 10 in eight-IPAE mesh (—■—Continuity , —△— Without continuity)

3.5.3 Effect of Surface Tension

In this simulation scenario, the fluid body is modeled using an eight-IPAE mesh. No continuity conditions are used and the fluid is assumed to deform freely under the effect of the surface tension

($\boldsymbol{\sigma} = 1000\mathbf{I}$, where $\mathbf{I}$ is a 3×3 identity matrix). The gravity effect is not considered in this example. This scenario can be used to simulate the motion of a liquid cube in space. The surface tension has the effect of changing the cubic shape to a nearly sphere droplet as shown in Fig. 29. However, because of the assumed polynomial functions, the cubic shape does not change to exact sphere. In order to have exact sphere or conic shapes, rational ANCF brick elements need to be used. The development of rational ANCF brick elements will be the subject of future investigations.

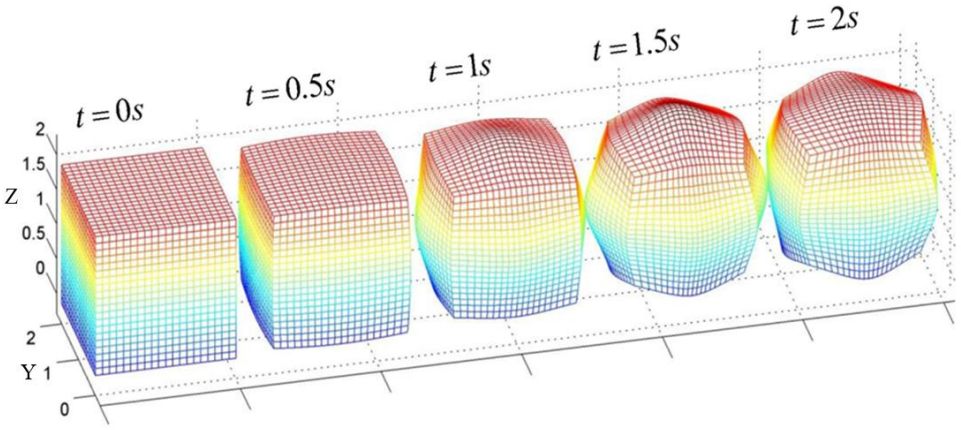

Figure 29. Effect of surface tension using eight-IPAE mesh

3.5.4 Sloshing in Moving Containers

In this example, the one-element model previously considered in this section is used to fill a container subjected to a prescribed harmonic motion with different frequencies in the y direction. As shown in Fig. 30, when the container movement is $0.1\sin(3t)$, the fluid experiences sloshing and the height reaches 1.16 m. The height reaches 1.35m for the $0.1\sin(8t)$ movement and 2.23m for the $0.3\sin(8t)$ movement. By investigating these three results, one could see that if the harmonic motions have the same amplitude, increasing the frequency would lead to the more sever fluid sloshing, while in the other case, if the harmonic motions have the same frequency, increasing

the amplitude would also lead to more sever fluid sloshing, which are consistent with common sense.

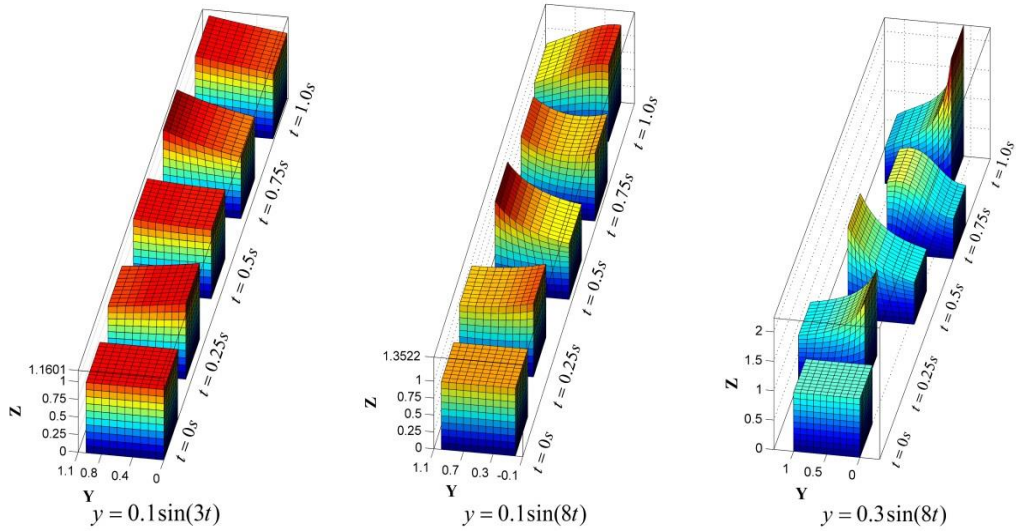

Figure 30. Sloshing problem solution using one element (Wei and Shabana, 2014)

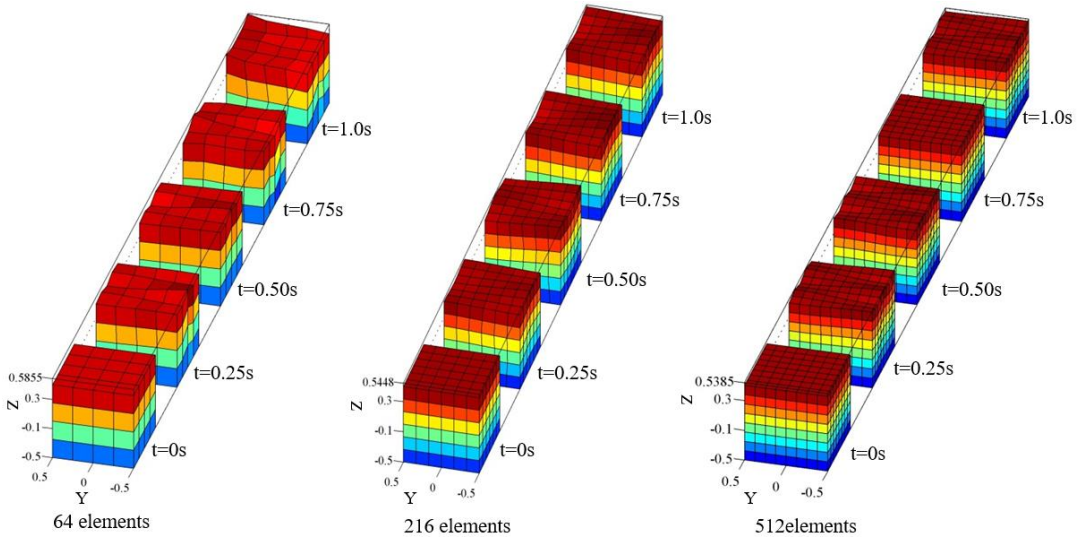

Figure 31. Sloshing problem using the FFR formulation

3.5.5 Comparison with the FFR Model

A fluid in a moving container model was developed using the floating frame of reference (FFR) formulation (Wang et al., 2014). The container is subjected to a prescribed harmonic motion in the

lateral direction defined by the function $0.1\sin(3t)$. It can be noticed from the results presented in Fig. 31 that the shape of the free surface could only be described properly by using large number of finite elements when the FFR formulation is used. The results show that one ANCF finite element tends to perform better than large number of elements of the FFR formulation in which linear modes are used to describe the fluid motion (Wang et al., 2014).

3.6 Concluding Remarks

A total Lagrangian ANCF finite element approach is proposed for liquid sloshing problems. The ANCF fluid elements allow for successful integration of fluid and MBS algorithms. Using the total Lagrangian approach, the fluid boundary conditions can be systematically introduced. The proposed ANCF brick elements have a constant inertia matrix, ensure the gradient continuity at the element nodes, and do not impose any restriction on the amount of rotation or deformation within the elements. The feasibility of implementing these fluid elements was demonstrated using several simple examples. The results show that complex fluid geometry can be obtained using one ANCF finite element. The results also show that in some simulation scenarios more realistic geometry can be obtained by increasing the degree of continuity at the IPAE interface. Furthermore, more complex geometry can be captured by using ANCF meshes with more finite elements, allowing for future investigations of more complex fluid problems using a total Lagrangian approach. The future work will focus on integrating this fluid model with vehicle or any flexible or rigid multibody system to study the interaction between the solid and liquid.

CHAPTER 4

ANCF TEXTILE MATERIAL AND ROLL-DRAFTING PROCESS

This chapter presents a new flexible multibody system (MBS) approach for modeling textile systems including roll-drafting sets used in chemical textile machinery. The proposed approach can be used in the analysis of textile materials such as lubricated polyester filament bundles (PFB), which have un-common material properties best described by specialized continuum mechanics constitutive models. In this investigation, the absolute nodal coordinate formulation (ANCF) is used to model PFB as a hyper-elastic transversely isotropic material. The PFB strain energy density function is decomposed into a fully isotropic component and an orthotropic, transversely isotropic component expressed in terms of five invariants of the right Cauchy-Green deformation tensor. Using this energy decomposition, the second Piola-Kirchhoff stress and the elasticity tensors can also be split into isotropic and transversely isotropic parts. The constitutive equations are used to define the generalized material forces associated with the coordinates of three-dimensional fully-parameterized ANCF finite elements. The proposed approach allows for modeling the dynamic interaction between the rollers polyester filament bundle and allows for using spline functions to describe the PFB forward velocity. This chapter demonstrates that the textile material constitutive equations and the MBS algorithms can be used effectively to obtain numerical solutions that define the state of strain of the textile material and the relative slip between rollers and PFB.

4.1 Textile Material Constitutive Equations

In this section, the transversely isotropic linear and nonlinear constitutive models of textile material are discussed. The elastic coefficients which enter into the formulation of the two constitutive models are defined (Bonet and Burton, 1997). The PFB constitutive models are used as examples in this investigation. In the development of the nonlinear model presented in this section, the total strain energy for transversely isotropic materials is expressed in terms of five strain invariants and is written as the sum of a fully isotropic component and an orthotropic, transversely isotropic component. Similarly, the second Piola-Kirchhoff stress tensor and the tensor of the elastic coefficients are split into isotropic and transversely isotropic parts. In order to generalize the strain energy equations to the fully nonlinear regime, the neo-Hookean potential is used to describe the isotropic component of the strain density function, while the orthotropic, transversely isotropic part follows the strain density function defined by Bonet and Burton (Bonet and Burton, 1997). In the nonlinear constitutive model presented in this section, the total strain energy function is written in terms of five independent coefficients, and coupling between different deformation modes is captured by using different Poisson ratios.

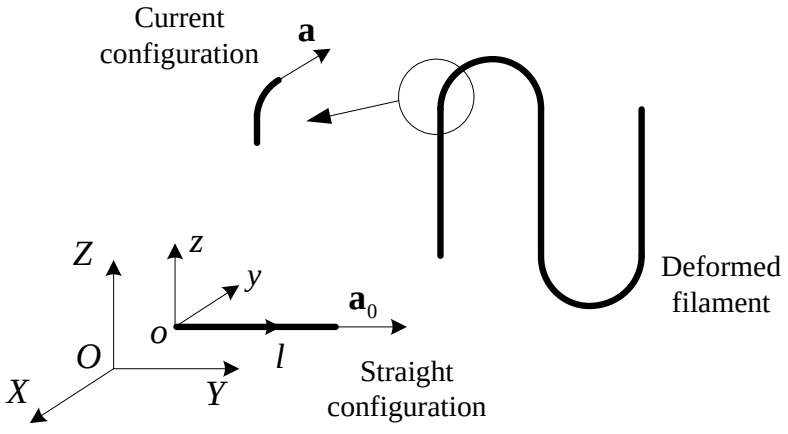

Figure 32. Filament coordinate system for transverse isotropy

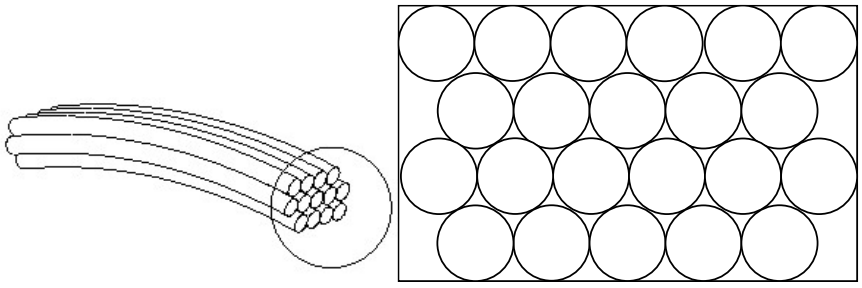

Figure 33. Filament bundle and its cross section

4.1.1 Small Strain Orthotropic Elasticity

Curisks and Carnaby (1985) treated the PFB as a continuum material. The PFB symmetric properties are used to relate the six stress components to the six strain components through a tangent compliance matrix, which defines the constitutive properties of the material. This matrix has been widely used to improve textile structure models. If expressed in a vector form, the strain-stress relationship can be written as $\boldsymbol{\varepsilon}_v = \mathbf{C}\boldsymbol{\sigma}_v$, where $\boldsymbol{\varepsilon}_v$ is the strain vector, $\mathbf{C}$ is the compliance matrix, and $\boldsymbol{\sigma}_v$ is the stress vector. The coordinate system of the filament bundle is oriented as shown in Fig. 32, where l defines the longitudinal direction along the fiber axis and the cross section is defined in the $y-z$ plane. As shown in Fig. 33, in the ideal case, all the filaments in the bundle can be assumed to be arranged parallel to each other. The gap among bundle filaments is filled with oil and water, thus making the PFB cross section mechanically isotropic. The linear transversely isotropic material strain-stress relationship can be written as

$$\begin{Bmatrix} \varepsilon_{ll} \\ \varepsilon_{yy} \\ \varepsilon_{zz} \\ \gamma_{ly} \\ \gamma_{zl} \\ \gamma_{yz} \end{Bmatrix} = \begin{bmatrix} 1/E_L & -\nu_{TL}/E_T & -\nu_{TL}/E_T & 0 & 0 & 0 \\ -\nu_{LT}/E_L & 1/E_T & -\nu_{TT}/E_T & 0 & 0 & 0 \\ -\nu_{LT}/E_L & -\nu_{TT}/E_T & 1/E_T & 0 & 0 & 0 \\ 0 & 0 & 0 & 1/G_{TL} & 0 & 0 \\ 0 & 0 & 0 & 0 & 1/G_{TL} & 0 \\ 0 & 0 & 0 & 0 & 0 & 1/G_{TT} \end{bmatrix} \begin{Bmatrix} \sigma_l \\ \sigma_y \\ \sigma_z \\ \sigma_{ly} \\ \sigma_{zl} \\ \sigma_{yz} \end{Bmatrix} \tag{50}$$

where ε_{ij} and $\gamma_{ij}, i, j = l, y, z$ denote axial and shear Green-Lagrange strains, respectively, E_L is the longitudinal elastic modulus governing uniaxial loading in the longitudinal direction l, ν_{LT} is the Poisson ratio that accounts for the effect of the longitudinal strains in the transverse directions, E_T is the transverse elastic modulus governing uniaxial loading in the transverse (y or z) direction, ν_{TT} is the associated Poisson ratio governing the resultant strains in the remaining orthogonal transverse directions (y or z), ν_{TL} is the corresponding Poisson ratio governing the induced strain in the longitudinal direction, G_{TL} is the shear modulus governing shear in the longitudinal direction, and G_{TT} is the shear modulus governing shear in the transverse plane. For the strain energy function to exist, the matrix of elastic coefficients must be symmetric. This implies the relation $-\nu_{TL}/E_T = -\nu_{LT}/E_L$ must hold. Also, there exist other restrictions in the range of permitted values for these material constants (Christensen, 1979), for instance, $E_L, E_T, G_{TL}, G_{TT} > 0$, $G_{TT} = E_T/\left[2(1+\nu_{TT})\right]$, $|\nu_{TL}| \le (E_T/E_L)^{1/2}$, $|\nu_{LT}| \le (E_L/E_T)^{1/2}$, $|\nu_{TT}| < 1$, and $1-\nu_{TT} > 2\nu_{LT}^2 E_T/E_L$. Using these relations, one can also write the stress-strain relationship $\boldsymbol{\sigma}_v = \mathbf{D}\boldsymbol{\varepsilon}_v$, where $\mathbf{D}$ is the matrix of elastic coefficients and $\mathbf{D} = \mathbf{C}^{-1}$.

$$\mathbf{D}=\begin{bmatrix} \frac{E_L\left(1-\nu_{TT}\right)}{m} & \frac{E_L\nu_{LT}}{m} & \frac{E_L\nu_{LT}}{m} & 0 & 0 & 0 \\ \frac{E_L\nu_{LT}}{m} & \frac{E_T\left(1-n\nu_{LT}^2\right)}{m\left(1+\nu_{TT}\right)} & \frac{E_T\left(n\nu_{LT}^2+\nu_{TT}\right)}{m\left(1+\nu_{TT}\right)} & 0 & 0 & 0 \\ \frac{E_L\nu_{LT}}{m} & \frac{E_T\left(n\nu_{LT}^2+\nu_{TT}\right)}{m\left(1+\nu_{TT}\right)} & \frac{E_T\left(1-n\nu_{LT}^2\right)}{m\left(1+\nu_{TT}\right)} & 0 & 0 & 0 \\ & 0 & 0 & G_{TL} & 0 & 0 \\ & 0 & 0 & 0 & G_{TL} & 0 \\ & 0 & 0 & 0 & 0 & G_{TT} \end{bmatrix} \tag{51}$$

where $n=E_T/E_L$, $m=1-\nu_{TT}-2n\nu_{LT}^2$.

4.1.2 Invariants of Transversely Isotropic Materials

Let $\mathbf{x}$ be the position vector of a material point in the undeformed (reference) configuration, and $\mathbf{r}=\mathbf{r}\left(\mathbf{x},t\right)$ be the corresponding position vector in the deformed configuration. The matrix of position vector gradients $\mathbf{J}$ is defined as $\mathbf{J}=\partial\mathbf{r}/\partial\mathbf{x}$. It is required that $\mathbf{J}$ satisfies $J=\left|\mathbf{J}\right|>0$, where J is the determinant of $\mathbf{J}$ and it represents the ratio of the deformed volume dv to the undeformed volume dV. The right Cauchy-Green deformation tensor is defined as $\mathbf{C}_r=\mathbf{J}^{\mathrm{T}}\mathbf{J}$. The second Piola-Kirchhoff stress tensor may be obtained using the derivative of the elastic energy as $\boldsymbol{\sigma}_{P2}=2\partial U/\partial\mathbf{C}_r$, where U is the strain energy density function. The first Piola-Kirchhoff stress tensor may be defined in terms of the second Piola-Kirchhoff stress tensor as $\boldsymbol{\sigma}_{P1}=\mathbf{J}\boldsymbol{\sigma}_{P2}$, and the Cauchy stress tensor $\boldsymbol{\sigma}=J^{-1}\mathbf{J}\boldsymbol{\sigma}_{P2}\mathbf{J}^{\mathrm{T}}$. In this case, the elasticity tensor can be derived as $\mathbf{C}=2\partial\boldsymbol{\sigma}_{P2}/\partial\mathbf{C}_r=4\partial^2U/\partial\mathbf{C}_r^2$. For the nonlinear hyper-elastic case, the elasticity tensor can be function of the strains, unlike the linear case considered in section 4.1.1.

It is convenient to represent the strain energy function in terms of the invariants of $\mathbf{C}_r$. In the isotropic case, one can write $U = U_{iso}\left(I_1,\ I_2,\ I_3\right)$, where U_{iso} stands for the strain energy for the isotropic material, and the three principal invariants of $\mathbf{C}_r$ are defined as

$$I_1 = \mathrm{tr}\left(\mathbf{C}_r\right),\ I_2 = \frac{1}{2}\left\{\left(\mathrm{tr}\left(\mathbf{C}_r\right)\right)^2 - \mathrm{tr}\left(\mathbf{C}_r^2\right)\right\},\ I_3 = \det\left(\mathbf{C}_r\right) \tag{52}$$

In the case of incompressible materials, $J = 1$, and therefore, the strain energy depends only on the first and second invariants, that is, $U = U_{iso,inc}\left(I_1,\ I_2\right)$.

In the case of transversely isotropic material with one family of fibers oriented along one direction, there are two additional invariants. If the fibers are aligned in the direction of the unit vector $\mathbf{a}_0$ in the reference configuration, the structure tensor is defined as $\mathbf{A}_0 = \mathbf{a}_0 \otimes \mathbf{a}_0$ (Spencer, 1971), and the new invariants that can be used to describe the deformation of the fiber family are

$$I_4 = \mathbf{C}_r : \mathbf{A}_0, \quad I_5 = \mathbf{C}_r^2 : \mathbf{A}_0 \tag{53}$$

The invariant I_4 has a straightforward physical meaning and can be calculated as $I_4 = \lambda_{\mathbf{a}}^2$, where $\lambda_{\mathbf{a}}$ is the fiber stretch, and I_5 is related to the way the fibers couple shear deformations. The vector $\mathbf{a}$ is a unit vector which corresponds to $\mathbf{a}_0$ into the current configuration, that is, $\mathbf{a} = \mathbf{J}\mathbf{a}_0 / \left\|\mathbf{J}\mathbf{a}_0\right\|$.

In the case of two families of fibers, there are four additional invariants of the deformation tensor. If the fibers are aligned in the directions of $\mathbf{a}_0$ and $\mathbf{g}_0$ in the reference configuration, the structure tensors characterizing these fiber families are $\mathbf{A}_0 = \mathbf{a}_0 \otimes \mathbf{a}_0$ and $\mathbf{G}_0 = \mathbf{g}_0 \otimes \mathbf{g}_0$ (Kao et al., 2010). In addition to the invariants from the transversely isotropic case, $I_{6\text{–}9}$ are defined as

$$I_6 = \mathbf{C}_r : \mathbf{G}_0,\ I_7 = \mathbf{C}_r^2 : \mathbf{G}_0,\ I_8 = \mathrm{tr}\left(\mathbf{C}_r\mathbf{A}_0\mathbf{G}_0\right),\ I_9 = \mathrm{tr}\left(\mathbf{A}_0\mathbf{G}_0\right) \tag{54}$$

If $\mathbf{a}_0$ and $\mathbf{g}_0$ are orthogonal to one another, the invariant I_8 is identically zero and does not enter into the formulation of the material model. The filament bundle model considered in this chapter is assumed to be a transversely isotropic material which involves five of the invariants mentioned above. For this case, the strain energy function may be written as

$$U = U_{trn}\left(I_1,\, I_2,\, I_3,\, I_4,\, I_5\right) \tag{55}$$

where U_{trn} stands for the strain energy density function of the transversely isotropic material. Using the equations presented in this section, the stress and elasticity tensors for the nonlinear transversely isotropic material can be derived.

4.1.3 Transversely Isotropic Material Constitutive Equations

The strain energy for transversely isotropic materials can be decomposed into a fully isotropic component and an orthotropic, transversely isotropic component (Bonet and Burton, 1997). Using the developments previously presented in this section, one can write the total strain energy as

$$U = U_{iso}\left(I_1,\, I_2,\, I_3\right) + U_{trn}\left(I_1,\, I_2,\, I_3,\, I_4,\, I_5\right) \tag{56}$$

Consequently, the second Piola-Kirchhoff stresses and the elasticity tensor can also be split into isotropic and transversely isotropic parts as

$$\left.\begin{aligned} \boldsymbol{\sigma}_{P2} &= \boldsymbol{\sigma}_{P2(iso)} + \boldsymbol{\sigma}_{P2(trn)} = 2\frac{\partial U_{iso}}{\partial \mathbf{C}_r} + 2\frac{\partial U_{trn}}{\partial \mathbf{C}_r} \\ \mathbf{C} &= \mathbf{C}_{iso} + \mathbf{C}_{trn} = 4\frac{\partial^2 U_{iso}}{\partial \mathbf{C}_r^2} + 4\frac{\partial^2 U_{trn}}{\partial \mathbf{C}_r^2} \end{aligned}\right\} \tag{57}$$

In order to generalize the strain energy equations to the fully nonlinear regime, the neo-Hookean potential is used to describe the isotropic component of the strain density function, and the

transversely part follows the strain density function defined by Bonet and Burton (1997). One can then use the following strain energy expressions:

$$\left.\begin{aligned} U_{iso} &= \frac{1}{2}\mu\left(I_1-3\right)-\mu\ln J+\frac{\lambda}{2}\left(\ln J\right)^2 \\ U_{trn} &= \left[\alpha+\beta\ln J+\gamma\left(I_4-1\right)\right]\left(I_4-1\right)-\frac{\alpha}{2}\left(I_5-1\right) \end{aligned}\right\} \tag{58}$$

Note that if the material has initially no strain energy stored, $I_1=3$, $J=1$, $I_4=I_5=1$, and the preceding equations lead to zero strain energy as expected. The coefficients in the preceding equations are defined as

$$\left.\begin{aligned} &\lambda=\frac{E_T\left(nv_{LT}^2+v_{TT}\right)}{m\left(1+v_{TT}\right)},\quad \mu=\frac{1}{2}\left(\frac{E_T\left(1-nv_{LT}^2\right)}{m\left(1+v_{TT}\right)}-\lambda\right)=G_{TT} \\ &\alpha=\mu-G_{TL}=\mu-\frac{E_L}{2\left(1+v_{LT}\right)},\quad \beta=\frac{1}{4}\left(\frac{E_L v_{LT}}{m\left(1+v_{TT}\right)}-\lambda\right), \\ &\gamma=\frac{1}{8}\left(\frac{E_L\left(1-v_{TT}\right)}{m}+4\alpha-\lambda-2\mu\right)-\beta \end{aligned}\right\} \tag{59}$$

There are only five independent material constants, which are E_L, E_T, v_{TT}, v_{LT}, G_{TL}. In this investigation, different Poisson ratios ($v_{TT}\neq v_{LT}$) are used in order to be consistent with the definition of transversely isotropic material. This modified constitutive model will be used to formulate the PFB mechanical properties which define the generalized stress forces as will be discussed in the following section.

4.2 Elastic Force Implementation

The constitutive equations presented in the preceding section are implemented in this investigation using a three-dimensional, fully-parameterized ANCF beam element (Shabana and Yakoub, 2001).

ANCF elements can describe rigid body motion using a non-incremental solution procedure and allow for a straightforward implementation of nonlinear constitutive equations.

4.2.1 Element Kinematics

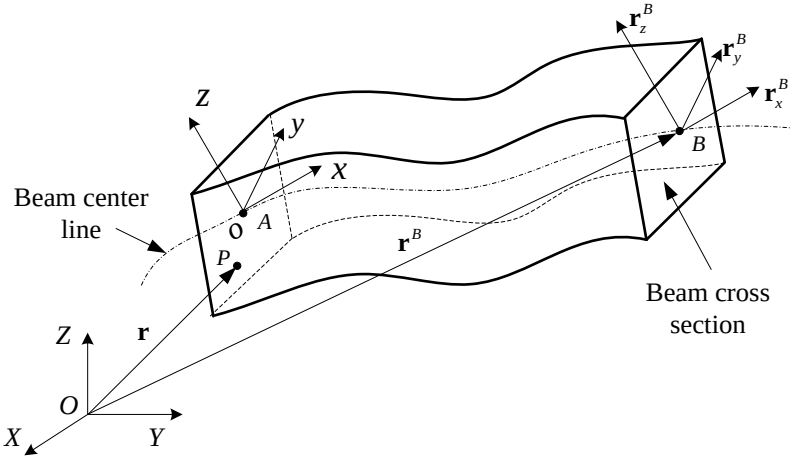

Figure 34. ANCF three-dimensional beam element

In this subsection, the ANCF three-dimensional beam element, shown in Fig. 34, is briefly discussed. This element employs polynomials that are cubic in the longitudinal direction *x* and linear in the transverse directions *y* and *z*, where *x*, *y*, and *z* are the local element spatial coordinates. The configuration of the beam element is determined by the position and gradient vectors of the two end nodes *A* and *B*. Each node has 12 coordinates which may be arranged in a column vector. For example, the coordinates of node i, can be written as $\mathbf{e}^i = \left[\mathbf{r}^{iT}\ \mathbf{r}_x^{iT}\ \mathbf{r}_y^{iT}\ \mathbf{r}_z^{iT}\right]^{\mathrm{T}}$, where $\mathbf{r}^i$ is the position vector of node i, $i = A, B$, and $\mathbf{r}_x^i$, $\mathbf{r}_y^i$, and $\mathbf{r}_z^i$ are the gradient vectors defined in the global inertial system XYZ. The element has 24 nodal coordinates given by the vector $\mathbf{e} = \left[\mathbf{e}^{AT}\ \mathbf{e}^{BT}\right]^{\mathrm{T}}$. The location of an arbitrary point *P* on the beam element can be written as $\mathbf{r} = \mathbf{S}(x, y, z)\mathbf{e}$, where $\mathbf{S}$ is a space dependent element shape function matrix which is defined as $\mathbf{S} = \left[S_1\mathbf{I}\ S_2\mathbf{I}\ S_3\mathbf{I}\ S_4\mathbf{I}\ S_5\mathbf{I}\ S_6\mathbf{I}\ S_7\mathbf{I}\ S_8\mathbf{I}\right]$, $\mathbf{I}$ is the 3×3 identity matrix, and $S_1 = 1 - 3\xi^2 + 2\xi^3$,

$S_2 = l\left(\xi - 2\xi^2 + \xi^3\right)$, $S_3 = l\left(\eta - \xi\eta\right)$, $S_4 = l\left(\zeta - \xi\zeta\right)$, $S_5 = 3\xi^2 - 2\xi^3$, $S_6 = l\left(-\xi^2 + \xi^3\right)$, $S_7 = l\xi\eta$, and $S_8 = l\xi\zeta$ are the shape functions, where the dimensionless parameters ξ, η, and ζ are defined as $\xi = x/l$, $\eta = y/l$, and $\zeta = z/l$, and l is the length of the beam element in the undeformed configuration.

4.2.2 Cross Section Deformation

Nanson's formula (Ogden, 1984) defines the relationship between the area in the current configuration *ds* and the area in the undeformed reference configuration *dS* as $ds = \left(J/\sqrt{\mathbf{n}^{\mathrm{T}}\mathbf{J}\mathbf{J}^{\mathrm{T}}\mathbf{n}}\right)dS$, where $\mathbf{J} = \left[\mathbf{r}_x\ \mathbf{r}_y\ \mathbf{r}_z\right]$ is the position vector gradient matrix, *J* is the determinant of $\mathbf{J}$, $\mathbf{n}$ is a unit vector perpendicular to the cross section area in the current configuration, which can be defined as $\mathbf{n} = \left(\mathbf{r}_y \times \mathbf{r}_z\right)/\left\|\mathbf{r}_y \times \mathbf{r}_z\right\|$. Using ANCF finite elements, Nanson's formula can be evaluated in a straightforward manner. It has been observed that when a linear elastic constitutive law is used in modeling textile materials subjected to large deformation, the deformed area decreases and may reach zero or even negative values. These singular configurations are not encountered when nonlinear constitutive laws are used with ANCF finite elements as previously reported in the literature (Maqueda and Shabana, 2007).

4.2.3 Generalized Elastic Forces for Transversely Isotropic Materials

Using the strain energy function presented previously in this chapter, one can easily obtain the ANCF elastic forces for the hyper-elastic transversely isotropic material. The generalized elastic forces for the isotropic and transversely isotropic parts, $\mathbf{Q}_{iso}$ and $\mathbf{Q}_{trn}$, respectively, are obtained by differentiating the strain energy with respect to the elastic nodal coordinates as

$$\left.\begin{aligned}
\mathbf{Q}_{iso} &= \frac{\partial U_{iso}}{\partial \mathbf{e}} = \int_V \frac{\mu}{2}\left(\frac{\partial I_1}{\partial \mathbf{e}}\right) + \frac{\lambda \ln J - \mu}{J}\left(\frac{\partial J}{\partial \mathbf{e}}\right) dV \\
\mathbf{Q}_{trn} &= \frac{\partial U_{trn}}{\partial \mathbf{e}} = \int_V \left(\left[\alpha + \beta \ln J + 2\gamma\left(I_4 - 1\right)\right]\left(\frac{\partial I_4}{\partial \mathbf{e}}\right) + \left(I_4 - 1\right)\frac{\beta}{J}\left(\frac{\partial J}{\partial \mathbf{e}}\right) - \frac{\alpha}{2}\left(\frac{\partial I_5}{\partial \mathbf{e}}\right)\right) dV
\end{aligned}\right\} \tag{60}$$

The coefficients used in this equation were previously defined in this chapter. Without any loss of generality, in the three-dimensional textile machine model used in the numerical study presented in this investigation, the direction of the fibers is assumed to be along the Y axis. Therefore, one can define the unit vector $\mathbf{a}_0 = \begin{bmatrix} 0 & 1 & 0 \end{bmatrix}^{\mathrm{T}}$. In this case, one has

$$\left.\begin{aligned}
&\frac{\partial I_1}{\partial \mathbf{e}} = \frac{\partial \mathrm{tr}\left(\mathbf{C}_r\right)}{\partial \mathbf{e}} = 2\left(\mathbf{S}_x^{\mathrm{T}}\mathbf{r}_x + \mathbf{S}_y^{\mathrm{T}}\mathbf{r}_y + \mathbf{S}_z^{\mathrm{T}}\mathbf{r}_z\right)^{\mathrm{T}} \\
&\left(\frac{\partial J}{\partial \mathbf{e}}\right)^{\mathrm{T}} = \sum_{i=1}^{3} \mathbf{S}_{x,i}^{\mathrm{T}}\left(\mathbf{r}_y \times \mathbf{r}_z\right)_{,i} + \sum_{i=1}^{3} \mathbf{S}_{y,i}^{\mathrm{T}}\left(\mathbf{r}_z \times \mathbf{r}_x\right)_{,i} + \sum_{i=1}^{3} \mathbf{S}_{z,i}^{\mathrm{T}}\left(\mathbf{r}_x \times \mathbf{r}_y\right)_{,i} \\
&\frac{\partial I_4}{\partial \mathbf{e}} = \frac{\partial\left(\mathbf{C}_r : \mathbf{A}_0\right)}{\partial \mathbf{e}} = \frac{\partial\left(\mathbf{r}_y^{\mathrm{T}}\mathbf{r}_y\right)}{\partial \mathbf{e}} = 2\left(\mathbf{S}_y^{\mathrm{T}}\mathbf{r}_y\right)^{\mathrm{T}} \\
&\frac{\partial I_5}{\partial \mathbf{e}} = \frac{\partial\left(\mathbf{C}_r^2 : \mathbf{A}_0\right)}{\partial \mathbf{e}} = \frac{\partial\left(\left(\mathbf{r}_x^{\mathrm{T}}\mathbf{r}_y\right)^2 + \left(\mathbf{r}_y^{\mathrm{T}}\mathbf{r}_y\right)^2 + \left(\mathbf{r}_y^{\mathrm{T}}\mathbf{r}_z\right)^2\right)}{\partial \mathbf{e}} \\
&= 2\left[\mathbf{r}_x^{\mathrm{T}}\mathbf{r}_y\left(\mathbf{S}_y^{\mathrm{T}}\mathbf{r}_x + \mathbf{S}_x^{\mathrm{T}}\mathbf{r}_y\right) + 2\mathbf{r}_y^{\mathrm{T}}\mathbf{r}_y\left(\mathbf{S}_y^{\mathrm{T}}\mathbf{r}_y\right) + \mathbf{r}_y^{\mathrm{T}}\mathbf{r}_z\left(\mathbf{S}_z^{\mathrm{T}}\mathbf{r}_y + \mathbf{S}_y^{\mathrm{T}}\mathbf{r}_z\right)\right]^{\mathrm{T}}
\end{aligned}\right\} \tag{61}$$

where $\mathbf{S}_x$, $\mathbf{S}_y$, and $\mathbf{S}_z$ denote the first derivative of the shape function matrix with respect to the element coordinates, and the subscript "*,i*" denotes the first component (row) of a vector (matrix). The resulting elastic forces $\mathbf{Q}_{el} = \mathbf{Q}_{trn} + \mathbf{Q}_{iso}$ can be written in terms of the derivatives of the shape functions and the gradient vectors. Since the strains and stresses are defined in the reference configuration, the integration can be carried out using the element dimensions at the reference configuration. Gauss quadrature method is used to evaluate the integrations required for the evaluation of the generalized elastic forces.

4.3. Roll-drafting MBS Algorithm

This section describes the MBS model developed in this chapter to integrate the flexible filament bundle and the textile machine. The aim is to analyze the roll-drafting process accounting for the interaction between motion of the rollers, the hyper-elastic transversely isotropic PFB, and the velocity at the boundaries of one set of rollers (see Fig. 1). The contact formulation that captures the interaction between the flexible body and the rigid rollers, and the MBS constrained dynamics formulation used are also discussed in this section.

4.3.1 Roll-Drafting Model

Table 1. Roller parameters

Radius	Width	Contact stiffness coefficient (N/m)	Contact damping coefficient (Ns/m)	Friction coefficient
0.2m	0.7m	2×10^{6}	5×10^{4}	0.24

Table 2. Filament bundle element properties

Density	Length× Width× Thickness	E_L (Pa)	E_T (Pa)	v_{TT}	v_{LT}	G_{TL} (Pa)
$694\,kg/m^3$	0.08×0.4×0.008m	1.73×10^{9}	1×10^{8}	0.4	0.3	6.65×10^{8}

Table 3. Numerical integration parameters

Method	Simulation Time	Constraint tolerance	Integrator tolerance
Adams-Bashforth	3s	1×10^{-7}	1×10^{-7}

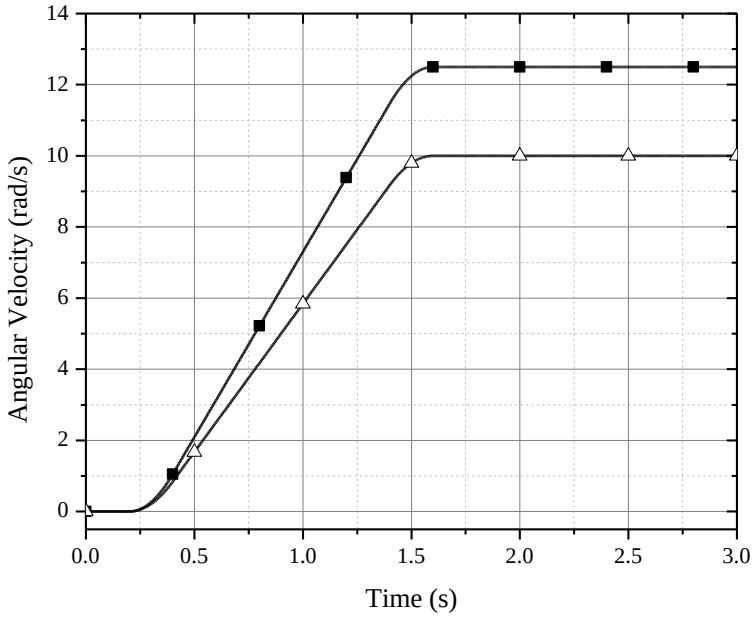

Figure 35. Angular velocity of the rollers
(—■— first scenario, —△— second scenario)

The roll-drafting model is developed in the *YZ* plane and consists of 7 rollers which have the same properties (shown in Table 1). The filament bundle is modeled using 127 ANCF fully parameterized three-dimensional beam elements. Some of the finite elements have an initially curved structure to match the geometry of rollers. The data of the beam elements are listed in Table 2. All the rollers are assumed to be connected to the ground by revolute joints, and their angular velocity is specified using spline data. Two different prescribed roller angular velocities, which are used in the numerical simulation to represent the influence of the machine operation parameters on the PFB deformation state, are introduced to the formulation as kinematic constraints. The time evolution of the angular velocity of these two sets of rollers is shown in Fig. 35. Contact forces are formulated using a penalty method which allows for small interpenetration and accounts for the effect of friction, which is required in the roll-drafting processes. In order for the filament bundle

on the output side to be driven straight, an additional support roller (Roller 8 in Fig. 37) is added to the textile machine. In the model developed in this investigation, the stretch of the filament bundle is produced using two sets of prescribed velocity constraints (as shown in Fig. 36). These constraints are imposed at the first and last nodes of the 127-node PFB model. The ratio of the front and end nodes velocity is utilized to introduce elongation in the textile material. Figure 37 shows the model developed for this study, while the numerical parameters of the simulations are shown in Table 3.

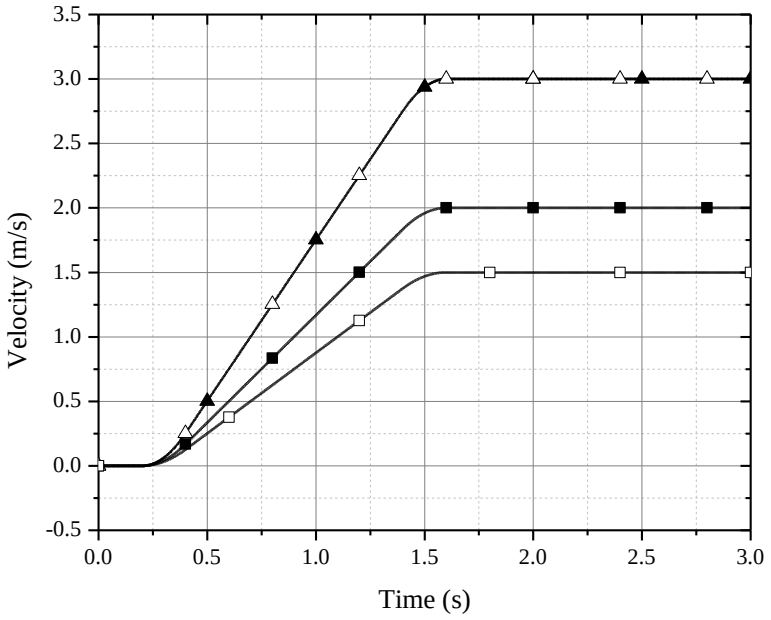

Figure 36. Forward velocity of the front and rear nodes (—■—first scenario rear node, —▲— first scenario front node, —△— second scenario front node, —□— second scenario rear node)

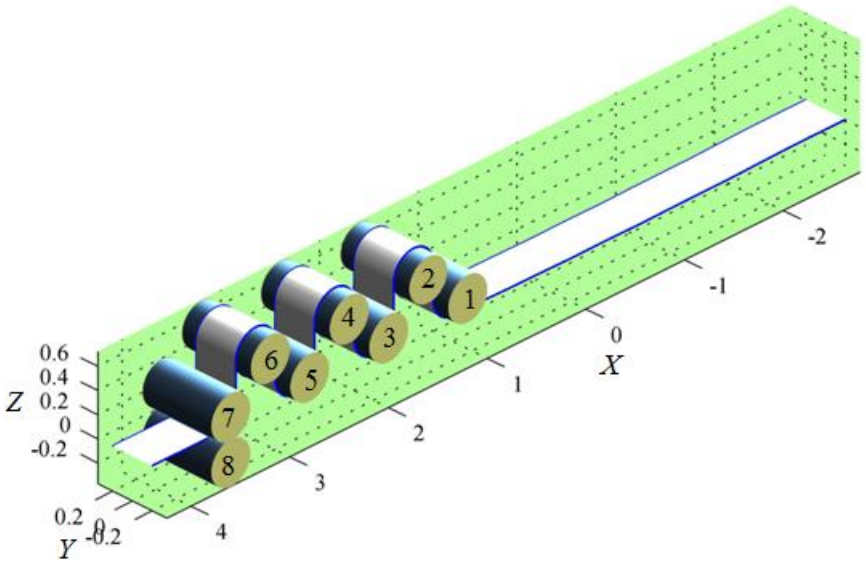

Figure 37. Snapshot of the system initial configuration

4.3.2 Starting the Roll-Drafting Process

Drawing machines start by smoothly increasing the angular velocity of rollers from zero to the maximum constant velocity in order to avoid a sudden change of the velocity that can cause high impulse forces. These forces can cause damage to the drawing machine. Therefore, the forward velocity constraints for the front and rear nodes must follow the same pattern. In this case, several spline functions are used to define constraints to smoothly increase the roller angular velocities and the PFB forward velocity. Because of introducing these velocity constraints and because the rollers are connected to the ground using revolute joints, the rollers have no remaining degrees of freedoms. The prescribed roller velocities as function of time are shown in Figs. 35-36.

4.3.3 Contact Forces

The filament-roller frictional contact model used in this chapter is similar to that proposed by Dufva et al. (2007). The penetration at the contact point between the finite element and the roller surface is determined and used in the calculation of the normal forces. The time rate of penetration is used to introduce damping forces that lead to energy dissipation. For an element i and a roller k, the normal force vector is defined as $\mathbf{f}_n^{ik} = F^{ik}\hat{\mathbf{n}}^{ik} = \left(E_r d^{ik} + c_r \dot{d}^{ik}\right)\hat{\mathbf{n}}^{ik}$, where $\mathbf{f}_n^{ik}$ is the normal force vector which has a magnitude F^{ik}, E_r and c_r are the contact stiffness and damping coefficients, respectively, d^{ik} is the penetration, $\dot{d}^{ik}$ is the time derivative of the penetration, $\hat{\mathbf{n}}^{ik} = \left(\mathbf{r}^i - \mathbf{r}^k\right) \Big/ \left\|\mathbf{r}^i - \mathbf{r}^k\right\|$, as shown in Fig. 38, is the unit normal, and $\mathbf{r}^i$ is the global position vector of the contact point on element i and $\mathbf{r}^k$ is the global position vector of the geometric center of the kth roller. The penetration at a contact point is determined as $d^{ik} = R^k - \left\|\mathbf{d}^{ik}\right\|$, where R^k is the radius of the roller k and $\mathbf{d}^{ik} = \mathbf{r}^i - \mathbf{r}^k$ is a vector that defines the position of the contact point on element i with respect to the center of the roller *k* defined by point O_k. The vector $\mathbf{d}^{ik}$ can be used to define the current normal to the surface and, consequently, will be taken as the normal force direction. Contact is assumed if $R^k \geq \left\|\mathbf{d}^{ik}\right\|$.

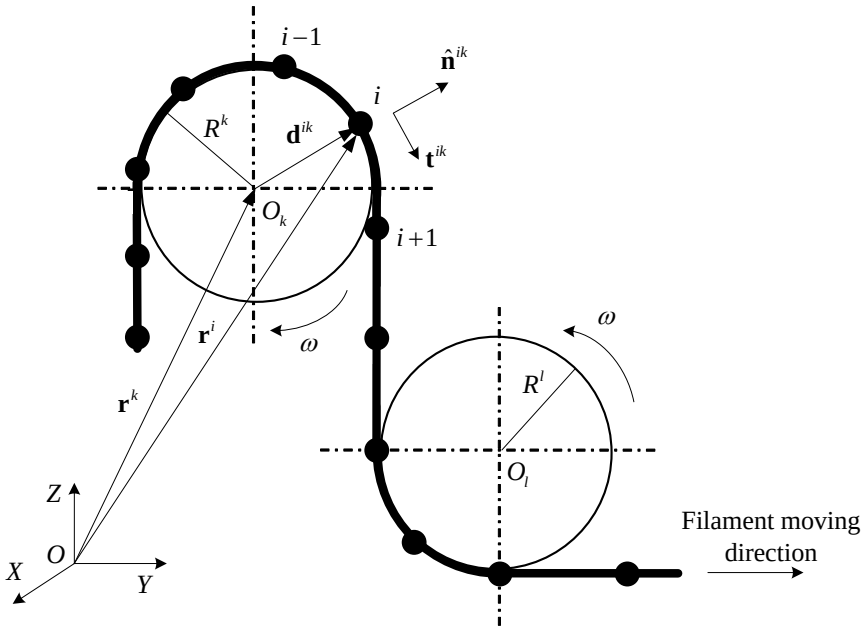

Figure 38 Description of filament-roller contact

The tangential or friction component of the contact force, $\mathbf{f}_f^{ik}$, depends on the relative velocity at the contact point. The relative velocity vector at the contact point is defined as $\mathbf{v}_r^{ik} = \mathbf{v}^i - \mathbf{v}^k$ where $\mathbf{v}^i$ is the velocity vector of the contact point on element i, which is obtained as a function of the element absolute nodal coordinates as $\mathbf{v}^i = \mathbf{S}\dot{\mathbf{e}}^i$, and $\mathbf{v}^k$ is the velocity vector of the contact point on the roller surface. The tangential component of the relative velocity $\mathbf{v}_t^{ik}$ can be written as $\mathbf{v}_t^{ik} = \mathbf{v}_r^{ik} - \left(\mathbf{v}_r^{ik\mathrm{T}}\hat{\mathbf{n}}^{ik}\right)\hat{\mathbf{n}}^{ik}$. A unit tangent vector $\mathbf{t}^{ik}$ in the direction of the slip can then be defined as $\mathbf{t}^{ik} = \mathbf{v}_t^{ik} \big/ \left\|\mathbf{v}_t^{ik}\right\|$. The friction force can then be defined as $\mathbf{f}_f^{ik} = -\mu F^{ik}\mathbf{t}^{ik}$, where μ is the friction coefficient between the roller k and the filament bundle. In this study, the friction coefficients are considered to be constant. However, an exponential smoothing technique is used to avoid numerical problems when the friction forces change sign in the neighborhood of

zero relative velocity at the contact point. The total contact force acting on the finite element can then be written as the sum of the normal and friction forces as $\mathbf{f}_c^{ik} = \mathbf{f}_n^{ik} + \mathbf{f}_f^{ik}$.

4.3.4 MBS Equations of Motion

The three-dimensional roll-drafting model developed in this chapter is implemented in a general flexible MBS algorithm designed for the analysis of interconnected rigid and flexible components. Each body may undergo arbitrary displacements including large rotations. Joint constraints and contact forces between the rollers and the filament bundle are introduced using the augmented Lagrangian formulation. The system equations of motion can be written as (Shabana, 2013)

$$\begin{bmatrix} \mathbf{M}_{rr} & \mathbf{0} & \mathbf{C}_{\mathbf{q}_r}^{\mathrm{T}} \\ \mathbf{0} & \mathbf{M}_{ee} & \mathbf{C}_{\mathbf{e}}^{\mathrm{T}} \\ \mathbf{C}_{\mathbf{q}_r} & \mathbf{C}_{\mathbf{e}} & \mathbf{0} \end{bmatrix} \begin{bmatrix} \ddot{\mathbf{q}}_r \\ \ddot{\mathbf{e}} \\ \boldsymbol{\lambda} \end{bmatrix} = \begin{bmatrix} \mathbf{Q}_r \\ \mathbf{Q}_{\mathbf{e}} \\ \mathbf{Q}_c \end{bmatrix} \tag{62}$$

where $\mathbf{M}_{rr}$ and $\mathbf{M}_{ee}$ are, respectively, the rigid body mass matrix and the constant ANCF mass matrix; $\mathbf{C}_{\mathbf{q}_r}$ is the constraint Jacobian matrix associated with the reference coordinates $\mathbf{q}_r$, $\mathbf{C}_{\mathbf{e}}$ is the constraint Jacobian matrix associated with absolute nodal coordinates $\mathbf{e}$, $\mathbf{C}_{\mathbf{q}_r}$ and $\mathbf{C}_{\mathbf{e}}$ account for the effect of the prescribed velocity and kinematic (joint) constraints; $\boldsymbol{\lambda}$ is the vector of Lagrange multipliers; $\mathbf{Q}_r$ and $\mathbf{Q}_e$ are the generalized force vectors associated with reference and absolute nodal coordinates; these vectors includes the contact forces as well as the hyper-elastic generalized forces, and $\mathbf{Q}_c$ is the quadratic velocity vector resulting from differentiation of the kinematic constraint equations twice with respect to time. The kinematic constraints in the model considered in this investigation include the revolute joint constraints, the prescribed roller angular velocities, and the forward velocity constraints on the first and last nodes. The augmented

form of the equations of motion can be solved for the vector of accelerations and Lagrange multipliers. The independent accelerations are integrated to determine the independent coordinates and velocities. The numerical solution used in this chapter ensures that the kinematic constraint equations are satisfied at the position, velocity, and acceleration levels.

4.4. Numerical Results

In this section, the PFB dynamic behavior in the textile machine during the roll-drafting process is examined. Several numerical examples are considered. A simple cantilever beam model is used first in order to check the implementation of the transversely isotropic material with the nonlinear isotropic neo-Hookean material models previously discussed in this chapter. The numerical results obtained using the textile set discussed in this chapter are then presented and analyzed. The arrangement of rollers and PFB for the initial configuration is depicted in Fig. 37. The roll-drafting process is simulated by using two different scenarios of roller and end node velocity constraints in order to ensure PFB stretch during the simulation.

4.4.1 Cantilever Beam Model

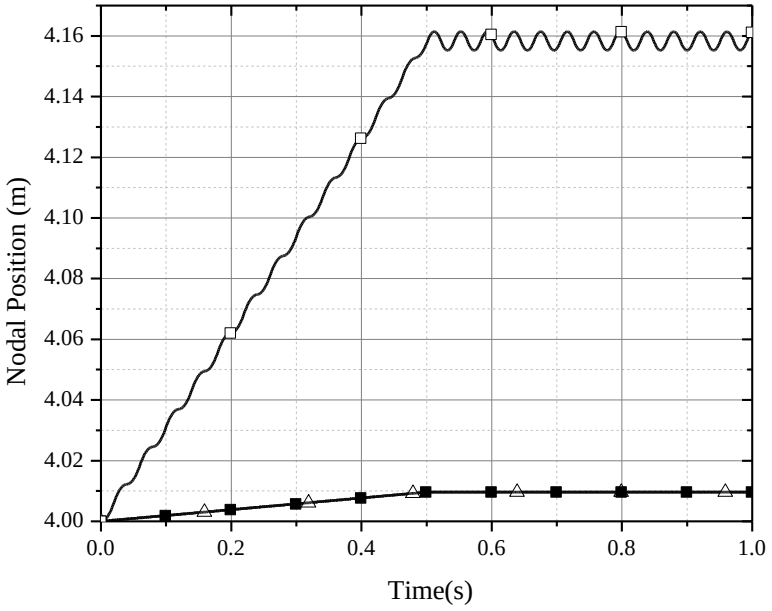

Figure 39. Nodal position in the *Y* direction (axial loading)
(—■— *a*, —△— *b*, —□— *c*)

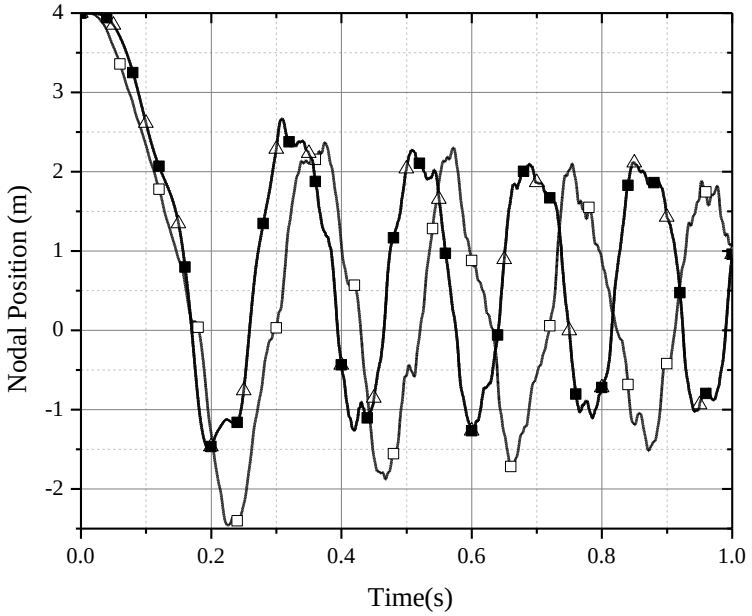

Figure 40. Nodal position in the *Y* direction (transverse load)
(—■— *a*, —△— *b*, —□— *c*)

Table 4. Cantilever beam model

	Density	Length× Width× Thickness	E_L (Pa)	E_T (Pa)	v_{TT}	v_{LT}	G_{TL} (Pa)
a	$100\,\mathrm{kg/m^3}$	0.4×0.04×0.04m	2.6×10^8		0.3		1×10^8
b	$100\,\mathrm{kg/m^3}$	0.4×0.04×0.04m	2.6×10^8	2.6×10^8	0.3	0.3	1×10^8
c	$100\,\mathrm{kg/m^3}$	0.4×0.04×0.04m	2.6×10^8	1.6×10^7	0.3	0.7	7.6×10^7

A simple cantilever beam model in the YZ plane is divided into 10 ANCF three-dimensional fully parameterized beam elements with properties shown in Table 4. There are three sets of element properties: (*a*) isotropic neo-Hookean material, (*b*) transversely isotropic material but with $E_L = E_T$ and $v_{TT} = v_{LT}$, and (*c*) transversely isotropic material with $E_L \neq E_T$ and $v_{TT} \neq v_{LT}$. Model b is used to obtain the fully isotropic model as a special case of the transversely isotropic model. This will allow for checking the new implementation of the transversely isotropic material model. In order to examine the axial deformation of this model, a force proportional to time is longitudinally applied at the end of the beam. To check the bending behavior, a time-variant force is applied at the end of the beam in the vertical direction. Figures 39-41 show the nodal displacement at the end of the beam along the two perpendicular axes. Figure 39 shows the response to the axial loading, whereas Figs. 40 and 41 show the response to the transverse loading. It can be observed that the results of the axial and bending deformations of models *a* and *b* agree well, demonstrating that the isotropic material is a special case of the transversely isotropic material when the longitudinal and transverse elastic coefficients and Poisson ratio are the same. It can also be concluded that, for model *c*, the new constitutive model leads to a different mechanical behavior as compared with the fully isotropic material. Good convergence of the new

constitutive model (model *c* in Tab. 4) can be observed from the results presented in Figs. 42-44. Figure 42 shows the *Y* displacements due to an axial load, whereas Figs. 43 and 44 show the nodal displacement at the end of the beam along the *Y* and *Z* directions, respectively. These results demonstrate that the fully parameterized ANCF beam element, with the newly proposed constitutive model, has good convergence characteristics even in the case of large deformations.

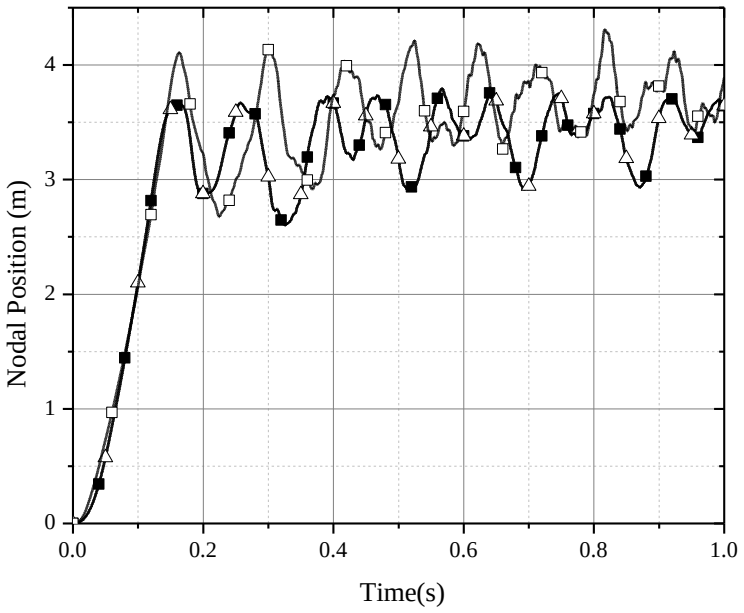

Figure 41. Nodal position in the *Z* direction (transverse load)
(—■— *a*, —△— *b*, —□— and *c*)

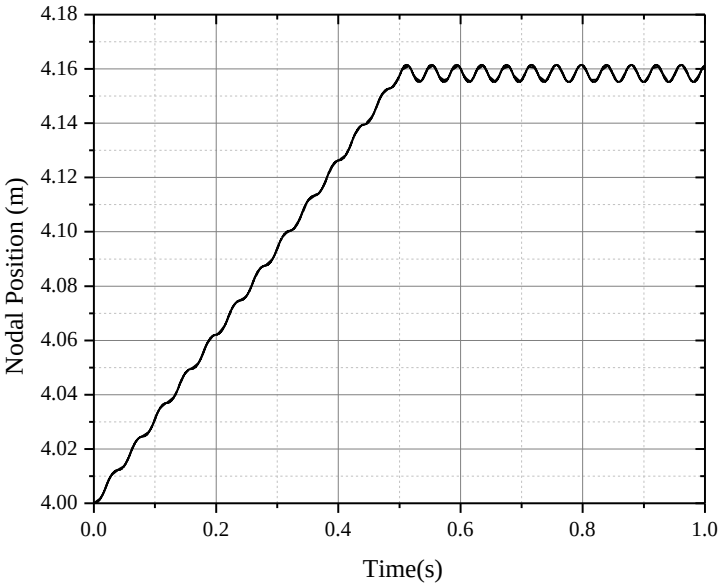

(*a*) Original plot

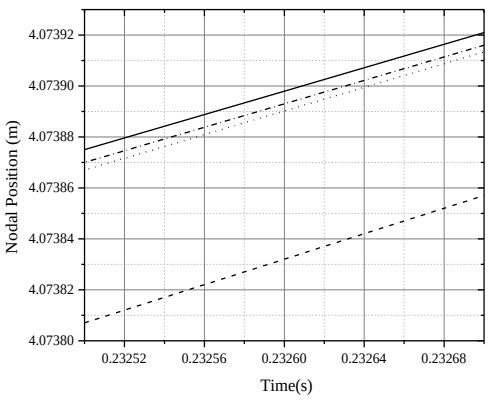

(*b*) Enlarged plot #1

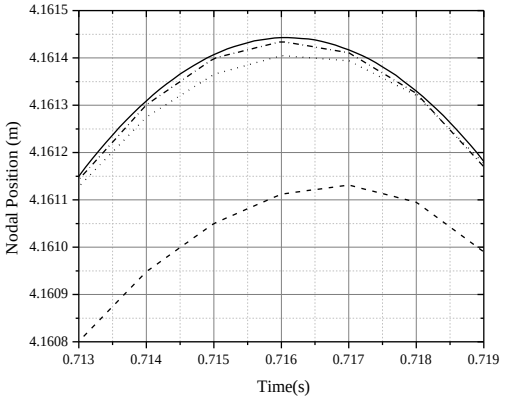

(*c*) Enlarged plot #2

Figure 42. Nodal Position in the *Y* direction (axial loading)
(------ 10-element, ... 20-element, _._._ 40-element, ——— 80-element)

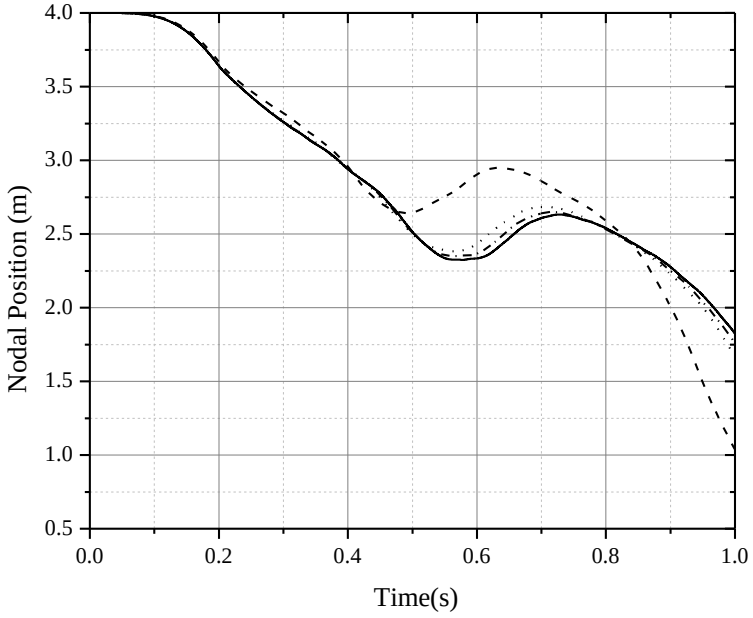

Figure 43. Nodal position in the *Y* direction (transverse load)
(------ 10-element, ... 20-element, _.-._.- 40-element, ——— 80-element)

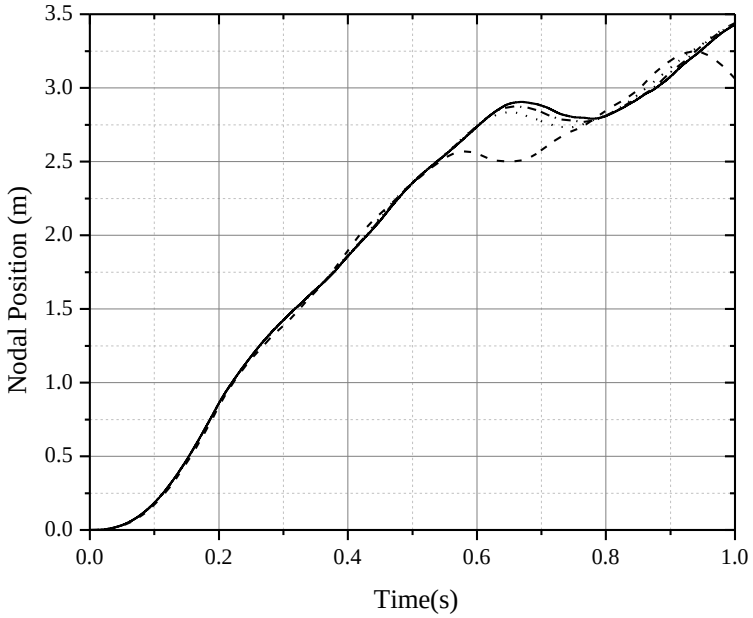

Figure 44. Nodal position in the *Z* direction (transverse load)
(------ 10-element, ... 20-element, _.-._.- 40-element, ——— 80-element)

4.4.2 Roll-Drafting MBS Model

The roll-drafting MBS model is investigated in this subsection. Results, such as the elongation ratio, the shrinkage of the cross section, the axial strain distribution, the nodal contact forces, and the nodal relative velocity can be obtained. In this section, various machine operating conditions are examined by specifying different velocity constraints of the rollers and nodes, which lead to a range of PFB dynamic deformation states.

Elongation ratio In this chapter, two sets of velocity constraints are investigated and compared (see Figs. 35 and 36). By examining the initial configuration of the system and the configuration at the end of the simulation, one can obtain the position of the first node and last node, as shown in Figs. 45a and b for the first and second cases, respectively. Using the position of the nodes, one can determine an approximate value for the change of total length of the filament bundle. Therefore, the elongation ratio of the filament bundle can be calculated as $\alpha = \left(\left(l_t - l_0 \right) / l_0 \right) \times 100 \ (\%)$, where α is the elongation ratio, l_0 is the initial length of the filament bundle, and l_t is the current length of the bundle. For the first case, at $t = 3\text{s}$, $\alpha_1 = \left(12.26 - 10.16 \right) / 10.16 = 20.67\%$, while for the second case $\alpha_2 = \left(13.31 - 10.16 \right) / 10.16 = 31.0\%$. Since the input and output velocity for the first case are 2m/s and 3m/s, respectively, as the PFB is drafted, the final velocity ratio will reach 150%. For the second case, with an input velocity of 1.5m/s, the final ratio will be 200%.

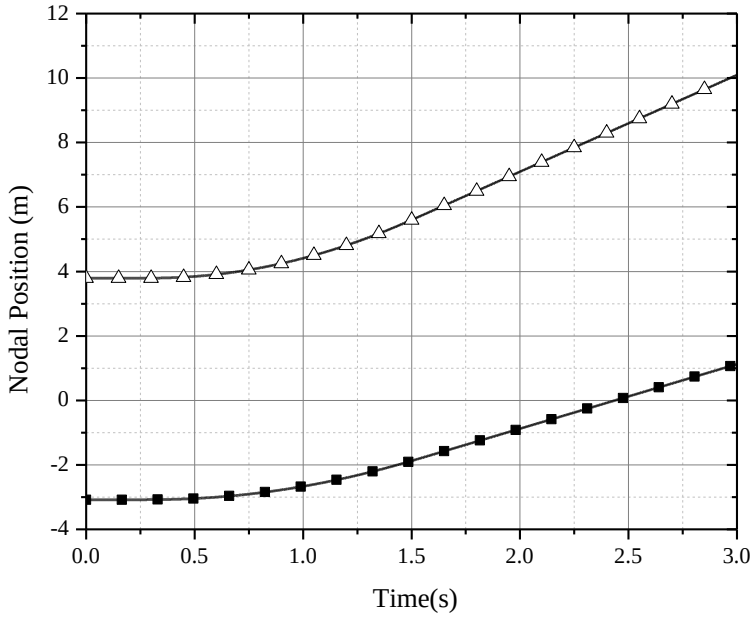

(*a*) First scenario

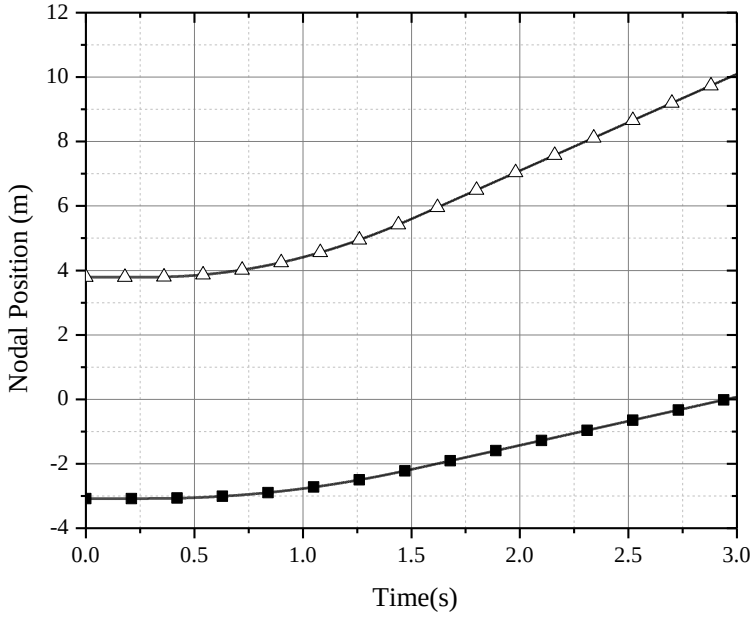

(*b*) Second scenario

Figure 45. Nodal position of the first and last node in the *Y* direction (—■—Node # 1, and —△— Node # 128)

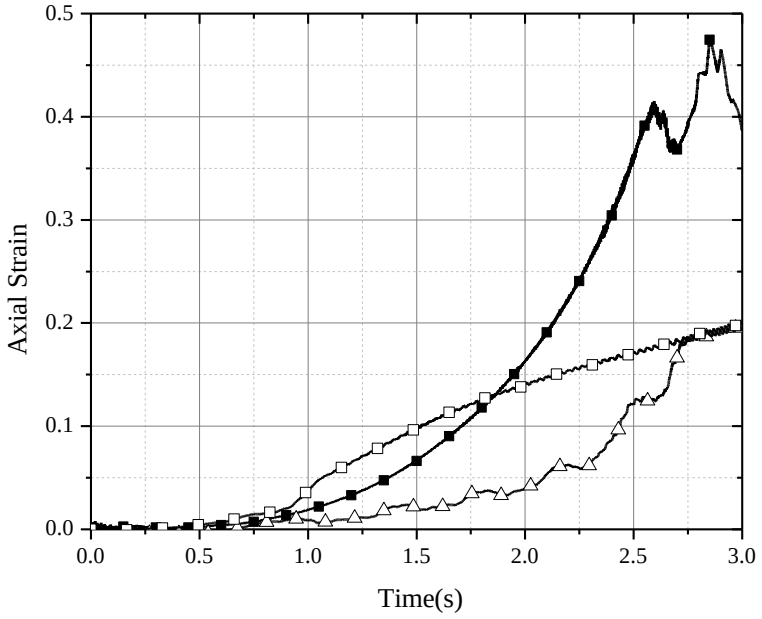

(*a*) First scenario

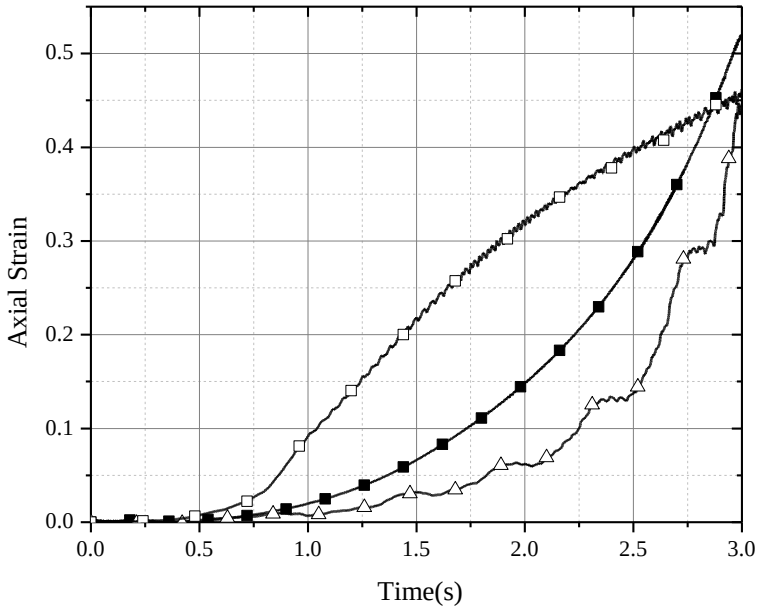

(*b*) Second scenario

Figure 46. Axial strain for several ANCF elements
(—■—Element # 10, —△— Element # 70 and —□— Element # 120)

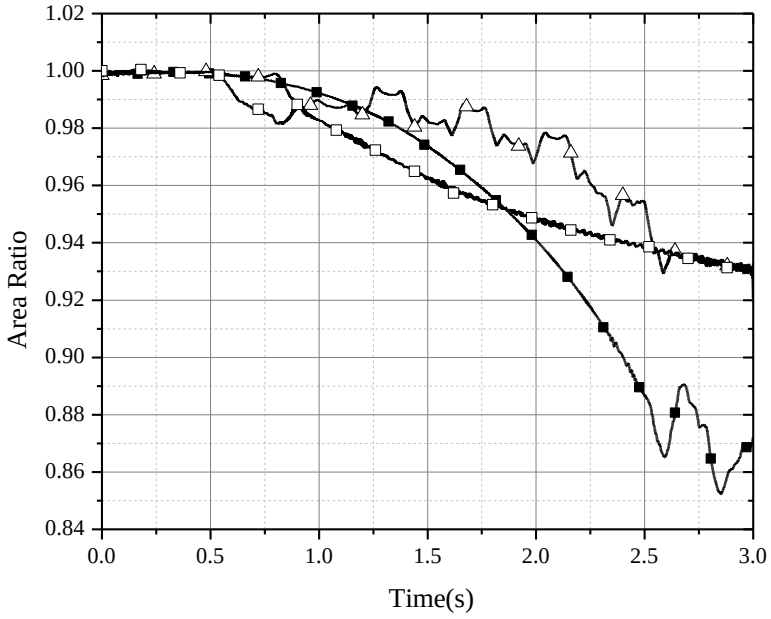

(*a*) First scenario

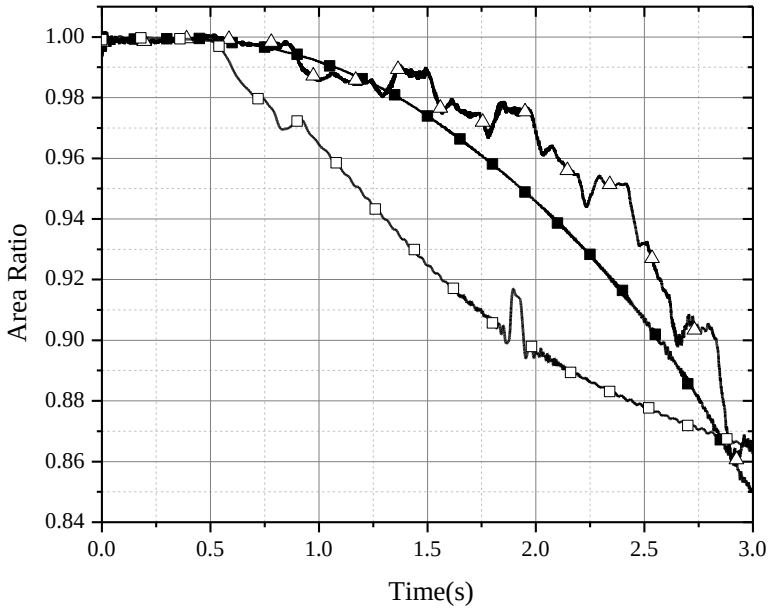

(*b*) Second scenario

Figure 47. Cross-section area ratio for several ANCF elements
(—■—Element # 10, —△— Element # 70 and —□— Element # 120)

Axial strain and cross-section deformation The use of the ANCF fully parameterized elements allow to obtain the Green-Lagrangian strains at an arbitrary point in the textile material during the drawing process in a straightforward manner. The strain results can help in understanding the influence of several PFB simulation parameters. Figures 46a and b show the axial strain results for different elements obtained using the two simulation scenarios. Figure 46b shows that the element 70 and element 120 experience strains larger than those in Fig. 46a. This is due to the fact that, for the second set of rollers, the velocity constraints lead to a larger elongation ratio over time. The same trend may be observed in Fig. 47, which shows the change of the cross-section area for the same finite elements. The shrinkage of the cross section area for the second case is larger than that of the first case; this behavior is consistent with the time evolution of the axial strain shown in Fig. 46. The deformation state of the entire textile fiber can be plotted at different time steps in order to analyze the regions of strain concentration. The axial strain distribution for the two sets of rollers at two different time steps is displayed in Fig. 48. From the strain distribution results in Fig. 48, it can be seen that, at the same instant of time, the output point in the second case undergoes larger elongation as compared to the first case. Moreover, the strains in the elements in contact with the rollers are smaller than those when there is no contact with the rollers, which indicates that the elongation is occurring mainly on the input and output points.

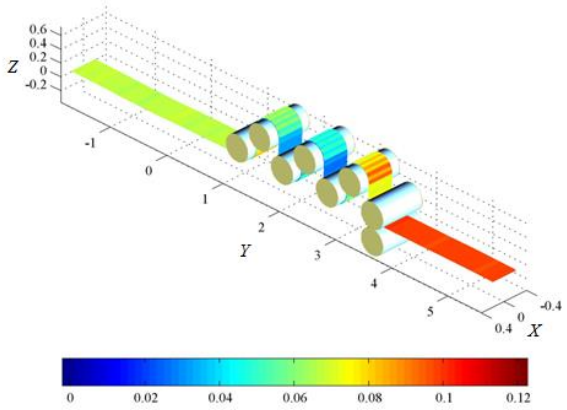

(*a*) At $t = 1.5s$, first scenario

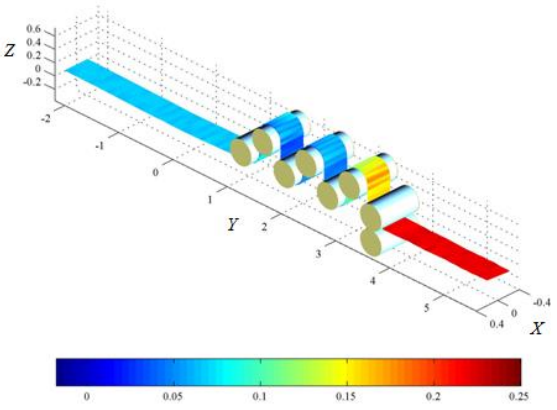

(*b*) At $t = 1.5s$, second scenario

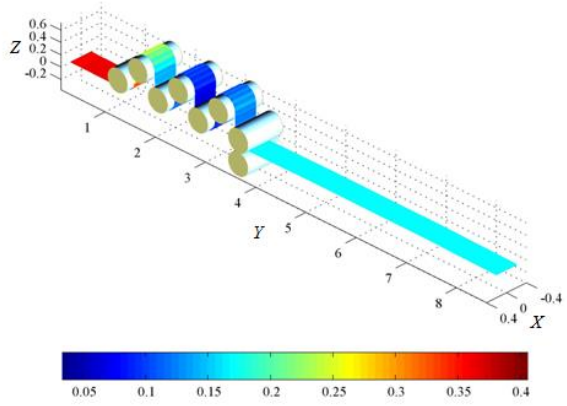

(*c*) At $t = 2.5s$, first scenario

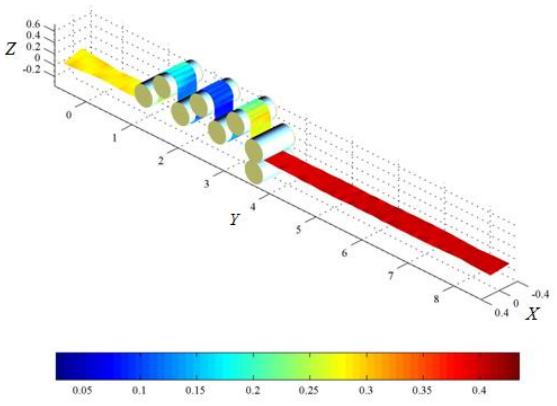

(*d*) At $t = 2.5s$, second scenario

Figure 48 Axial Green-Lagrange strain distribution in the filament bundle at two time steps

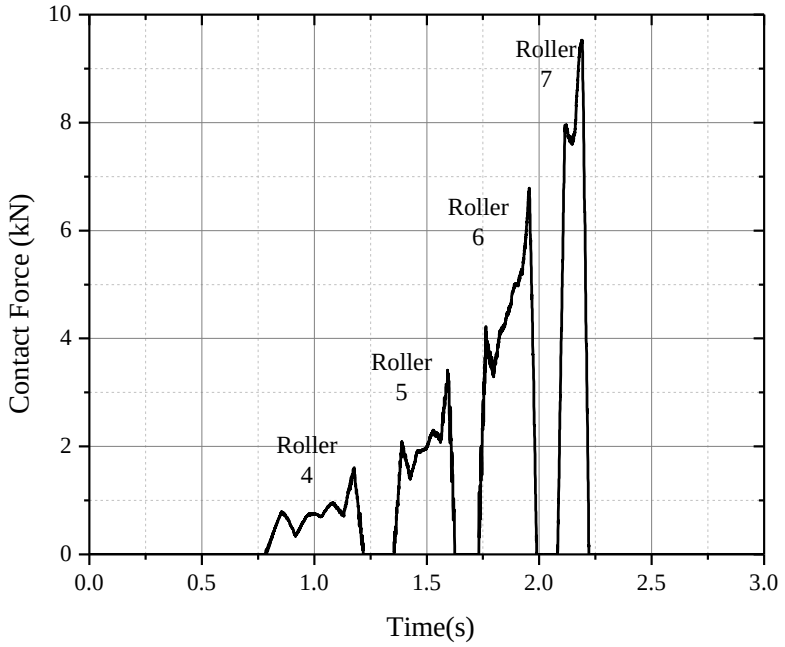

(*a*) First scenario

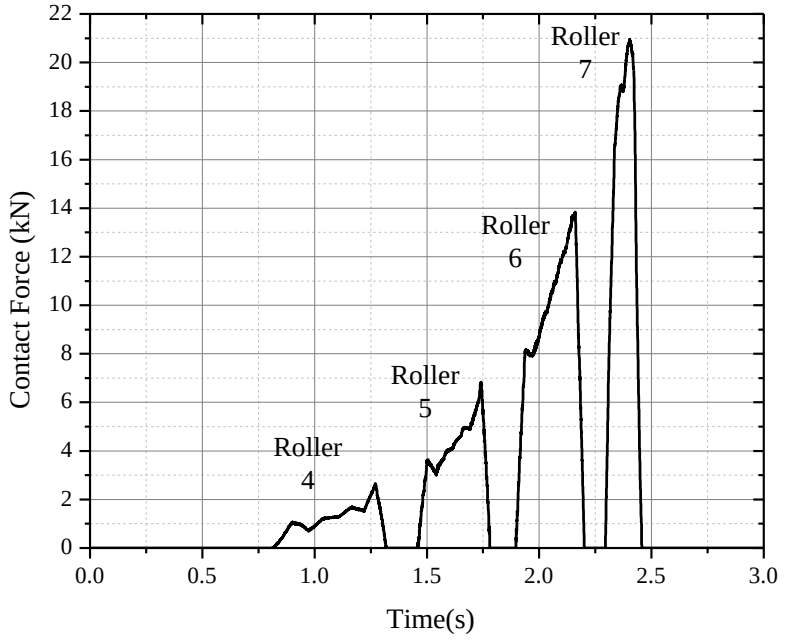

(*b*) Second scenario

Figure 49. Contact force at node # 83 (number of roller in contact is indicated in the plot)

Contact forces and relative velocity The flexible MBS model allows for easily extracting system information. For example, the time history of the contact forces can be obtained to examine the roller reaction forces as a function of the angular velocity. Figures 49a and b show the contact forces associated with node 83, which is located initially between the third and the fourth roller. The results of Figs. 49a and b show that the contact forces range from zero to peak values. This behavior is expected and is attributed to engagements and disengagements with various rollers. Between rollers, the contact force falls to zero, whereas when there is contact with a roller, increasing the forward velocity produces a rapid increase in the value of the total force, as seen in Fig. 49. Figures 50a and b show the forward velocity of node 83 when it is in contact with rollers. The velocity of the fiber (solid line) as well as the velocity of the rollers (dashed line) can be seen. For the first set of rollers, it may be observed that there is a negligible relative velocity between the filament bundle and the rollers 4 and 5. However, due to the fact that the output velocity is larger than the velocity of the rollers, there is a relative velocity between the filament bundle and the rollers. Nonetheless, for the second set of rollers, the difference between the velocity at the output point and rollers is larger, and the relative velocity is only small on roller 4, where the PFB velocity is close to the velocity of rollers. The relative velocity oscillations shown in Fig. 50 are due to the hyper-elastic material behavior. This phenomenon may be mostly attributed to the elastic deformation in the axial direction, which leads to cross section shrinkage.

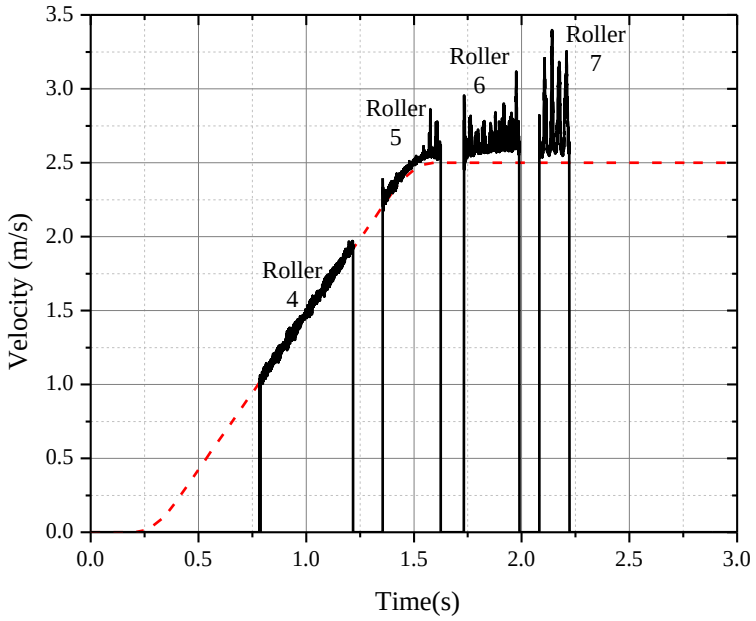

(a) First scenario

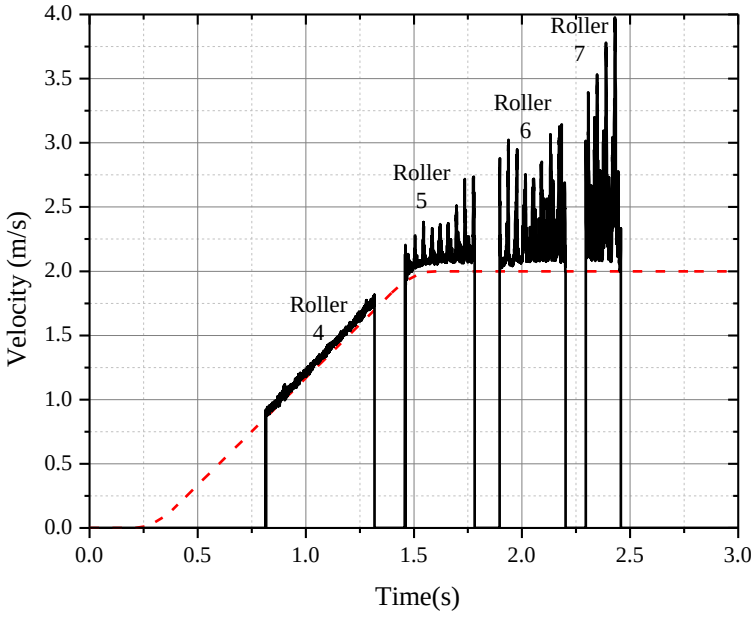

(*b*) Second scenario

Figure 50. Forward velocity of node #83 (number of roller in contact is indicated in the plot) (— nodal velocity, --- line velocity of rollers)

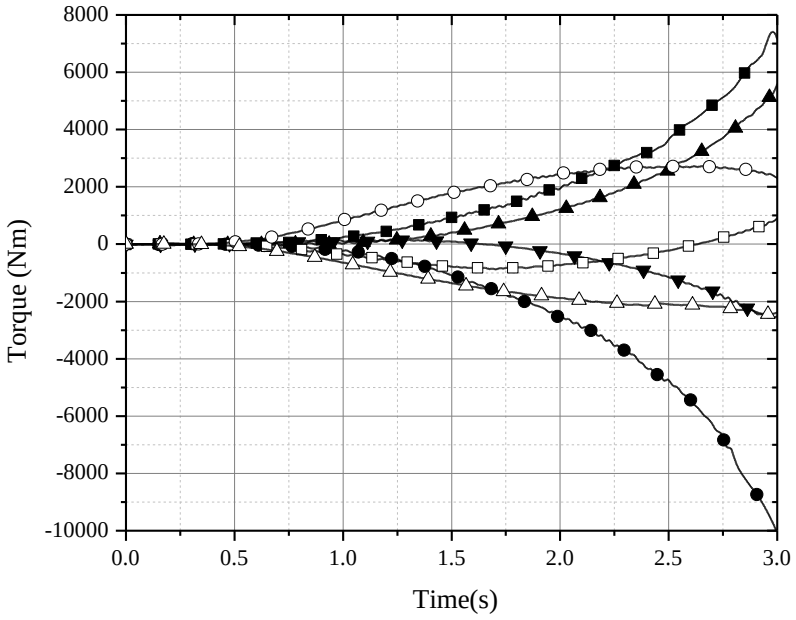

Figure 51. The torques on each roller

(1, 2, 3, 4, 5, 6, 7)

Torques on the rollers By using Lagrange multipliers and the Jacobian matrix of the algebraic constraint equations, the torque applied to each roller can be obtained as shown in Fig. 51. The results presented in this figure show the torques that need to be produced by the motors to drive the roll-drafting machine. It can be seen from the results of this figure that the first three rollers must be provided with higher torque. This is consistent with the strains shown in Fig. 47, where the elements closer to the first rollers have larger deformation. It is also important to point out that this initial study of this new MBS application is mainly focused on the transient effect at the beginning of the roll-drafting process with the objective of demonstrating the use of ANCF finite elements in developing new MBS textile models. The study of the complete process and reaching the steady state requires the use of much longer yarn that will require more array space and more

computational efforts and time. This important issue will be addressed in future investigations by the authors.

4.5 Concluding Remarks

In this chapter, a transversely isotropic hyper-elastic constitutive law is employed to develop a new MBS computational approach for the virtual prototyping of textile systems. The work presented in this chapter can be considered as a first step in developing detailed MBS textile models. The strain energy for transversely isotropic materials is decomposed into a fully isotropic component and an orthotropic, transversely isotropic component expressed in terms of five invariants of the right Cauchy-Green deformation tensor. Using this energy decomposition, the second Piola-Kirchhoff stress tensor and the tensor of the elastic coefficients are split into isotropic and transversely isotropic parts. The strain energy equations are generalized to the fully nonlinear regime by using the neo-Hookean potential to describe the isotropic component, while the orthotropic, transversely isotropic part follows the strain density function defined by Bonet and Burton (1997). The total strain energy function is written in terms of five strain invariants and the resulting constitutive equations are expressed in terms of five independent elastic coefficients. Different Poisson ratios are used in order to capture the coupling between deformation modes in different directions. The roll-drafting process is simulated by imposing boundary velocity constraints in order to reproduce the effects of PFB/roller interactions and the motors in the textile machine. ANCF finite elements are used for to develop a new PFB model. The use of hyper-elastic materials and ANCF kinematics avoids deformation singularity problems encountered when linear

constitutive laws are employed. The results obtained in this investigation show that the PFB model can capture translation and rotation, large strains, and the shrinkage of the cross section during the drawing process. The contact information during the drawing process can be extracted to assess slippage between fiber and rollers. The model used in this chapter demonstrates the effectiveness of using ANCF finite elements and MBS algorithms for the analysis of textile machinery.

There are, however, several phenomena that need to be addressed in future investigations in order to enhance the simulation capabilities, capture more details, and improve the textile models. For example, plastic effects can be included in the PFB constitutive equations; the thermal effects of hot water tanks can be accounted for by space-dependent parameters, such as Young modulus, and surface-to-surface contact can also be included in future studies. Consideration of these effects will improve the accuracy of the model and will be considered for future investigations by the authors. Another important issue is the study of the complete roll-draft process. As previously mentioned, this initial study of this new MBS application is mainly focused on the transient effect at the beginning of the roll-drafting process with the goal of demonstrating that ANCF finite elements can be effectively used in developing new models of these systems and capturing the deformation of the yarn cross section. The study of the complete process and reaching the steady state requires the use of much longer yarn that will require more array space and more computational efforts and time. This important issue will be addressed in future investigations by the authors.

CHAPTER 5

CONCLUSIONS

In this thesis, a low order three-dimensional liquid sloshing model based on the FFR formulation is proposed. This liquid sloshing model can capture the free surface motion and the distributed inertia of the fluid. Using a total Lagrangian approach and the FFR formulation, the liquid sloshing model was successfully integrated with MBS algorithms and used to study the effect of the sloshing on the dynamics of railroad vehicles. The FE method and modal analysis techniques are used to develop a reduced order fluid body model. The results presented in this thesis shows that liquid sloshing can have a significant effect on the contact forces and the dynamics of the vehicle. This was demonstrated using a three-dimensional wheel/rail contact model that allows for accurate description of the wheel and rail profiles. The results presented in this thesis showed that the wheels that carry the highest loads in the fluid body and rigid body models can be different. The results also show that liquid sloshing tends to increase the possibility of wheel/rail separation.

While the liquid sloshing approach proposed in this thesis defines a low order model, it has several clear advantages compared with existing models. It is a more realistic model as compared with the discrete inertia models that employ pendulum systems and used in the area of vehicle dynamics, it allows capturing the effect of the fluid body distributed inertia, it allows studying the contribution of each mode of the fluid displacement on the vehicle dynamics and identifying the modes that are the cause of accidents, and it can be systematically integrated into the computational algorithms implemented in most commercial MBS computer programs. As previously mentioned in this thesis, the goal is not to study the effect of the vehicle motion on the fluid, rather the goal is to study the effect of the distributed inertia of the fluid on the vehicle dynamics.

And a total Lagrangian ANCF finite element approach is proposed for liquid sloshing problems. The ANCF fluid elements allow for successful integration of fluid and MBS algorithms. Using the total Lagrangian approach, the fluid boundary conditions can be systematically introduced. The proposed ANCF brick elements have a constant inertia matrix, ensure the gradient continuity at the element nodes, and do not impose any restriction on the amount of rotation or deformation within the elements. The feasibility of implementing these fluid elements was demonstrated using several simple examples. The results show that complex fluid geometry can be obtained using one ANCF finite element. The results also show that in some simulation scenarios more realistic geometry can be obtained by increasing the degree of continuity at the IPAE interface. Furthermore, more complex geometry can be captured by using ANCF meshes with more finite elements, allowing for future investigations of more complex fluid problems using a total Lagrangian approach. The future work will focus on integrating this fluid model with vehicle or any flexible or rigid multibody system to study the interaction between the solid and liquid.

In this thesis, a transversely isotropic hyper-elastic constitutive law is employed to develop a new MBS computational approach for the virtual prototyping of textile systems. The work presented in this thesis can be considered as a first step in developing detailed MBS textile models. The strain energy for transversely isotropic materials is decomposed into a fully isotropic component and an orthotropic, transversely isotropic component expressed in terms of five invariants of the right Cauchy-Green deformation tensor. Using this energy decomposition, the second Piola-Kirchhoff stress tensor and the tensor of the elastic coefficients are split into isotropic

and transversely isotropic parts. The strain energy equations are generalized to the fully nonlinear regime by using the neo-Hookean potential to describe the isotropic component, while the orthotropic, transversely isotropic part follows the strain density function defined by Bonet and Burton (1997). The total strain energy function is written in terms of five strain invariants and the resulting constitutive equations are expressed in terms of five independent elastic coefficients. Different Poisson ratios are used in order to capture the coupling between deformation modes in different directions. The roll-drafting process is simulated by imposing boundary velocity constraints in order to reproduce the effects of PFB/roller interactions and the motors in the textile machine. ANCF finite elements are used for to develop a new PFB model. The use of hyper-elastic materials and ANCF kinematics avoids deformation singularity problems encountered when linear constitutive laws are employed. The results obtained in this thesis show that the PFB model can capture translation and rotation, large strains, and the shrinkage of the cross section during the drawing process. The contact information during the drawing process can be extracted to assess slippage between fiber and rollers. The model used in this thesis demonstrates the effectiveness of using ANCF finite elements and MBS algorithms for the analysis of textile machinery.

There are, however, several phenomena that need to be addressed in future investigations so as to enhance the simulation capabilities, capture more details, and improve the textile models. For example, plastic effects can be included in the PFB constitutive equations; the thermal effects of hot water tanks can be accounted for by space-dependent parameters, such as Young's modulus, and surface-to-surface contact can also be included in future studies. Consideration of these effects will improve the accuracy of the model and will be considered for future investigations by the

authors. Another important issue is the study of the complete roll-draft process. As previously mentioned, this initial study of this new MBS application is mainly focused on the transient effect at the beginning of the roll-drafting process with the goal of demonstrating that ANCF finite elements can be effectively used in developing new models of these systems and capturing the deformation of the yarn cross section. The study of the complete process and reaching the steady state requires the use of much longer yarn that will require more array space and more computational efforts and time. This important issue will be addressed in future investigations by the authors.

APPENDIX A

On Tue, Feb 23, 2016 at 3:13 PM, Beth Darchi <DarchiB@asme.org> wrote:

Dear Mr. Wang:

It is our pleasure to grant you permission to use the following ASME materials:

- ANCF Analysis of Textile Systems, by Liang Wang; Yongxing Wang; Antonio M. Recuero; Ahmed A. Shabana, J. Comput. Nonlinear Dynam. 2015; 11(3)
- Low Order Continuum-Based Liquid Sloshing Formulation for Vehicle System Dynamics, by Liang Wang; Jesús R. Jiménez Octavio; Cheng Wei; Ahmed A. Shabana, J. Comput. Nonlinear Dynam. 2015; 10(2)
- A Total Lagrangian ANCF Liquid Sloshing Approach for Multibody System Applications, by Cheng Wei; Liang Wang; Ahmed A. Shabana, J. Comput. Nonlinear Dynam. 2015; 10(5)

cited in your letter for inclusion in an PhD Thesis entitled Integration of Different Constitutive Models in Multibody System Algorithms to be published by University of Illinois at Chicago Library.

Permission is granted for the specific use as stated herein and does not permit further use of the materials without proper authorization. Proper attribution must be made to the author(s) of the materials. **Please note**: if any or all of the figures and/or Tables are of another source, permission should be granted from that outside source or include the reference of the original source. ASME does not grant permission for outside source material that may be referenced in the ASME works.

As is customary, we request that you ensure full acknowledgment of this material, the author(s), source and ASME as original publisher. Acknowledgment must be retained on all pages printed and distributed.

Many thanks for your interest in ASME publications.

Sincerely,

Beth Darchi
Publishing Administrator
ASME
2 Park Avenue, 6th Floor
New York, NY 10016-5990
Tel 1.212.591.7700
darchib@asme.org

CITED LITERATURES

1. Aboubakr, A.K., and Shabana, A.A., 2015, “Efficient and robust implementation of the TLISMNI method”, Journal of Sound and Vibration. Vol. 353, pp. 220-242.

2. Abramson, H.N., 1966, “The Dynamic Behaviour of Liquids in Moving Containers”, NASA SP-106.

3. Aliabadi. S., Johnson. A., and Abedi. J., 2003, "Comparison of Finite Element and Pendulum Models for Simulation of Sloshing". Computers and Fluids. Vol. 32, pp. 535-545

4. Anderson, J. D., 1995, Computational Fluid Dynamics: the Basics with Applications, McGraw-Hill, New York City, New York.

5. Bauer, H.F., 1960, “Mechanical Model for the Description of the Liquid Motion in a Rectangular Container”, Lockheed-Co, RN ER-8559 (June).

6. Bechtel, S. E., Vohra, S. and Jacob, K. I., 2002, “Stretching and Slipping of Fibers in Isothermal Draw Processes”, Textile Research Journal, Vol. 72, pp. 769-776.

7. Bonet, J., and Burton, A. J., 1997, “A Simple Orthotropic, Transversely Isotropic Hyperelastic Constitutive Equations for Large Strain Computations”, Comput. Methods Appl. Mech. Engrg. Vol. 162. pp. 151-164.

8. Bonet, J., and Wood, R.D., 1997, Nonlinear Continuum Mechanics for Finite Element Analysis, Cambridge University Press, Cambridge.

9. Cai, Z., and Gutowski, T., 1992. “The 3-D Deformation Behavior of a Lubricated Fiber Bundle”, *Journal of Composite Materials*, Vol. 26, pp. 1207-1237.

10. Celebi. M. S., Akyildiz. H., 2001, "Nonlinear modeling of liquid sloshing in a moving rectangular tank". Ocean Engineering. Vol. 29, pp. 1527-1553.

11. Christensen, R. M., 1979, *Mechanics of Composite Materials*, John Wiley & Sons.

12. Curiskis, J.I., and Carnaby, G.A., 1985, “Continuum Mechanics of the Fiber Bundle”, *Textile Research Journal*, Vol. 55, pp. 334-344.

13. Djaja, R. G., Moss, P. J., Carnaby, G. A., and Lee, D. H., 1992, “Finite Element Modeling of an Oriented Assembly of Continuous Fibers”, *Textile Research Journal*, Vol. 62, pp. 445-457.

14. Dodge, F.T., and Kana, D.D., 1966, “Moment of Inertia and Damping of Liquid in Baffled Cylindrical Tanks”, *Journal of Spacecraft Rockets,* Vol. 3(1), pp. 153-155.

15. Dufva, K., Kerkkänen, K., Maqueda, L. G., Shabana, A.A., 2007, “Nonlinear Dynamics of Three-dimensional Belt Drives Using the Finite-element Method”, *Nonlinear Dynamics*, Vol. 48, pp. 449-466.

16. Dyke, P.V., and Hedgepeth, J.M., 1969, “Stress Concentrations from Single-Filament Failures in Composite Materials”, *Textile Research Journal*, Vol. 39, pp. 618-626.

17. Gialleonardo, E. D., Premoli, A., Gallazzi, S., Bruni, S., 2013, “Sloshing Effects and Running Safety in Railway Freight Vehicles”, *Vehicle System Dynamics*, 51:10, pp. 1640-1654.

18. Gingold, R. A., and Monaghan, J. J., 1977, "Smoothed Particle Hydrodynamics: Theory and Application to Non-Spherical Stars", *Monthly Notices of the Royal Astronomical Society*, Vol. 181(2), pp. 375-389.

19. Graham, E.W., 1951, “The Forces Produced by Fuel Oscillations in a Rectangular Tank”, *Douglas Aircraft Cooperation*, SM-13748.

20. Graham, E.W., and Rodríguez, A.M. 1952, “The Characteristics of Fuel Motion Which Affect Airplane Dynamics”, *Journal of Applied Mechanics*, 74, pp. 381-388.

21. http://www.cbsnews.com/8301-202_162-57593058/canada-train-derailments-number-of-missing-rises-to-60/

22. Huh, Y., and Kim, J.S., 2004, “Modeling the Dynamic Behavior of the Fiber Bundle in a Roll-Drafting Process”, *Textile Research Journal*, Vol. 74, pp. 872-878.

23. Huh, Y., and Kim, J.S., 2006, “Effects of Material Parameters and Process Conditions on the Roll-Drafting Dynamics”, *Fibers and Polymers*, Vol. 7(4), pp. 424-431.

24. Ibrahim, R.A., Pilipchuk, V.N. and Ikeda, T., 2001, “Recent Advances in Liquid Sloshing Dynamics”, *Applied Mechanics Reviews,* 54(2), pp. 133-199.

25. Ibrahim, R.A., 2005, *Liquid Sloshing Dynamics: Theory and Applications*, Cambridge University Press.

26. Idelsohn, S. R., Onate, E., Pin, F. D., and Calvo, N., 2006, "Fluid-structure Interaction Using the Particle Finite Element Method", *Computer Methods in Applied Mechanics and Engineering*, Vol. 195(17-18), pp. 2100-2123.

27. Iwnicki, S., 2006, *Handbook of Railway Vehicle Dynamics*, CRC Press.

28. Jones, N., 1974, "Elastic-Plastic and Viscoelastic Behavior of a Continuous Filament Yarn", *Int. J. Mech. Sci.*, Vol. 16, pp. 679-687.

29. Jung, J. H., and Kang, T. J., 2005, "Large Deflection Analysis of Fibers with Nonlinear Elastic Properties", *Textile Research Journal*, Vol. 75, pp. 715-723.

30. Kana, D. D., 1987, "A Model for Nonlinear Rotary Slosh in Propellant Tanks", *Journal of Spacecraft Rockets*, 24(3,4), pp. 169-177.

31. Kana, D. D., 1989, "Validated Spherical Pendulum Model for Rotary Liquid Slosh", *Journal of Spacecraft Rockets*, 26(3), pp. 188-195.

32. Kao, P.H., Lammers, S.R., Hunter, K., Stenmark, K.R., Shandas, R., and Qi, H.J., 2010, "Constitutive Modeling of Anisotropic Finite-Deformation Hyperelastic Behaviors of Soft Materials Reinforced by Tortuous Fibers", *International Journal of Structural Changes in Solids- Mechanics and Applications*, Vol. 2(1), pp. 19-29.

33. Karbhari, V.M., Simacek, P., 1996, "Notes on the Modeling of Preform Compaction: I-Micromechanics at the Fiber Bundle Level", *Journal of Reinforced Plastics and Composites*. Vol. 15, pp. 86-122.

34. Kim, J. S., Cherif, C., and Huh, Y., 2008, "Numerical Analysis of Fiber Fleece Behavior in Roller Drafting in a Transient State", *Textile Research Journal*, Vol. 78, pp. 796-805.

35. King, C. and Trichur, R., 2015, "Train Carrying Crude Oil Derails in Ontario", *The Wall Street Journal*, http://www.wsj.com/articles/train-carrying-crude-oil-derails-in-ontario-1424015961

36. Kulkarni, S.G., Gao, X., Horner, S.E., Mortlock, R. F., Zheng, J.Q., 2014, "A Transversely Isotropic Visco-hyperelastic Constitutive Model for Soft Tissues", Mathematics and Mechanics of Solids, (In Press), DOI: 10.1177/1081286514536921

37. Limbert, G. and Middleton. J., 2004, "A Transversely Isotropic Viscohyperelastic Material Application to the Modeling of Biological Soft Connective Tissues", *International Journal of Solid and Structures*, Vol. 41, pp4237-4260.

38. Liu, M. B., and Liu, G. R., 2010, "Smoothed Particle Hydrodynamics (SPH): an Overview and Recent Developments", *Archives of Computational Methods in Engineering*, Vol. 17(1), pp. 25-76.

39. Maqueda, L. G., and Shabana, A. A., 2007, "Poisson Modes and General Nonlinear Constitutive Models in the Large Displacement Analysis of Beams", *Multibody System Dynamics*, Vol. 18, pp. 375-396.

40. Mbarek, S., Jaziri, M., Carrot, C., and Chalamet, Y., 2012, “Thermo Mechanical Properties of a Polymer Blend: Investigation of a Third Phase”, *Mechanics of Materials*, Vol. 52, pp. 78-86.

41. McLaughlin, P.V. Jr., 1972, “Plastic Limit Behavior and Failure of Filament Reinforced Materials”, *Int. J. Solids Structures*, Vol. 8, pp. 1299-1318.

42. McIvor, P., 1989, “Sloshing Frequencies for Cylindrical and Spherical Containers Filled to an Arbitrary Depth”, *Journal of Fluid Mechanics*, 201, pp. 243-257.

43. Negrut, D., Tasora, A., Mazhar, H., Heyn, T., and Hahn, P., 2012, "Leveraging Parallel Computing in Multibody Dynamics", *Multibody System Dynamics*, Vol. 27(1), 95-117.

44. Ogden, R. W., 1984, *Non-linear Elastic Deformations*, Dovers Publications, Mineola, New York.

45. Olshevskiy, A., Dmitrochenko, O. and Kim, C.W., 2013, “Three-Dimensional Solid Brick Element Using Slopes in the Absolute Nodal Coordinate Formulation”, *ASME Journal of Computational and Nonlinear Dynamics*, Vol. 9(2), 021001, (10 pages), doi:10.1115/1.4024910.

46. Pan, N., Carnaby, G.A., 1989, “Theory of the Shear Deformation of Fibrous Assemblies”, *Textile Research Journal*, Vol. 59, pp. 285-292.

47. Pan, N., 1992, “Development of a Constitutive Theory for Short Fiber Yarns: Mechanics of Staple Yarn Without Slippage Effect”, *Textile Research Journal*, Vol. 62, pp. 749-765.

48. Pin, F. D., Idelsohn, S., Oñate, E., and Aubry, R., 2007, "The ALE/Lagrangian Particle Finite Element Method: A New Approach to Computation of Free-surface Flows and Fluid-object Interactions", *Computers and Fluid*, Vol. 36(1), pp. 27-38.

49. Pinson, L.D., 1964, “Longitudinal Spring Constants for Liquid Propellant Tanks with Ellipsoidal Tanks”, NASA TN D-2220 (November).

50. Platt, M.M., Klein, W.G., and Hamburger, W.J., 1958, “Mechanics of Elastic Performance of Textile Materials: Part XIII： Torque Development in Yarn System: Singles Yarn”, *Textile Research Journal*, Vol. 28, pp. 1-14.

51. Platt, M.M., Klein, W.G., and Hamburger, W.J., 1959, “Mechanics of Elastic Performance of Textile Materials: Part XIV： Some Aspects of Bending Rigidity of Singles Yarns”, *Textile Research Journal*, Vol. 29, pp. 611-627.

52. Ranganathan, R., Rakheja, S. and Sankar, S., 1989, “Steady Turning Stability of Partially Filled Tank Vehicles with Arbitrary Tank Geometry”, *Journal of Dynamic Systems, Measurement, and Control* , 111, pp. 481–489.

53. Rebouillat, S. and Liksonov, D., 2010, “Fluid-structure Interaction in Partially Filled Liquid Containers: A Comparative Review of Numerical Approaches”, *Computers and Fluids*, 39(5), pp. 739-746.

54. Reddy, J. N., and Gartling, D.K., 2010, *The Finite Element Method in Heat Transfer and Fluid Dynamics*, Taylor & Francis/CRC.

55. Shabana, A. A., 1997, “Flexible Multibody Dynamics: Review of Past and Recent Developments”, *Multibody System Dynamics*, Vol. 1, pp. 189-222.

56. Shabana, A. A., 1998, "Computer Implementation of the Absolute Nodal Coordinate Formulation for Flexible Multibody Dynamics", *Nonlinear Dynamics*, Vol. 16, pp. 293-306.

57. Shabana, A.A., Zaazaa, K.E., and Sugiyama, H., 2008, *Railroad vehicle dynamics: a computational approach*, Taylor & Francis/CRC.

58. Shabana, A. A., and Yakoub, R.Y., 2001, “Three Dimension Absolute Nodal Coordinate Formulation for Beam Elements: Theory”, *ASME J. Mech. Des*, Vol. 123, pp. 606-613.

59. Shabana, A.A., 2012, *Computational Continuum Mechanics*, Second Edition, Cambridge University Press.

60. Shabana, A.A., 2014, *Dynamics of Multibody Systems*, Fourth Edition, Cambridge University Press, New York.

61. Spencer, A.J.M., 1971, Theory of Invariants, in Continuum Physics Volume 1: Mathematics, A.C. Eringen Edition, Academic Press, New York, USA

62. Spencer, A.J.M., 1980, *Continuum Mechanics*, Longman, London.

63. Son, G., 2005, "A Level Set Method for Incompressible Two-fluid Flows with Immersed Solid Boundaries", *Numerical Heat Transfer Part B-Fundamentals*, Vol. 47(5), 473-489.

64. Sumner, I.E., 1965, “Experimentally Determined Pendulum Analogy of Liquid Sloshing in Spherical and Oblate-Spherical Tanks”, NASA TN D-2737.

65. Sussman, M., Smereka, P., and Osher, S., 1994, "A Level Set Approach for Computing Solutions to Incompressible 2-phase Flow", *Journal of Computational Physics*, Vol. 114(1), pp. 146-159.

66. Thürey, N., Wojtan, C., Gross, M., and Turk, G., 2010, "A Multiscale Approach to Mesh-based Surface Tension Flows", *ACM Transactions on Graphics*, Vol. 29(4), Article No. 48.

67. Tritton, D., 1986, “Chaos in the Swing of a Pendulum”, *New Scientist*, 24, pp. 37-40.

68. Unruh, J.F., Kana, D.D., Dodge, F.T., Fey, T.A., 1986, “Digital Data Analysis Techniques for Extraction of Slosh Model Parameters”, *Journal of Spacecraft Rockets*, 23(3,4), pp. 171-177.

69. U.S. Department of Transportation, 2012, “National Transportation Statistics, Research and Innovative Technology Administration”, *Bureau of Transportation Statistics*.

70. van Luijk, C.J., Carr, A.J., and Carnaby, G.A., 1984, “Finite Element Analysis of Yarns Part I”, *J. Textile Inst.*, Vol. 75, pp. 342-362.

71. Versteeg, H. K., and Malalasekera, W., 2007, *An Introduction to Computational Fluid Dynamics: the Finite Volume Method*, Second Edition, Pearson/Prentice Hall, Upper Saddle River, New Jersey.

72. Vose, R.W., 1944, “The Dynamics of Flowing Cord”, *Textile Research Journal*, Vol. 14, pp. 105-112.

73. Wang, L., Octavio, J.R.J., Wei, C., and Shabana, A.A., 2015a, Low Order Continuum-Based Liquid Sloshing Formulation for Vehicle System Dynamics. *Journal of Computational and Nonlinear Dynamics.* Vol. 10(2), ID 021022.

74. Wang, L., Wang, Y., Recuero, A.M., and Shabana, A.A., 2015b, ANCF Analysis of Textile Systems. *Journal of Computational and Nonlinear Dynamics*. Vol. 11(3), ID 031005.

75. Wei, C., and Shabana, A.A., 2014, “Continuum-Based Liquid Sloshing Model for Vehicle Dynamics”, Technical report # MBS2014-1-UIC, Department of Mechanical and Industrial Engineering, University of Illinois at Chicago.

76. Wei, C., Wang, L., and Shabana, A.A., 2015, A Total Lagrangian ANCF Liquid Sloshing Approach For Multibody System Applications. *Journal of Computational and Nonlinear Dynamics*. Vol. 10(5), ID 051014.

77. Werner, P.W., Coldwell, J.T., 1961, “Experimental Evaluation of Analytical Models for the Inertias and Natural Frequencies of Fuel Sloshing in a Circular Cylindrical Tanks”, NASA TN D-865.

78. Yan, H. and Conlon, K., 2015, “Trains Derails, Explodes in West Virginia; Crude Oil Spills into River”, *CNN News*, http://www.cnn.com/2015/02/17/us/west-virginia-train-derailment/

79. Yu, J., Wojtan, C., Turk, G., and Tap, C., 2012. "Explicit Mesh Surfaces for Particle Base Fluids", *Eurographics*, Vol.31 (2), pp. 815-824.

80. Zhao, L., Mantell, S.C., Cohen, D., and McPeak, R., 2001, “Finite Element Modeling of the Filament Winding Process”, *Composite Structures*, Vol. 52, pp. 499-510.

81. Zheng, X., Li, X., and Ren, Y., 2012, “Equivalent Mechanical Model for Lateral Liquid Sloshing in Partially Filled Tank Vehicles”, *Mathematical Problems in Engineering*, Article ID 162825.

82. Zienkiewicz, O. C., Nithiarasu, P., Taylor, R. L., and Ebrary Inc., 2005, *The Finite Element Method for Fluid Dynamics* Sixth Edition, Elsevier Butterworth-Heinemann, Amsterdam/Boston.

83. Zikanov, O., and Ebrary Inc., 2010, *Essential Computational Fluid Dynamics*, Wiley, Hoboken, New Jersey.

VITA

L I A N G W A N G

EDUCATION

Doctor of Philosophy, Mechanical Engineering, May 2016, University of Illinois at Chicago (UIC), Major in Dynamic Analysis of Multi-Body Systems, GPA 4.00/4.00

Master of Science, Mechanical Engineering, July 2011, Harbin Institute of Technology (HIT), Major in Process Automation and Detection, GPA 3.86/4.00

Bachelor of Science, Mechanical Engineering, July 2009, Harbin Institute of Technology (HIT), Major in Mechanical Manufacturing and Automation, GPA 3.68/4.00

PROFESSIONAL EXPERIENCE

Teaching Assistant | Dept. of Mech. Engr., UIC **Aug. 2013 - May 2016**

- Perform tasks including grading of homework assignments and examinations, validation of the solutions to these assignments provided by faculty, and holding office hours which students attend voluntarily to supplement the material presented in lecture.

Research Assistant | Dynamic Simulation Laboratory, UIC **Aug. 2011 - May 2016**

- Participate in the development of the general purpose multi-body dynamics software SIGMA/SAMS & specialized railroad industry codes ATTIF; formulation of mathematical models of multi-body systems of interconnected rigid and deformable bodies. Knowledge of FORTRAN used extensively in the development and implementation of different constitutive models such as fluid, metal and textile and their integration with multibody system. Provide analysis of the accuracy and effectiveness of software implementations in the SIGAMA/SAMS software packages.

JOURNAL PUBLICATIONS

1. Shi, H., **Wang, L.**, Shabana, A.A., 2016, Dynamics of Flexible Beam Negotiating a Curve. *Journal of Computational and Nonlinear Dynamics*. (Accepted manuscript)

2. **Wang, L.**, Shi, H., Shabana, A.A., 2015, Effect of the Tank Car Thickness on the Nonlinear Dynamics of Railroad Vehicles. *Journal of Multi-body Dynamics*. (Under review)

3. Aceituno, J.F., Wang, P., **Wang, L.**, and Shabana, A.A., 2015, Influence of Rail Flexibility in a Wheel/rail Wear Prediction Model. *Journal of Rail and Rapid Transit*. DOI: 10.1177/0954409715618426.

4. **Wang, L.**, Wang, Y., Recuero, A.M., and Shabana, A.A., 2015, ANCF Analysis of Textile Systems. *Journal of Computational and Nonlinear Dynamics*. Vol. 11(3), ID 031005.

5. Wei, C., **Wang, L.**, and Shabana, A.A., 2015, A Total Lagrangian ANCF Liquid Sloshing Approach For Multibody System Applications. *Journal of Computational and Nonlinear Dynamics*. Vol. 10(5), ID 051014.

6. **Wang, L.**, Octavio, J.R.J., Wei, C., and Shabana, A.A., 2015, Low Order Continuum-Based Liquid Sloshing Formulation for Vehicle System Dynamics. *Journal of Computational and Nonlinear Dynamics.* Vol. 10(2), ID 021022.

7. Wang, G., **Wang, L.**, Wang, J., Ma, T., 2011, Research on Precise Carbon Film Potentiometer Automatic Trimming Technology and System. *Modular Machine Tool and Automatic Manufacturing Technique.* Vol. 5

CONFERENCE PUBLICATIONS

1. **Wang, L.**, Wang, Y., Recuero, A.M., and Shabana, A.A., ANCF Analysis of Textile Systems. *Proceedings of the ASME 2015 International Design Engineering Technical Conferences& Computers and Information in Engineering Conference*. August 2-5, 2015, Boston, MA, USA. (Paper and Presentation)

2. Wei, C., **Wang, L.**, and Shabana, A.A., A Total Lagrangian ANCF Liquid Sloshing Approach For Multibody System Applications. *Proceedings of the ASME 2015 International Design Engineering Technical Conferences& Computers and Information in Engineering Conference*. August 2-5, 2015, Boston, MA, USA. (Paper and Presentation)

3. **Wang, L.**, Shi, H., Shabana, A.A., Analysis of Tank Car Deformations Using Multibody System and Finite Element Algorithms, *Proceedings of the ASME 2015 International Design Engineering Technical Conferences& Computers and Information in Engineering Conference*. August 2-5, 2015, Boston, MA, USA. (Paper and Presentation)

4. **Wang, L.**, 2014, A New Liquid Sloshing Model for Vehicle Dynamics, *Commercial Vehicle Engineering Congress*, Donald E. Stephens Convention Center, October 7-9, 2014, Rosemont, IL USA. (Presentation only)

5. **Wang, L.**, Octavio, J.R.J., Wei, C., Shabana, A.A., Low Order Continuum-Based Liquid Sloshing Formulation for Vehicle System Dynamics, *Proceedings of the ASME 2014 International Design Engineering Technical Conferences& Computers and Information in Engineering Conference*. August 17-20, 2014, Buffalo, New York, USA. (Paper and Presentation)

PROFESSIONAL SERVICE

Journal Reviewer:

- Journal of Spacecraft and Rockets
- ASME Journal of Computational and Nonlinear Dynamics

Conference Reviewer:

- ASME IDETC/CIE

Mentoring Graduated and Undergraduate Students in Different Research Projects

ACADEMIC HONORS & AWARDS

- UIC Chancellor's Student Service Award, in recognition of outstanding service for the university and community, UIC, 2015.
- Research Assistant Scholarship, UIC, from 2011 to 2013.
- HIT First Grade Scholarship, HIT, from 2009 to 2011
- Meritorious Winner, MCM/ICM (Mathematical Contest in Modeling/Interdisciplinary CM), HIT, 2008
- First Price, National Mathematical Modeling Contest, HIT, 2007
- The title of Excellent Cadre of Students-Future Leader of HIT, HIT, 2006

PROFESSIONAL AFFILIATIONS

- American Society of Mechanical Engineering (ASME)

RESEARCH PROJECTS AND COLLABORATIONS

- Improve Computational Efficiency in MBS Codes

  Integrate the open source package, BLAS and SuperLU_MT in Multibody codes. Use Intel Fortran MKL PADISO to solve linear algebraic equations in parallel.

- Modeling Initially Curved Structure Using ANCF Solid Element

  ANCF solid element is used to model the cylindrical tank car and the liquid in it. The concept of ANCF reference node is used to model the rigid tank and ANCF liquid in a single mesh. Continuity conditions and ANCF constraints are also examined.

- Modeling a New Constitutive Model for Textile Material Using ANCF

  A transversely isotropic hyperplastic constitutive model that is suitable for textile filament bundles is developed in order to simulate a crucial process in the textile industry, namely the roll-drafting process.

- Wheel/rail Wear on Flexible Rail

  Study the influence of rail flexibility within a wheel/rail wear prediction model that computes the material loss based on an energy approach. A comparative study using a sliding approach is also conducted using FASTSIM.

- Modeling Flexible Tank Cars Using FFR Based Shell Element

  To describe the complex geometry of a tank car, a rectangular and triangular shell element is developed to examine the effects of tank car shell thickness on the tank car natural frequency, derailment criteria and running stability.

- Liquid Sloshing Problem Using FFR and ANCF Method and Integration into Railroad Vehicle MBS Model

  A total Lagrangian approach is used to formulate the Navier-Stokes equations using FFR and ANCF elements while the incompressible Newtonian fluid model was integrated with the railroad vehicle to examine the sloshing effects on the motion of the vehicle, especially when the freight train is negotiating a curve.

- Wheel/Rail Contact Project

Develop Fortran Codes for wheel/rail contact based on an elastic contact formulation that would be able to detect multiple contact points between the wheel and rail, whose profile information is described using a spline function.

RESEARCH INTERESTS

Computational Dynamics for Rigid and Deformable Bodies
Liquid Sloshing Problem
Railroad Vehicle Dynamics
Structural Dynamics and Vibrations
Contact Modeling
Process Automation and Detection